

AN INVESTIGATION OF RIVER KINETIC TURBINES:  
PERFORMANCE ENHANCEMENTS, TURBINE MODELLING TECHNIQUES,  
AND AN ASSESSMENT OF TURBULENCE MODELS

by

David L. F. Gaden

A thesis presented to the Faculty of Graduate Studies,  
University of Manitoba in fulfillment of the thesis requirement  
for the degree of Master of Science in  
MECHANICAL ENGINEERING

Department of Mechanical and Manufacturing Engineering  
University of Manitoba  
Winnipeg, Manitoba, Canada

Copyright © 2007 David L. F. Gaden

## **Acknowledgements**

First I would like to thank my fellow graduate students who shared office space with me and helped make my time here more enjoyable, particularly Andrea Kraj and Jeremy Langner. I would also like to thank Kofi Adane for his assistance with my experimentation. Thanks to Dr. M. Tachie who offered me his guidance in interpreting my data. I am very grateful for the contributions of Dr. S. Ormiston, who assisted me with the computational software, and whose understanding helped me in his course when I was facing some unexpected challenges. I am grateful for the contributions from Mr. Philippe Vauthier in the review process and for his interactions with my advisor. I would also like to thank the other members of the graduate committee, Dr. A. Gole and Mr. Tom Molinski for taking the time to participate in the review process. I would like to acknowledge the generous funding provided by Manitoba Hydro and NSERC and the interaction with the Emerging Technologies Group at Manitoba Hydro. Lastly, for Dr. Eric Bibeau's continuous guidance, open-mindedness, understanding, and motivation, I am truly grateful.

## **Abstract**

The research focus of this thesis is on modelling techniques for river kinetic turbines, to develop predictive numerical tools to further the design of this emerging hydro technology. The performance benefits of enclosing the turbine in a shroud are quantified numerically and an optimized shroud design is developed. The optimum performing model is then used to study river kinetic turbines, including different anchoring systems to enhance performance. Two different turbine numerical models are studied to simulate the rotor. Four different computational fluid dynamics (CFD) turbulence models are compared against a series of particle image velocimetry (PIV) experiments involving highly-separated diffuser-flow and nozzle-flow conditions. The risk of cavitation is briefly discussed as well as riverbed boundary layer losses. This study is part of an effort to develop this emerging technology for distributed power generation in provinces like Manitoba that have a river system well adapted for this technology.

## Table of contents

|  |      |
|--|------|
| Acknowledgements.....                              | i    |
| Abstract.....                                      | ii   |
| Table of contents.....                             | iii  |
| List of tables.....                                | viii |
| List of figures.....                               | ix   |
| 1 Introduction.....                                | 1    |
| 1.1 River kinetic hydropower overview .....        | 2    |
| 1.2 Recent kinetic hydro developments.....         | 5    |
| 1.3 Modelling.....                                 | 9    |
| 1.3.1 Rotor modelling .....                        | 11   |
| 1.3.2 Shroud optimisation .....                    | 11   |
| 1.3.3 Riverbed modelling.....                      | 13   |
| 1.3.4 Validation experiment.....                   | 14   |
| 2 Computational model.....                         | 16   |
| 2.1 Notation .....                                 | 17   |
| 2.2 Governing equations.....                       | 18   |
| 2.3 Turbulence models.....                         | 19   |
| 2.3.1 Closure problem.....                         | 21   |
| 2.3.2 Boussinesq eddy-viscosity hypothesis.....    | 22   |
| 2.3.3 Standard k-epsilon turbulence model.....     | 23   |
| 2.3.4 Shear stress transport turbulence model..... | 24   |
| 2.3.5 Reynolds stress turbulence models .....      | 25   |

|         |   |    |
|---------|---|----|
| 2.3.6   | Speziale, Sarkar and Gatski Reynolds turbulence model .....       | 26 |
| 2.3.7   | Baseline Reynolds turbulence model .....                          | 27 |
| 2.3.8   | Numerical solver .....  | 28 |
| 3       | Shroud design.....  | 30 |
| 3.1     | Theory.....   | 30 |
| 3.1.1   | Turbine efficiency and the Betz limit .....                       | 30 |
| 3.1.2   | Ducted turbine theory .....                                       | 33 |
| 3.2     | Turbine rotor modelling.....                                      | 35 |
| 3.2.1   | No model.....   | 36 |
| 3.2.2   | Momentum source .....   | 36 |
| 3.2.2.1 | Momentum source theory .....                                      | 37 |
| 3.2.2.2 | Momentum source error analysis.....                               | 39 |
| 3.2.3   | Averaging rotating reference frame .....                          | 44 |
| 3.2.4   | Sliding mesh rotating reference frame .....                       | 45 |
| 3.3     | Shroud optimization experiment using a momentum source model..... | 45 |
| 3.3.1   | Problem definition .....  | 45 |
| 3.3.2   | Results and discussion .....                                      | 50 |
| 3.4     | Rotating reference frame .....                                    | 56 |
| 3.4.1   | Turbine design and meshing.....                                   | 56 |
| 3.4.2   | Methodology .....   | 62 |
| 3.4.3   | Results and discussion .....                                      | 63 |
| 3.4.4   | Cavitation.....   | 68 |
| 4       | Boundary layer power loss mitigation .....                        | 71 |

|       |   |     |
|-------|---|-----|
| 4.1   | Anchor geometry methodology .....                 | 71  |
| 4.1.1 | Anchor theory .....                               | 72  |
| 4.1.2 | Anchor design .....                               | 73  |
| 4.1.3 | Mesh strategy .....                               | 75  |
| 4.1.4 | Fully-developed boundary layer .....              | 76  |
| 4.2   | Results and discussions.....                      | 76  |
| 5     | Particle Image Velocimetry (PIV) experiment ..... | 81  |
| 5.1   | PIV overview .....                                | 81  |
| 5.2   | PIV theory.....                                   | 83  |
| 5.3   | Apparatus .....                                   | 86  |
| 5.4   | Procedure .....                                   | 88  |
| 5.4.1 | Set-up .....                                      | 88  |
| 5.4.2 | Experimentation .....                             | 90  |
| 5.5   | Data processing.....                              | 91  |
| 5.5.1 | Refraction correction .....                       | 91  |
| 5.5.2 | Masking and value blanking .....                  | 93  |
| 5.5.3 | Adaptive-correlation and averaging.....           | 95  |
| 5.5.4 | Derived quantities .....                          | 96  |
| 5.6   | Error analysis .....                              | 98  |
| 5.6.1 | Monte Carlo simulation .....                      | 98  |
| 5.6.2 | Resolution errors.....                            | 104 |
| 5.6.3 | Seeding density .....                             | 106 |
| 5.7   | Results.....                                      | 106 |

|            |   |     |
|------------|---|-----|
| 5.7.1      | Velocities and streamlines .....          | 106 |
| 5.7.2      | Turbulence .....                          | 109 |
| 5.8        | Discussion.....                           | 110 |
| 6          | Validation computational model.....       | 113 |
| 6.1        | Mesh strategy.....                        | 114 |
| 6.2        | Convergence .....                         | 115 |
| 6.3        | Inlet conditions .....                    | 116 |
| 6.4        | Results.....                              | 117 |
| 6.4.1      | Velocities and streamlines .....          | 117 |
| 6.4.2      | Turbulence .....                          | 119 |
| 6.5        | Discussion.....                           | 123 |
| 7          | Validation comparison .....               | 130 |
| 7.1        | Validation procedure.....                 | 130 |
| 7.2        | Results.....                              | 130 |
| 7.2.1      | Local validation .....                    | 130 |
| 7.2.2      | Full-field validation .....               | 134 |
| 7.3        | Discussion.....                           | 135 |
| 8          | Conclusion .....                          | 139 |
| 8.1        | Future study .....                        | 141 |
|            | Bibliography .....                        | 143 |
| Appendix A | Turbulence Models .....                   | 154 |
| A.1        | Wilcox $k-\omega$ turbulence model.....   | 154 |
| A.2        | Baseline $k-\omega$ turbulence model..... | 155 |

|            |  |     |
|------------|--|-----|
| A.3        | Reynolds stress- $\omega$ turbulence model ..... | 156 |
| Appendix B | Optical correction.....                          | 158 |
| B.1        | Optical correction overview.....                 | 158 |
| B.2        | Cylinder transformation function.....            | 158 |
| B.3        | Transforming an image .....                      | 163 |
| B.4        | Optical correction MATLAB algorithm.....         | 165 |
| Appendix C | PIV Monte Carlo simulation.....                  | 168 |
| C.1        | Monte Carlo simulation MATLAB algorithm.....     | 168 |



## List of tables

|   |     |
|---|-----|
| Table 1 – Kinetic hydro power development.....                          | 6   |
| Table 2 – Experiments performed.....                                    | 10  |
| Table 3 – Momentum source experiment parameters.....                    | 46  |
| Table 4 – Turbine blade details.....                                    | 58  |
| Table 5 – Rotating reference frame experiment parameters.....           | 62  |
| Table 6 – Boundary-layer power loss mitigation experiment details ..... | 72  |
| Table 7 – Anchor mesh sizes .....                                       | 75  |
| Table 8 – Monte Carlo simulation summary .....                          | 100 |
| Table 9 – RMS standards and errors.....                                 | 101 |
| Table 10 – Derived quantities and associated errors .....               | 103 |
| Table 11 – Validation experiment parameters.....                        | 113 |
| Table 12 – Grid independence .....                                      | 115 |
| Table 13 – Convergence independence .....                               | 115 |
| Table 14 – Inlet conditions .....                                       | 117 |

## List of figures

|   |    |
|---|----|
| Figure 1 – River with a natural flow restriction.....   | 3  |
| Figure 2 – Kinetic turbine components based on UEK technology.....                              | 4  |
| Figure 3 – Flow through an unshrouded turbine.....  | 31 |
| Figure 4 – Power ratio versus velocity ratio .....  | 32 |
| Figure 5 – Streamtubes passing through a shrouded and unshrouded turbine.....                   | 34 |
| Figure 6 – Momentum source .....  | 37 |
| Figure 7 – Perturbation factors: (a) squared functions $u^2$ ; (b) cubic functions, $u^3$ ..... | 41 |
| Figure 8 – Momentum source versus theory.....   | 42 |
| Figure 9 – Efficiency, $\eta$ versus factor, $k$ .....  | 43 |
| Figure 10 – Shroud experiment dimensions .....  | 47 |
| Figure 11 – Shroud experiment flow domain .....   | 48 |
| Figure 12 – Shroud experiment 3-D surface mesh and 2-D mesh slice.....                          | 49 |
| Figure 13 – (a) Power and (b) drag versus area ratio.....                                       | 50 |
| Figure 14 – (a) Power and (b) drag versus diffuser angle.....                                   | 52 |
| Figure 15 – Streamlines for the (a) 45° and (b) 20° diffusers.....                              | 53 |
| Figure 16 – Streamlines around turbine configured (a) without and (b) with a diffuser ..        | 54 |
| Figure 17 – Axial velocity, (a) without and (b) with a diffuser .....                           | 55 |
| Figure 18 – Velocity vectors at the turbine blade .....   | 57 |
| Figure 19 – Turbine model .....   | 59 |
| Figure 20 – ARRF flow domain .....  | 59 |
| Figure 21 – ARRF 3-D surface mesh .....   | 60 |
| Figure 22 – Sample mesh at the turbine blades .....   | 61 |

|   |    |
|---|----|
| Figure 23 – Rotating reference frame models.....  | 63 |
| Figure 24 – Power output comparison.....  | 64 |
| Figure 25 – Streamlines across the turbine (a) with no shroud; (b) with a shroud.....   | 65 |
| Figure 26 – Streamlines across turbine (a) without diffuser, and (b) with diffuser..... | 67 |
| Figure 27 – Centreline pressure for ARRF and MS turbine models.....                     | 68 |
| Figure 28 – Surface pressure contour plot.....  | 69 |
| Figure 29 – Anchor A and anchor B isometric view.....                                   | 74 |
| Figure 30 – Anchor C and anchor D isometric view.....                                   | 74 |
| Figure 31 – Boundary-layer power loss.....  | 76 |
| Figure 32 – Power ratio versus $Y^*$ at 2.5 meters from the anchor.....                 | 77 |
| Figure 33 – Power ratio versus $Y^*$ at 7.5 meters.....                                 | 78 |
| Figure 34 – Power ratio versus $Y^*$ at 12.5 meters.....                                | 78 |
| Figure 35 – Streamlines around each anchor.....   | 79 |
| Figure 36 – Mid-stream velocity magnitude contour plot.....                             | 79 |
| Figure 37 – PIV apparatus overview.....   | 82 |
| Figure 38 – PIV displacement comparison.....  | 83 |
| Figure 39 – Particle tracking problems.....   | 84 |
| Figure 40 – Interrogation regions.....  | 84 |
| Figure 41 – Experimental apparatus.....   | 87 |
| Figure 42 – Acrylic model dimensions.....   | 88 |
| Figure 43 – Sample PIV raw image.....   | 92 |
| Figure 44 – Refraction correction, before and after.....                                | 92 |
| Figure 45 – Half-pixel distortion region.....   | 93 |

|  |     |
|--|-----|
| Figure 46 – Typical image mask.....  | 94  |
| Figure 47 – Value blanking.....  | 95  |
| Figure 48 – Monte Carlo simulation results .....                                     | 99  |
| Figure 49 – D30 and N30 streamlines .....  | 107 |
| Figure 50 – D45 and N45 streamlines .....  | 107 |
| Figure 51 – D60 and N60 streamlines .....  | 108 |
| Figure 52 – D30 and N30 velocity contour plots.....                                  | 108 |
| Figure 53 – D45 and N45 velocity contour plots.....                                  | 109 |
| Figure 54 – D60 and N60 velocity contour plots.....                                  | 109 |
| Figure 55 – D45 and N45 turbulence kinetic energy contour plots.....                 | 110 |
| Figure 56 – D45 and N45 turbulence intensity contour plots.....                      | 110 |
| Figure 57 – Nozzle configuration noise.....  | 111 |
| Figure 58 – Cross-stream data extraction .....                                       | 112 |
| Figure 59 – Velocity profile, $U / U_{\infty}$ versus $y$ .....                      | 112 |
| Figure 60 – Inlet flow conditions.....   | 116 |
| Figure 61 – D60 streamlines and velocity contours for $k-\varepsilon$ and SST.....   | 118 |
| Figure 62 – D60 streamlines and velocity contours for SSG and BSL .....              | 118 |
| Figure 63 – N60 streamlines and velocity contours for $k-\varepsilon$ and SST.....   | 119 |
| Figure 64 – N60 streamlines and velocity contours for SSG and BSL .....              | 119 |
| Figure 65 – D60 turbulence kinetic energy contours for $k-\varepsilon$ and SST.....  | 120 |
| Figure 66 – D60 turbulence kinetic energy contours for SSG and BSL.....              | 120 |
| Figure 67 – N60 turbulence kinetic energy contours for $k-\varepsilon$ and SST ..... | 121 |
| Figure 68 – N60 turbulence kinetic energy contours for SSG and BSL.....              | 121 |

|  |     |
|--|-----|
| Figure 69 – D60 turbulence intensity contours for $k-\varepsilon$ and SST.....   | 122 |
| Figure 70 – D60 turbulence intensity contours for SSG and BSL.....               | 122 |
| Figure 71 – N60 turbulence intensity contours for $k-\varepsilon$ and SST.....   | 123 |
| Figure 72 – N60 turbulence intensity contours for SSG and BSL.....               | 123 |
| Figure 73 – D60 wake streamlines for the SSG Reynolds turbulence model.....      | 124 |
| Figure 74 – N60 turbulence intensity using identical scales.....                 | 126 |
| Figure 75 – N60 turbulence kinetic energy using identical scales.....            | 127 |
| Figure 76 – Drag force and mass flow rate.....                                   | 128 |
| Figure 77 – D60 velocity error for $k-\varepsilon$ and BSL.....                  | 131 |
| Figure 78 – N60 velocity error for $k-\varepsilon$ and BSL.....                  | 132 |
| Figure 79 – D60 turbulence intensity error for $k-\varepsilon$ and BSL.....      | 132 |
| Figure 80 – N60 turbulence intensity error for $k-\varepsilon$ and BSL.....      | 133 |
| Figure 81 – D60 turbulence kinetic energy error for $k-\varepsilon$ and BSL..... | 133 |
| Figure 82 – N60 turbulence kinetic energy error for $k-\varepsilon$ and BSL..... | 134 |
| Figure 83 – Velocity RMS error.....  | 134 |
| Figure 84 – Turbulence intensity RMS error.....                                  | 135 |
| Figure 85 – Turbulence kinetic energy RMS error.....                             | 135 |
| Figure 86 – D30 streamlines for PIV and $k-\varepsilon$ .....                    | 137 |
| Figure 87 – Optical correction variables.....                                    | 159 |
| Figure 88 – Optical transformation function.....                                 | 162 |
| Figure 89 – Optical distortion.....  | 163 |
| Figure 90 – Scale ray traces showing maximum deviation.....                      | 163 |

## **1 Introduction**

Growth in energy consumption and environmental concerns over conventional power generation technologies has given rise to a need for alternative energy sources. Emerging hydro technologies consist of kinetic currents, tidal and wave applications. River kinetic hydropower is a promising technology that involves the use of underwater turbines in fast moving rivers to produce electricity. The technology differs from more conventional hydropower technologies in that it does not require a dam, or powerhouse. River kinetic hydropower is well-suited for distributed power generation. The technology has been available for decades; however despite its minimal environmental impact, commercialization has been limited. Recently, there has been a large resurgence in the interest in all forms of emerging hydro technologies (Sergergren 2005); however, the application of river kinetic hydropower is largely undocumented (Gaden 2006).

The main purpose of this thesis is to develop and evaluate a set of design tools for practical application to the development of river-kinetic hydro power. It is not intended as a rigorous academic investigation of specific flow conditions. Therefore the goal is not to obtain highly accurate results, but rather to cover a wide array of modelling techniques and obtain an understanding of their performance. Hence an emphasis will be placed more on the trends in the data rather than the exact values. Although broad in scope, important general conclusions can be drawn from these studies. In the field of fluid dynamics, three techniques are used to gain insight into the behaviour of fluids: theoretical, numerical, and experimental. All these techniques have deficiencies, as theoretical and numerical solutions are both limited by our breadth of knowledge, and

experimental data is limited by the errors inherent in our experiment and by the costs of test equipment. It is important to understand what useful information can be obtained from any design tools, and under what circumstances. Therefore, in this thesis, all techniques are presented, along with a detailed study of the limitations of each approach. The results in concert with the error analyses will provide the reader with an appreciation of the capabilities of the design tools available to river-kinetic turbines. It is important not to lose sight of the primary goal of this thesis: to improve our ability to extract power from kinetic flows. This thesis provides a stepping-stone to further the development of this technology.

## **1.1 River kinetic hydropower overview**

River kinetic hydropower is a technology that uses the kinetic energy in a river to generate electrical power when the flow is sub-critical<sup>1</sup>. Installations are sited at strategic points along a targeted river where the land formation provides a natural flow restriction, resulting in high streamwise velocities as shown in Figure 1.

At these locations, one or several kinetic turbines are installed beneath the surface of the water for the purpose of electrical power generation. The term *kinetic hydropower*<sup>2</sup> is used to differentiate this technology from run-of-river and small hydropower, which require the construction of dams or powerhouses.

---

<sup>1</sup> Sub-critical flow occurs when the river velocity is less than the wave velocity. When the river is in this condition, an obstruction will not significantly alter the flow field. Conversely, in super-critical flow, an obstruction can produce hydraulic jumps.

<sup>2</sup> Unless otherwise specified, the term is applied exclusively to river applications in this thesis.



**Figure 1 – River with a natural flow restriction<sup>3</sup>**

A kinetic hydropower installation is composed of four main components, as shown in

Figure 2:

- turbine;
- shroud (optional);
- cable anchoring structure; and
- generator and subsequent power distribution.

---

<sup>3</sup> maps.google.com – This satellite image was selected for demonstration; the actual geographic location is inconsequential.



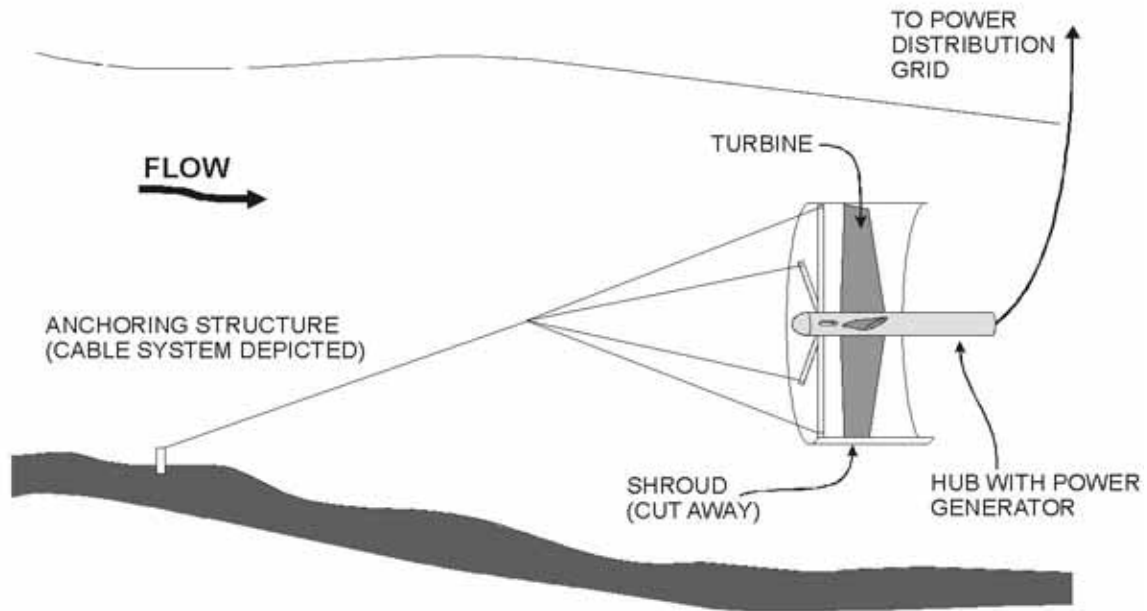


**Figure 2 – Kinetic turbine components based on UEK technology**

Alternatively, a fixed anchor can be used which, unlike a cable anchor, must also withstand a moment force which is function of the height of the turbine above the river bed and the peak drag force expected during the lifetime of the turbine. This increases costs.

Kinetic hydropower has no reservoir, spillway, or emissions. Therefore environmental impact is minimal, and site selection is far less restrictive compared with other hydro technologies. The initial installation cost and deployment time is relatively short as river kinetic hydropower does not require any significant infrastructure, such as dams or powerhouses. The modular nature of kinetic hydropower leads to an easily scalable energy output but with limited opportunities to decrease the capital cost per kW. Finally, river flows lead to continuous energy production, thus eliminating the need for any

significant energy storage capacity, an important advantage in remote communities and of interest to utilities. This technology is intended to supplement existing hydro power generation.

Installation and servicing may be complicated by dangerous river conditions, cold weather and seasonal ice floes, where applicable. The design must accommodate diverse flow conditions, including seasonal variations in the river flow rate, thus design optimization is compromised. There is no control over the upstream flow conditions or riverbed surface, therefore turbulence, silt and foreign debris are expected at the inlet. The turbine may be designed to move in the vertical direction to avoid debris during spring runoff, similar to the UEK design (Vauthier 2006). Turbulent inlet flow may lead to cavitation on the turbine blades. Finally, the technology poses an unknown risk to fish, vegetation, and other habitants of the river, a risk that must be understood before large-scale deployment is considered.

## **1.2 Recent kinetic hydro developments**

A summary of river kinetic turbine and ocean kinetic turbine-related developments are shown in Table 1<sup>4</sup>. Although much development has taken place for hydro kinetic turbines (Melvin 2004), there is little available in the technical literature sources. In Canada there has been an emphasis on vertical axis hydro turbines, or Darreius turbines, such as with Nova Energy, Blue Energy, and New Energy. There have been recent efforts to commercialize these small scale Darreius turbines in Canada. More recently, axial hydro turbines have been investigated in Canada, with a one-month test installation

---

<sup>4</sup> Adapted from Segergren, 2005

near St. Catharines, Ontario, and an on-going demonstration project at Race Rocks in British Columbia. This thesis is complementary to an up-coming test in Manitoba involving the UEK turbine, a three meter ducted axial turbine. Therefore the focus will be on horizontal axis turbines.

**Table 1 – Kinetic hydro power development**

| <b>Name / Location</b>   | <b>Year(s)</b> | <b>Resource</b>             | <b>Type</b>          | <b>Duct</b> | <b>Anchor</b>          | <b>Dia-meter</b> | <b>Output</b> |
|--|----------------|-----------------------------|----------------------|-------------|------------------------|------------------|---------------|
| The Coriolis Program (Gulf Stream, USA) <sup>5,6</sup>                                 | 1973-1978      | Ocean current               | Axial turbine        | Yes         | Cabled                 | 1 m              |               |
| ITDG/IT Power (River Nile, Sudan) <sup>7</sup>   | 1976-1983      | River                       | Darrieus turbine     | No          | Pontoon                | 3 m              |               |
| Underwater Electric Kite (USA) <sup>8</sup>  | 1981-Present   | River, ocean current, Tidal | Axial turbine (Twin) | Yes         | Cabled, Fixed, Pontoon | 3 m              | Up to 120 kW  |
| National Research Council and Nova Energy Ltd. (St. Lawrence River) <sup>9</sup>       | 1982           | River                       | Darrieus turbine     | Yes         | Pontoon                | 1.8 m            | 25 kW         |
| National Research Council and Nova Energy Ltd. (Sheet River, Nova Scotia) <sup>9</sup> | 1983-1985      | River                       | Darrieus turbine     |             | Existing structure     | 1.8 m            | 10 kW         |

<sup>5</sup> Lissaman et al., 1979

<sup>6</sup> Venezia, W. A., 1994

<sup>7</sup> Technomare SpA et al., 1996

<sup>8</sup> www.uekus.com (accessed 2007-01-16)

<sup>9</sup> H. N. Halvorson Consultant Ltd., 1994

| <b>Name / Location</b>   | <b>Year(s)</b> | <b>Resource</b> | <b>Type</b>      | <b>Duct</b> | <b>Anchor</b> | <b>Dia-meter</b> | <b>Output</b> |
|--|----------------|-----------------|------------------|-------------|---------------|------------------|---------------|
| Nihon University (Kurushima Straits, Japan) <sup>7</sup>               | 1983-1988      | Ocean current   | Darrieus turbine | No          | Seabed        |                  | 3.5 kW        |
| Nova Energy Ltd. (Gulf Stream, USA) <sup>6,7</sup>                     | 1984-1985      | Ocean current   | Darrieus turbine | Yes         | Cabled        | 1.2 m            | 4 kW          |
| Russian Joint Stock Co. <sup>7</sup>                                   |                | River           | Axial turbine    | Yes         | Pontoon       | 1.8 m            |               |
| Scottish Nuclear, IT Power, NEL (Loch Linnhe, Scotland) <sup>7</sup>   | 1994           | Tidal           | Axial turbine    |             | Pontoon       | 3.5 m            | 15 kW         |
| Northern Territory University (Aspley Straits, Australia) <sup>7</sup> | 1994           | Ocean current   | Axial turbine    | No          | Pontoon       |                  |               |
| Marine Current Turbines Ltd. (3 km NE of Lynmouth, UK) <sup>10</sup>   | 1999-Present   | Tidal           | Axial turbine    |             | Seabed        | 11 m             | 300 kW        |

<sup>10</sup> [www.marineturbines.com](http://www.marineturbines.com) (accessed 2007-01-16)

| Name / Location   | Year(s)      | Resource     | Type                  | Duct | Anchor             | Dia-meter | Output  |
|---|--------------|--------------|-----------------------|------|--------------------|-----------|---------|
| Ontario Power Generation, UEK, St. Catharines, Ontario <sup>11,12</sup> | 2000         | River        | Axial turbine (Twin)  | Yes  | Cabled             | 3 m       | < 30 kW |
| Hammerfest Strøm AS (Strait of Kvalsundet, Norway) <sup>13</sup>        | 2002         | Tidal        | Axial turbine         |      | Seabed             | 20 m      | 300 kW  |
| Exim and Seapower (Sweden / Scotland) <sup>14</sup>                     | 2002-Present | Ocean        | Savonius turbine      |      | Buoyed             |           |         |
| Hydro Venturi Ltd. <sup>15</sup>  | 2002-Present | River, Tidal | Axial turbine         | Yes  | Existing structure |           |         |
| TidEl Generator <sup>16</sup>   | 2003-Present | Tidal        | Axial turbine         | No   | Cabled             | 1.3 m     |         |
| Lunar system <sup>17</sup>  | 2003-Present | Tidal        | Axial turbine         | Yes  | Seabed             |           |         |
| Engineering Business Ltd, Stingray Tidal Stream Generator <sup>18</sup> | 2002-Present | Tidal        | Hydro-plane actuation | No   | Seabed             | N/A       | 150 kW  |

<sup>11</sup> Molinski, T., 2004. "Re: OPG experience with UEK design and list of recommendations". Memorandum from Manitoba Hydro, Power Planning & Development Division, August 20, 2004.

<sup>12</sup> Vauthier, 2006.

<sup>13</sup> [www.tidevannsenergi.com](http://www.tidevannsenergi.com) (accessed 2007-01-16)

<sup>14</sup> Lagström, G. E., 2003

<sup>15</sup> [www.hydroventuri.com](http://www.hydroventuri.com) (accessed 2007-01-16)

<sup>16</sup> [www.smdhydrovision.com](http://www.smdhydrovision.com) (accessed 2007-01-16)

<sup>17</sup> [www.lunarenergy.co.uk](http://www.lunarenergy.co.uk) (accessed 2007-01-16)

<sup>18</sup> Trapp, T., 2002; [www.engb.com](http://www.engb.com) (accessed 2007-01-16)

| Name / Location   | Year(s)      | Resource        | Type             | Duct | Anchor  | Dia-meter | Output  |
|---|--------------|-----------------|------------------|------|---------|-----------|---------|
| Pearson College, EnCana, Clean Current (Race Rocks, British Columbia) <sup>19</sup> | 2004-Present | Tidal           | Axial turbine    | Yes  | Seabed  |           |         |
| New Energy Corporation, Alberta <sup>20</sup>                                       | 2003-present | River and tidal | Darrieus turbine | Yes  | Various | 1.0 m     | 5–25 kW |
| Starkraft Development, Norway <sup>21</sup>   | 2004-Present | Tidal           | Axial turbine    | No   | Pontoon | 15 m      |         |
| University of Manitoba, Manitoba Hydro (Point du Bois, Manitoba)                    | 2007         | River           | Axial turbine    | Yes  | Boat    | 3 m       | 60 kW   |

### 1.3 Modelling

Computer models enable designers to rapidly test many configurations, and study their behaviour with numerical simulations. These experiments do not require the construction of physical prototypes, or sensor equipment for data collection, and can therefore produce vast amounts of data with minimal costs. However, the accuracy and usefulness of the results depends on how closely the simulation matches reality.

There is little in the way of numerical studies on kinetic hydropower in the open literature, especially those focusing on river applications. Therefore an important step toward furthering the development of river kinetic turbines is to find a computational

<sup>19</sup> [www.racerocks.com](http://www.racerocks.com) (accessed 2007-01-16)

<sup>20</sup> [www.newenergycorp.ca](http://www.newenergycorp.ca) (accessed 2007-01-16)

<sup>21</sup> [www.starkraft.com](http://www.starkraft.com) (accessed 2007-01-16)

fluid dynamic (CFD) model that adequately represents river kinetic turbines. This challenge is addressed herein on three fronts. From the perspective of fluid flow, the river kinetic turbines are composed of three main fluid dynamic elements. These are:

- the turbine rotor – a rotating machine part with a complex geometry;
- the shroud – an axisymmetric component with internal and external flows; and
- the river bed – a boundary condition that differs at every installation site.

Several experiments are performed with a focus on various combinations of these main elements. The goal is to find a robust model that successfully handles all these elements, and has been validated against experimental data; however, such an endeavour is too broad in scope to cover in a single thesis. Therefore, the focus of this thesis is to lay some of the groundwork in modelling river kinetic turbines. Four numerical experiments are performed, as shown in Table 2. The governing equations, turbulence models and discretisation employed in these models are reviewed in Chapter 2.

**Table 2 – Experiments performed**

| <b>Experiment</b>                    | <b>Elements</b> | <b>Type</b>  |
|--------------------------------------|-----------------|--|
| Momentum source evaluation           | Rotor           | Numerical experiment compared with theory              |
| Shroud optimisation                  | Rotor, Shroud   | Numerical experiment only                              |
| Boundary layer power-loss mitigation | River bed       | Numerical experiment only                              |
| Validation                           | Shroud          | Numerical experiment compared with physical experiment |

The results obtained herein can also be applied to ocean-kinetic and ocean-tidal hydropower applications. Furthermore, this study serves as a starting point to investigate the use of this technology in geographic areas like Manitoba, a cold weather climatic

region that has well over 20% of the North American precipitation draining through its territory based on watershed catchment area, making this emerging technology ideally suited (Bibeau 2006).

### **1.3.1 Rotor modelling**

The turbine rotor represents a challenge in numerical analysis due to its complex geometry and rotational motion. This component is addressed in Chapter 3, where four turbine rotor modelling techniques are reviewed, and two are employed. A momentum source model is used to produce rapid design iterations, and a rotating reference frame is later used to confirm the momentum source results.

### **1.3.2 Shroud optimisation**

A potentially significant improvement to the technology involves the use of a shroud around the turbine. If the geometry of the shroud is carefully designed, it will increase the velocity of the flow passing through the turbine, similar to a ducted fan. Since the power available in the fluid is proportional to the cube of the velocity, a small velocity increase will translate into a significant power production increase. This is particularly important for kinetic turbines because, unlike wind energy where economies of scale have been realized by constructing larger rotor diameters (Herbert 2007; Flay 1996), river-kinetic turbines are restricted in size by the cross section of the channel. Therefore, maximizing the energy density in the useable cross sectional area is of great importance to make this technology viable for river applications, a restriction not necessarily applicable to ocean deployment. In addition, the use of a shroud may reduce maintenance and operational costs as it acts as a floatable structure to simplify anchoring



and retrieval to avoid the use of a barge, crane and divers during maintenance (Vauthier 2006). Furthermore as suggested by Vauthier, the shroud offers a structure to attach a louver system in compliance with small hydro regulations requiring a screen upstream of the turbine where applicable. Presently, no such regulation is defined in Canada for this emerging technology.

Although there is little in the open literature available for river kinetic turbines, studies on wind turbines are relevant due to their similarities. Diffuser systems for wind turbines have been investigated in detail (Igra 1981a; Igra 1981b; Helmy 1991; Al-Sulaiman et al. 1992; Phillips et al. 1999a; Phillips et al. 1999b; Bet et al. 2003; Grassmann et al. 2003a; Grassmann et al. 2003b; Grassmann et al. 2005). The theory behind the benefits of using a shroud is well understood (Lewis et al. 1977; Helmy et al. 1991; Grassmann et al. 2003b). A simplified one dimensional analysis by Phillips et al. (1999b) shows a potential power increase by a factor of four, but experimental results did not show this. Numerical studies by Bet et al. (2003) and Grassmann et al. (2003b) show aerodynamic features can boost the power output by a factor of two and five respectively; however, experimental results later showed an output voltage boost of only 1.25 under unloaded conditions (Grassmann et al. 2003a). An experiment involving an 88 mm diameter turbine showed a promising power increase by a factor of three (Igra 1981). Large scale deployment of shrouded wind turbines has not occurred, possibly because the large rotor diameters can lead to prohibitive costs for the duct structure. Al-Sulaiman et al. (1992) suggest that shrouds may be useful in regions where the low wind power density renders conventional turbines unfeasible.

The results of these studies provide evidence that a diffuser system would be beneficial for river kinetic turbines. In fact, Grassmann et al. (2003b) review the differences between the theory for ducted wind and for ducted hydro turbines, and suggest that the numerical findings for wind is also applicable to hydro applications. However, none of these studies actually models water flow through a ducted turbine. It is unknown whether the benefits of a shroud (e.g. increased power output) will outweigh the negative impacts of a shroud (e.g. increased drag). Furthermore, if cross-sectional area is limited, the use of a shroud comes at the expense of turbine rotor area. It is unknown whether there is a benefit to using a shroud with a smaller turbine, or maximizing the turbine rotor diameter within the available area. These are questions that will be addressed in Chapter 3.

### **1.3.3 Riverbed modelling**

Boundary layer power-loss is a phenomenon in which the power output of the turbine is negatively impacted by the boundary layer of the riverbed. Due to the limited cross sections of rivers, boundary layer power-loss is a concern for river kinetic turbines. A potential mitigation technique involves the use of an upstream obstruction designed to alter the downstream flow in a beneficial manner. Furthermore, such an object may also be used as an anchoring structure for the river kinetic turbine and as a means to protect the turbine during runoff periods that carry debris.

There are few studies in the open literature that address this question. The field of wind energy suffers from boundary layer power-loss as well and it has long been known that

wind speed increases with altitude. In general wind turbine towers have been increasing in height, however, given the limited cross-sectional area of a river, increasing height is not an option for river kinetic turbines.

Submerged breakwaters have a similar physical arrangement to the proposed anchor study, and there have been many studies on the downstream effects of these marine components (Reddy et al. 2007; Ranasinghe et al. 2006; Johnson et al. 2005; Stamos et al. 2003). These studies are focused on modelling the surface dynamics of waves (Stamos et al. 2003) and shoreline effects (Ranasinghe et al. 2006). Often the flow beneath the surface is modelled with simplifying assumptions (Johnson et al. 2005). It is unknown what effect an obstruction will have on the downstream riverbed boundary layer, and it is unknown whether the geometry of the obstruction can be modified to benefit a downstream river kinetic turbine. The boundary layer power-loss mitigation experiment in Chapter 4 addresses these questions with a three-dimensional numerical investigation.

#### **1.3.4 Validation experiment**

The accuracy of a numerical model varies greatly depending on the parameters of the problem. Basing a design on a numerical model alone can produce unexpected behaviour, or even catastrophic failure. It is therefore important to validate the model against physical experimental data to ensure it produces accurate predictions, and to become familiar with the conditions in which it performs with less accuracy.

For river kinetic turbines, a validation is desired that encompasses all three fluid dynamic elements (the rotor, the shroud, and the riverbed). For this thesis, a series of experiments was performed to validate multiple turbulence models for the shroud component. These experiments are presented in Chapters 5 to 7. Unfortunately, the results of these experiments are hindered by experimental error, and inadequately modelled boundary conditions. However, qualitative conclusions are drawn from these results and the methodology is thoroughly documented. Therefore these Chapters may serve as a template for future experiments.

Before studying river-kinetic hydro turbines, we will review the computational model for the numerical simulations.

## 2 Computational model

A computational model for a kinetic turbine must incorporate a diversity of elements before it can be utilized to develop and optimise the technology. Such elements include:

- solving the governing equations in three dimensions;
- adequately modelling the large scale eddies generated by the riverbed boundary layer;
- selection of a turbulence model that performs well at high Reynolds numbers, as kinetic hydropower is most economic at velocities giving Reynolds numbers in excess of  $10^6$ , based on the freestream velocity and the rotor diameter;
- modelling challenging boundary conditions, including:
  - the free surface and its small slope angles;
  - the roughness of the riverbed surface;
  - inlet conditions that are difficult to quantify due to turbulence and complex boundary layer profiles depending on the upstream river geometry; and
  - the long distance required to recover pressure gradients, thus increasing the computational domain downstream of the turbine;
- modelling of a shroud that can cause severe flow separation;
- inner and outer ducted channel flow;
- rotating blades with possible boundary layer transition from laminar to turbulence and separating flows on the blade surface;

- swirl caused by the rotor;
- inlet guiding vanes and stators to properly direct the inlet flow to increase efficiency;
- the transport of silt and rocks that wear down turbine materials;
- ice cover effects that alter the river flow;
- the effect of anchoring geometry on turbine performance and disruption of river flow;
- the impact on the ecosystem and techniques to minimize this effect, particularly fish mortality;
- the behaviour of turbine arrays, such as the effect of upstream turbines on performance;
- accurate drag calculations to facilitate optimal anchoring designs; and
- a large computational domain of the entire river section modelled with a turbine.

Several turbulence models are evaluated in the course of this thesis. The optimum model is selected based on its performance in highly separated external flow, and diffuser and nozzle flow conditions. This turbulence model is then used for simulations with the turbine rotors.

## 2.1 Notation

There are multiple notational conventions available. For instance, the gradient of a variable,  $\theta$  can be expressed:

in vector notation:  $\nabla \cdot \theta$ ;

in index notation:  $\frac{\partial \theta_i}{\partial x_i}$ ; and

in explicit notation:  $\frac{\partial \theta_x}{\partial x} + \frac{\partial \theta_y}{\partial y} + \frac{\partial \theta_z}{\partial z}$ .

Unless otherwise indicated, index notation will be used herein.

## 2.2 Governing equations

The motion and properties of a fluid can be modelled with a set of fundamental equations known as the Navier-Stokes equations. The continuity equation is an extension of the conservation of mass to fluidic media. For an incompressible Newtonian fluid, the continuity equation is:

$$\frac{\partial u_i}{\partial x_i} = 0, \quad (1)$$

where  $x_i$  is the  $i^{\text{th}}$  spatial dimension; and  $u_i$  is the  $i^{\text{th}}$  component of velocity. Similarly, the momentum equation is:

$$\rho \frac{\partial u_i}{\partial t} + \rho \frac{\partial}{\partial x_j} (u_i u_j) = -\frac{\partial p}{\partial x_i} + \mu \left( \frac{\partial^2 u_i}{\partial x_j^2} + \frac{\partial^2 u_j}{\partial x_j \partial x_i} \right) + S_{M,i}, \quad (2)$$

where  $\rho$  is fluid density,  $t$  is time;  $\mu$  is the dynamic viscosity; and  $S_{M,i}$  is the momentum source in the  $i^{\text{th}}$  direction.

Equations (1) and (2) are based on the approximation that a fluid is a continuous medium (Panton 1996, p. 3). On the microscopic scale, a fluid is not a continuum; it is composed

of individual atoms, interacting and colliding. It would be impractical to model individual molecules, especially considering that a millilitre of water contains more than  $30 \times 10^{18}$  molecules. On significantly larger scales, there are considerable numbers of atoms, and their interactions can be characterized as continuous properties, such as pressure and density. Thus the continuum assumption simplifies the problem. However, when turbulence sets in, the intermolecular interactions become

However, when turbulence sets in, the fluid enters a condition that is challenging to model. Small scale phenomena occur that affect the flow field, and cannot be captured fully. Additional quantities, such as turbulence kinetic energy, are introduced to describe these phenomena within a continuum formulation.

### **2.3 Turbulence models**

The Reynolds number is used to characterise a flow:

$$Re = \frac{\rho U_c L_c}{\mu}, \quad (3)$$

where  $U_c$  is a characteristic velocity and  $L_c$  is a characteristic length scale. The Reynolds number represents the ratio of inertial forces to viscous forces (Davidson 2004, p. 9).

Viscous forces can be interpreted as forces holding the fluid together; inertial forces can be interpreted as forces pulling the fluid apart. Flows with a high Reynolds number are unstable because they represent flow conditions in which the inertial forces are large and the viscous forces small. When the Reynolds number is large enough, turbulence sets in. Turbulent flow is characterised by random instantaneous fluctuations in hydrodynamic quantities, but with meaningful time and space average values (Horák 1972).



To incorporate these turbulent fluctuations into a mathematical environment, statistical averaging is used. For instance, instantaneous velocity is expressed as the sum of the mean velocity and a fluctuating component:

$$U = \bar{U} + u , \quad (4)$$

where  $U$  is instantaneous velocity;  $\bar{U}$  is average velocity; and  $u$  is the fluctuating component. This statistical technique is applied to the Navier-Stokes Equations (1) and (2), producing the Reynolds averaged Navier-Stokes equations (RANS). Continuity becomes:

$$\frac{\partial \bar{U}_i}{\partial x_i} = 0 , \quad (5)$$

where  $\bar{U}_i$  is the average velocity. The momentum equation is:

$$\rho \frac{\partial \bar{U}_i}{\partial t} + \rho \frac{\partial}{\partial x_j} (\bar{U}_j \bar{U}_i) = -\frac{\partial \bar{p}}{\partial x_i} + \mu \left( \frac{\partial^2 \bar{U}_i}{\partial x_j^2} + \frac{\partial^2 \bar{U}_i}{\partial x_j \partial x_i} \right) - \rho \frac{\partial}{\partial x_j} (u_i' u_j') + \bar{S}_{M,i} , \quad (6)$$

where the overbar indicates time-averaged quantities. For simplicity, the overbar notation will be discontinued henceforth. The term  $u_i'$  in Equation (6) is the root mean square of the fluctuating component of velocity, defined as:

$$u' = \sqrt{\frac{1}{t_1 - t_0} \int_{t_0}^{t_1} [u(t)]^2 dt} \quad (7)$$

Comparing Equations (2) and (6) reveals that there is an additional term on the right-hand side involving  $u_i' u_j'$ . This term has been interpreted as a stress on an element of fluid,

caused by the turbulent fluctuations. This leads to the definition of the Reynolds stress tensor:

$$\tau_{ij}^R = -\rho u'_i u'_j. \quad (8)$$

### 2.3.1 Closure problem

The appearance of the Reynolds stress tensor introduces a closure problem. There are two governing equations (continuity and momentum); however, there are now three unknowns ( $p$ ,  $u_i$ , and  $\tau_{ij}^R$ ). Another equation is necessary to relate the Reynolds stress tensor to known quantities. No such equation exists, and this problem remains one of the challenges of modern fluid dynamics (Gao et al. 2004).

A turbulence model is an approximation based on one or several assumptions that allows the Reynolds stresses to be solved. The relations used by a turbulence model are generally valid only for a very specific set of flow conditions; there is no universally successful turbulence model (Házi 2005).

Turbulence models can be divided into two broad categories:

- models based on the eddy-viscosity hypothesis (Sections 2.3.2 to 2.3.4); and
- Reynolds stress models (Sections 2.3.5 to 2.3.7).

### 2.3.2 Boussinesq eddy-viscosity hypothesis

According to the Boussinesq eddy-viscosity hypothesis, the Reynolds stresses are proportional to the mean velocity gradients:

$$\tau_{ij}^R = \mu_T \left( \frac{\partial U_i}{\partial x_j} + \frac{\partial U_j}{\partial x_i} \right) \quad (9)$$

where  $\mu_T$  is turbulent viscosity, the constant of proportionality. With this relation, the momentum equation simplifies to:

$$\rho \frac{\partial U_i}{\partial t} + \rho \frac{\partial}{\partial x_j} (U_j U_i) = -\frac{\partial p}{\partial x_i} + \mu_{eff} \left( \frac{\partial^2 U_i}{\partial x_j^2} + \frac{\partial^2 U_i}{\partial x_j \partial x_i} \right) + S_{M,i}, \quad (10)$$

where  $\mu_{eff}$  is effective viscosity, given by:

$$\mu_{eff} = \mu + \mu_T. \quad (11)$$

When the eddy-viscosity hypothesis is combined with a scheme to determine turbulent viscosity,  $\mu_T$ , the governing equations can be solved.

The eddy-viscosity hypothesis has several limitations. For instance,  $\tau_{ij}^R$  and the velocity gradients are related by a scalar,  $\mu_T$  instead of a tensor. This is inadequate for highly anisotropic turbulence (Davidson 2004, p. 176). Despite its limitations, models based on the eddy-viscosity hypothesis are computationally simple, and practical for most engineering applications.

### 2.3.3 Standard k-epsilon turbulence model

The standard  $k$ - $\varepsilon$  turbulence model was first introduced in 1968 (Harlow et al. 1968), although Jones et al. (1972) have been credited with developing it in its modern form (Scott-Pomerantz 2004). The standard  $k$ - $\varepsilon$  turbulence model is a two equation approximation based on the eddy-viscosity hypothesis. Two new variables are introduced: turbulence kinetic energy,  $k$ , and turbulence dissipation,  $\varepsilon$ . Transport equations are derived for the new variables. Finally, turbulent viscosity is solved by relating it to these new variables:

$$\mu_T = C_\mu \rho \frac{k^2}{\varepsilon}, \quad (12)$$

where  $C_\mu$  is an empirical constant,  $k$  is turbulence kinetic energy, and  $\varepsilon$  is dissipation.

The transport equation for  $k$  is obtained by multiplying the momentum Equation (6) by velocity  $U_i$  (Panton 1996, p. 765):

$$\rho \frac{\partial k}{\partial t} + \rho \frac{\partial}{\partial x_i} (kU_i) = \frac{\partial}{\partial x_j} \left[ \left( \mu + \frac{\mu_T}{\sigma_k} \right) \frac{\partial k}{\partial x_j} \right] + P_k - \rho \varepsilon, \quad (13)$$

where  $P_k$  is turbulence production due to viscous and buoyancy forces, given by:

$$P_k = \mu_T (2S_{ij}S_{ij}), \quad (14)$$

where  $S_{ij}$  is the viscous strain-rate defined by:

$$S_{ij} = \frac{1}{2} \left( \frac{\partial U_i}{\partial x_j} + \frac{\partial U_j}{\partial x_i} \right). \quad (15)$$

Whereas the transport equation for  $k$  is derived using well-defined analytical methods, the transport equation for  $\varepsilon$  is arbitrarily designed (Davidson 2004, p. 125). The transport equation for  $\varepsilon$  is:

$$\rho \frac{\partial \varepsilon}{\partial t} + \rho \frac{\partial}{\partial x_i} (\varepsilon U_i) = \frac{\partial}{\partial x_j} \left[ \left( \mu + \frac{\mu_T}{\sigma_\varepsilon} \right) \frac{\partial \varepsilon}{\partial x_j} \right] + \frac{\varepsilon}{k} (C_{\varepsilon 1} P_k - C_{\varepsilon 2} \rho \varepsilon). \quad (16)$$

In Equations (12), (13) and especially (16) there are several constants. These constants have been selected empirically in order to give the  $k$ - $\varepsilon$  model good predictive abilities, and self-consistency. They are:

$$C_{1\varepsilon} = 1.44, \quad C_{2\varepsilon} = 1.92, \quad C_\mu = 0.09, \quad \sigma_k = 1.0, \quad \sigma_\varepsilon = 1.3. \quad (17)$$

Finally, pressure is modified in the standard  $k$ - $\varepsilon$  model according to:

$$p' = p_s + \frac{2\rho k}{3}, \quad (18)$$

where  $p_s$  is the stagnation pressure.

The standard  $k$ - $\varepsilon$  turbulence model has several limitations. For instance, it is well known to be insensitive to adverse pressure gradients (Menter 1993). For the purposes of modelling diffuser flow, this is a serious concern. Furthermore, the model behaves poorly in near-wall regions, requiring complex non-linear wall functions.

### 2.3.4 Shear stress transport turbulence model

The shear stress transport turbulence model (SST) is an extension to the BSL  $k$ - $\omega$  model (refer to Appendix A). The SST model is based on the BSL model, but includes a

transport model for turbulent shear stress, an addition intended to resolve the shortcomings of the BSL  $k$ - $\omega$  models (ANSYS 2005). The equation for turbulent viscosity is modified to limit its growth:

$$\mu_T = \rho \frac{a_1 k}{\max(a_1 \omega, SF_2)}, \quad (19)$$

where  $a_1$  is an empirical constant;  $k$  is turbulence kinetic energy;  $\omega$  is turbulence frequency;  $S$  is an invariant measure of strain rate; and  $F_2$  is a blending function.

### 2.3.5 Reynolds stress turbulence models

Reynolds stress turbulence models (RSTM) were developed in an attempt to resolve some of the short-comings of the eddy-viscosity hypothesis, such as modelling severely anisotropic turbulence (Davidson 2004, p. 186). RSTMs are turbulence models that do not use the eddy-viscosity hypothesis. They specify a relation to solve each component of the Reynolds stress tensor with differential or numerical methods. The first RSTM was developed in 1975 (Launder et al. 1975). Under this formulation, the transport equation for Reynolds stress is:

$$\rho \frac{\partial}{\partial t} (u'_i u'_j) + \rho \frac{\partial}{\partial x_k} (U_k \rho u'_i u'_j) = P_{ij} + \phi_{ij} + \frac{\partial}{\partial x_k} \left[ \left( \mu + \frac{2}{3} c_s \rho \frac{k^2}{\varepsilon} \right) \frac{\partial u'_i u'_j}{\partial x_k} \right] - \frac{2}{3} \delta_{ij} \rho \varepsilon, \quad (20)$$

where  $\phi_{ij}$  is the pressure-strain term, and  $P_{ij}$  is the production term,  $\varepsilon$  is the turbulence dissipation,  $k$  is the turbulence kinetic energy. All these have their own associated transport equations, and empirical constants.  $k$  and  $\varepsilon$  use the transport equations from the standard  $k$ - $\varepsilon$  model, Equations (16) and (13) respectively.  $P_{ij}$  is given by:

$$P_{ij} = -\rho \left[ (u'_i u'_k) \frac{\partial U_j}{\partial x_k} + (u'_j u'_k) \frac{\partial U_i}{\partial x_k} \right]. \quad (21)$$

The pressure-strain term varies depending on the specific turbulence model.

### 2.3.6 Speziale, Sarkar and Gatski Reynolds turbulence model

Speziale, Sarkar and Gatski (SSG) turbulence model was presented in 1991 (Speziale et al. 1991). It is based on the RSTM model, using a pressure-strain term defined as:

$$\begin{aligned} \phi_{ij} = & -(C_1 \rho \varepsilon + C_1^* p) b_{ij} + C_2 \rho \varepsilon \left( b_{ik} b_{kj} - \frac{1}{3} b_{mn} b_{mn} \delta_{ij} \right) + (C_3 - C_3^* \sqrt{b_{ij} b_{ij}}) \rho k S_{ij} \\ & + C_4 \rho k \left( b_{ik} S_{jk} + b_{jk} S_{ik} - \frac{2}{3} b_{mn} S_{mn} \delta_{ij} \right) + C_5 \rho k (b_{ik} \Omega_{jk} + b_{jk} \Omega_{ik}) \end{aligned} \quad (22)$$

where  $C_1$  to  $C_5$  are empirical constants;  $S_{ij}$  is the viscous strain rate, given by Equation (15);  $b_{ij}$  is the Reynolds stress anisotropy tensor, given by:

$$b_{ij} = -\frac{1}{2\rho k} \left( \rho u'_i u'_j + \frac{2}{3} \rho k \delta_{ij} \right); \text{ and} \quad (23)$$

$\Omega_{ij}$  is the mean rate of rotation tensor, given by:

$$\Omega_{ij} = \frac{1}{2} \left( \frac{\partial U_j}{\partial x_i} - \frac{\partial U_i}{\partial x_j} \right). \quad (24)$$

The SSG turbulence model is one among a class of turbulence models differentiated by the empirical constants employed in the RSTM formulation of Launder et al. (1975).

### 2.3.7 Baseline Reynolds turbulence model

Analogous to the Baseline  $k$ - $\omega$  model (refer to Appendix A), the Baseline (BSL) Reynolds turbulence model combines two turbulence models with a blending function, skewing the solution towards the better performing model depending on the local conditions. The model defines a formulation for  $\varepsilon$  in terms of  $\omega$ . Using a blending function, this formulation is adapted to the transport equation for  $\omega$ , giving:

$$\rho \frac{\partial \omega}{\partial t} + \rho \frac{\partial}{\partial x_i} (\omega U_i) = \frac{\partial}{\partial x_j} \left[ \left( \mu + \frac{\mu_T}{\sigma_\omega} \right) \frac{\partial \omega}{\partial x_j} \right] + \alpha \frac{\omega}{k} P_k - \beta \rho \omega^2 + (1 - F_1) 2\rho \frac{1}{\sigma_2 \omega} \frac{\partial k}{\partial x_k} \frac{\partial \omega}{\partial x_k} \quad (25)$$

where  $\sigma$ ,  $\sigma_\omega$ , and  $\sigma_2$  are empirical constants; and  $F_1$  is the blending function. All the empirical constants in the turbulence model have two values: one for the  $\omega$  regions, and one for the  $\varepsilon$  regions. These constants are calculated using the blending function, according to:

$$\theta_{BSL} = F_1 \theta_\omega + (1 - F_1) \theta_\varepsilon, \quad (26)$$

where  $\theta_{BSL}$  is the blended empirical constant;  $\theta_\omega$  is the empirical constant in the  $\omega$  regions; and  $\theta_\varepsilon$  is the empirical constant in the  $\varepsilon$  regions. Compared to turbulence models based on the eddy-viscosity hypothesis, there is little in the open literature that critically studies these RSTM based turbulence models.



### 2.3.8 Numerical solver

The numerical calculations to solve these transport equations were performed using ANSYS CFX 10.0<sup>22</sup>, a commercially available CFD package. The geometry of the flow problem is overlaid with a fine three-dimensional mesh, whose individual elements are used in the discretisation of the governing equations. The meshes were generated using ANSYS ICEM CFD 10.0<sup>22</sup>. The geometries used by the meshing software were developed in Autodesk Mechanical Desktop 2004 DX<sup>23</sup>. Further details regarding the meshing process and the geometry creation are included in the methodology descriptions for each experiment.

There is a variety of techniques that may be employed to discretise the governing equations across a mesh. CFX 10.0 uses a finite volume method whereby a volume is defined around each node, or point of the mesh, using the centroids of the surrounding surfaces. For the advection term, a high resolution blending scheme similar to that described by Barth and Jespersen is implemented (Barth et al. 1989). Near-wall calculations are treated by implementing an extension to the logarithmic formulations detailed by Launder and Spalding (Launder et al. 1974).

The process of discretisation can lead to staggered grids, in which some fluid dynamic terms are defined at volume boundaries, such as velocity, and others are defined within the volumes, such as pressure. CFX 10.0 avoids the need for staggered grids by using a

---

<sup>22</sup> ANSYS CFX 10.0 and ANSYS ICEM CFD 10.0 are copyright ANSYS Europe Ltd., 1996-2005.

<sup>23</sup> Autodesk Mechanical Desktop 2004 DX is copyright Autodesk Inc., 1983-2003.

method similar to Rhie-Chow collocation (Rhie et al. 1982) to locate all the fluid dynamic terms at the same position.

To speed convergence, an algebraic multigrid method is used in which virtual coarse meshes are created by joining adjacent mesh elements. Numerical solvers are efficient at reducing errors that have a wavelength close to the grid spacing, therefore by performing the calculations with a variety of grid spacings, errors occurring with a wider spectrum of wavelengths can be reduced.

### 3 Shroud design

A series of CFD models were developed to evaluate the effect of ducting on the output power of a kinetic turbine.

#### 3.1 Theory

The limitations of unshrouded turbines, and the benefits of using a shroud are discussed below.

##### 3.1.1 Turbine efficiency and the Betz limit

The power in a free-flowing stream tube is given by:

$$P_{\infty} = \frac{\rho u_{\infty}^3 A}{2}, \quad (27)$$

where  $u_{\infty}$  is the freestream velocity, and  $A$  is the cross stream area. When a turbine extracts power from the flow, it reduces the energy in the fluid around the turbine. This energy loss manifests itself as a pressure drop across the turbine rotor and shroud. Locally, there is an increase in pressure at the turbine leading edge, and a decrease at the trailing edge. The local high pressure area causes some of the upstream fluid to divert around the turbine, thus decreasing the amount of fluid passing through the turbine, which in turn reduces the amount of power available to the turbine, as shown in Figure 3.

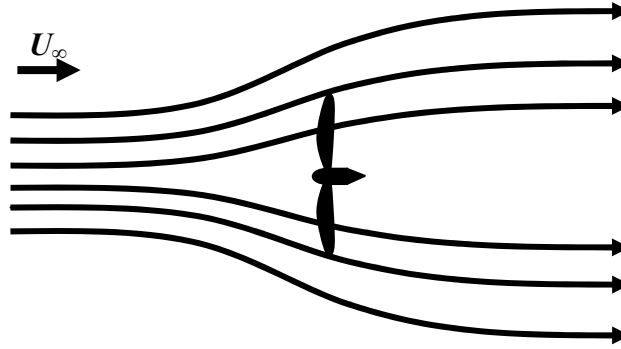


**Figure 3 – Flow through an unshrouded turbine**

As more power is extracted from the fluid, the pressure disturbance increases, further reducing the amount of fluid passing through the turbine. Therefore, there is a theoretical maximum to the total power that can be extracted from a fluid. This was proven in 1926 by Albert Betz (Betz 1926), and is known as the Betz limit. A summary of the derivation is presented here<sup>24</sup>. We begin by assuming that the velocity at the rotor is the average of the velocity in the wake and the freestream velocity:

$$u_t = \frac{1}{2}(u_w + u_\infty). \quad (28)$$

This assumption can be proven using a one-dimensional momentum and energy balance (Lewis et al. 1977). The mass flow rate through the rotor is

$$\dot{m} = \rho A u_t = \frac{1}{2} \rho A (u_w + u_\infty), \quad (29)$$

where  $A$  is the area swept by the rotor blades. Power is related to velocity changes by

$$P = \frac{1}{2} \dot{m} (u_\infty^2 - u_w^2). \quad (30)$$

<sup>24</sup> Adapted from windpower.org. Accessed 2007-01-09, available at: <http://www.windpower.org/en/tour/wres/betz.htm>

Substituting Equation (29) into Equation (30) gives the amount of power extracted by the turbine,

$$P = \frac{\rho A}{4} (u_{\infty}^2 - u_w^2) (u_w + u_{\infty}). \quad (31)$$

Finally, the Betz limit becomes apparent when this is compared with the power in the freestream,  $P_{\infty}$ . That is, dividing Equation (31) by Equation (27), we get

$$\frac{P}{P_{\infty}} = \frac{1}{2} \left[ 1 - \left( \frac{u_w}{u_{\infty}} \right)^2 \right] \left[ 1 + \frac{u_w}{u_{\infty}} \right], \quad (32)$$

and is represented Figure 4.

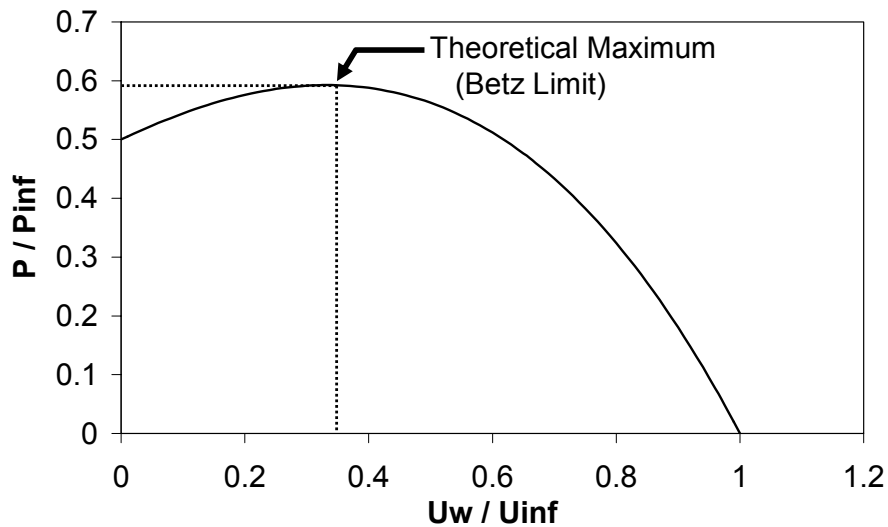


**Figure 4 – Power ratio versus velocity ratio**

The maximum of this function is the maximum power an ideal turbine will be able to extract from the fluid. This limitation is usually expressed by adding an efficiency term to Equation (27):

$$P_a = \frac{\eta \rho u_\infty^3 A}{2}, \quad (33)$$

where  $P_a$  is the power available, and  $\eta$  is the efficiency. The maximum possible value for  $\eta$  is approximately 16/27. That is, an ideal turbine will extract less than 60% of the total energy in the freestream.

### 3.1.2 Ducted turbine theory

A ducted turbine is a rotor enclosed by a shroud. The geometry of the shroud may be modified to increase the power available in the fluid passing through the turbine. For example, a nozzle at the inlet or a diffuser<sup>25</sup> at the outlet will increase the flow velocity through the turbine, which in turn will increase the power output. The use of a diffuser at the outlet may seem counter-intuitive as diffusers reduce flow speed and increase pressure. However, it is the upstream effect of this that benefits the turbine.

The shroud alters the flow field, increasing the volume of fluid passing through the turbine. The larger velocities give a larger density of power available to the turbine. The streamtube passing through each turbine is illustrated in Figure 5 with exaggerated distances for clarity.

---

<sup>25</sup> A nozzle is a fluid dynamic component in which the cross-sectional area of the channel narrows. A nozzle increases the velocity of the fluid, while reducing its pressure. Conversely, a diffuser is a component with a widening cross-section, causing a reduction in flow velocity and an increase in pressure.

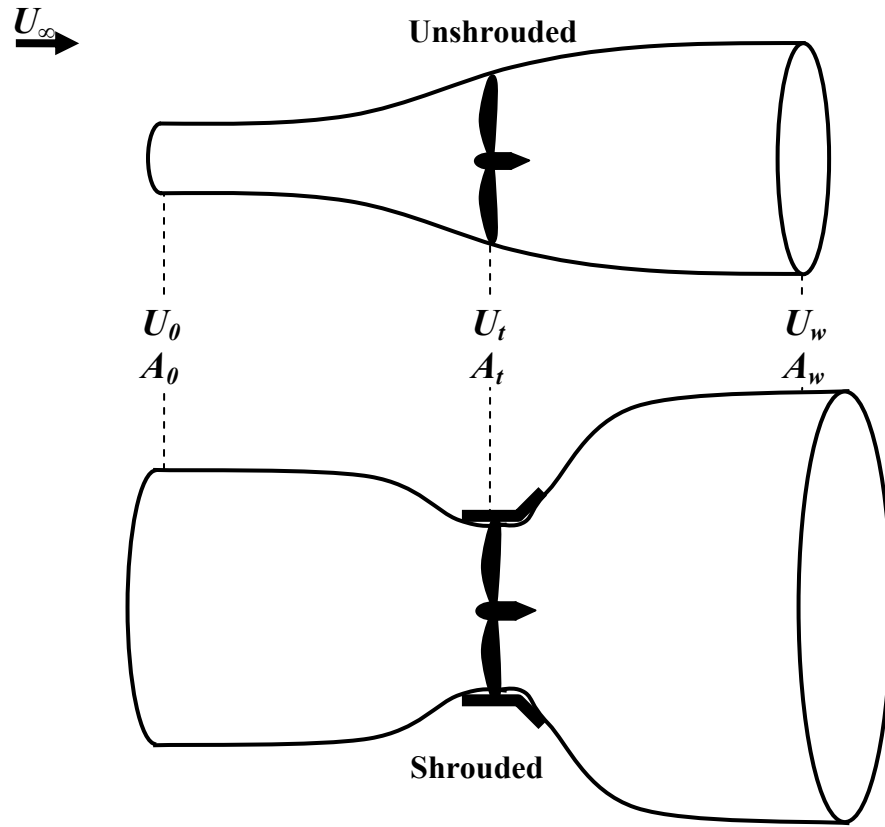


**Figure 5 – Streamtubes passing through a shrouded and unshrouded turbine**

The effect of a shroud can be demonstrated using thrust ratios (Lewis et al. 1977). When a shroud encloses the turbine, the total thrust is shared between the turbine and the shroud. The thrust ratio is given by:

$$\tau = \frac{T_t}{T}, \quad (34)$$

where  $T_t$  is the turbine thrust, and  $T$  is the total thrust. The power generated by an ideal shrouded turbine is:

$$P = \frac{1}{\tau} \left[ \frac{\rho A}{4} (u_\infty^2 - u_w^2) (u_w + u_\infty) \right] \quad (35)$$

For a diffuser, the thrust ratio  $\tau$  is less than unity, leading to a greater power output.

Although the shroud may increase the power output of kinetic turbines, it will also increase its drag. Drag impacts the cost of the technology by way of larger support structures and anchoring system. It is unknown whether the benefits of performance increases will outweigh the negative costs of drag for kinetic turbines as it is a complex optimization problem, made more complicated by the presence of ice floes and frazile ice issues. This explains why the research on kinetic turbines at the University of Manitoba also includes in-situ monitoring of these devices in rivers in collaboration with Manitoba Hydro and UEK (Bibeau 2006).

### **3.2 Turbine rotor modelling**

Due to its intricate geometry and rotational motion, the turbine rotor represents a significant complication in modelling. Four techniques are detailed below to handle the rotor section:

- No model;
- Momentum source;
- Averaging rotating reference frame; and
- Sliding mesh rotating reference frame.



### **3.2.1 No model**

The simplest solution is to perform the simulation with no turbine model. This model includes all the ducting, but the turbine simply becomes an unobstructed passage. This will exclude the pressure drop across the turbine as well as swirl effects.

The turbine introduces a non-linear feedback of the velocity through the shroud. Any velocity increase caused by a change in the shroud geometry will be affected by an increase in the pressure disturbance from the turbine. Attempting to model the shroud without a turbine is removing a significant variable from the problem. It is expected that the optimum shroud resulting from simulations with no turbine will be significantly different than a design resulting from simulations with a turbine model. Therefore, this type of model is not used in the design of the shroud.

### **3.2.2 Momentum source**

To simplify the numerical simulations, the turbine rotor can be modeled as a momentum source. In this model, the rotor is treated as a black box, where the energy is removed from the flow by introducing a momentum source term in the cylindrical region enclosing the turbine, as shown in Figure 6. This method has been used in many previous rotor modelling studies (Yihua et al. 2005), as well as for other complex flow problems (Koskela 2004).

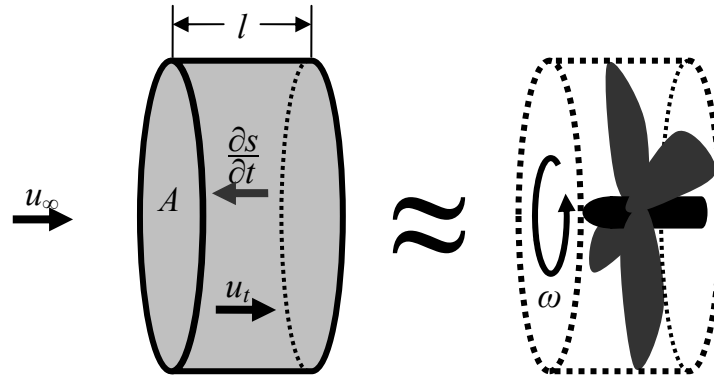


**Figure 6 – Momentum source**

### 3.2.2.1 Momentum source theory

In order to apply a momentum source term to the CFD simulation, the source needs to be applicable on the local level, both spatially and temporally. That is, instead of solving for the total momentum change, we are looking for the change in momentum per unit time, per unit volume (ANSYS 2005).

The total amount of power we wish to extract from the flow can be expressed as a fraction of the power available at the turbine:

$$P = kP_r = \frac{k\rho u_t^3 A}{2}, \quad (36)$$

where  $k$  is herein called the momentum source factor, an input parameter,  $P_r$  is the power available in the turbine region, and  $u_t$  is the velocity at the turbine. Power is related to momentum by:

$$P = \frac{\partial S}{\partial t} \left( \frac{d}{t} \right), \quad (37)$$

where  $S$  is momentum,  $d$  is the length through which the momentum changes, and  $t$  is the time the momentum change takes. Therefore, from Equations (36) and (37) the momentum change is:

$$\frac{\partial S}{\partial t} = k \frac{1}{2} \rho u_t^3 \left( \frac{t}{d} \right) A. \quad (38)$$

This momentum change is to be evenly distributed throughout the turbine region.

Therefore, the local momentum change is:

$$\frac{\partial s}{\partial t} = \frac{k}{2\mathcal{V}} \left( \frac{t}{d} \right) \rho u_t^3 A, \quad (39)$$

where  $s$  is the momentum change per unit volume,  $\mathcal{V}$  is the volume of the turbine region:

$$\mathcal{V} = lA, \quad (40)$$

and since  $t$  is the time for a fluid particle to pass through the momentum source region, and  $d$  is the length of the momentum source region, we have:

$$\frac{t}{d} = u_t. \quad (41)$$

Finally, Equations (39), to (41) give:

$$\frac{\partial s}{\partial t} = k \frac{\rho u_t^2}{2l}. \quad (42)$$

The term  $u_t$  is a problem for the CFD simulations because it is not actually a local quantity. For simplification, local velocity  $u$  will be used instead. The effect this assumption may have on the simulation is addressed later in Section 3.2.2.2.

$$\frac{\partial s}{\partial t} = k \frac{\rho u^2}{2l} \quad (43)$$

This is the momentum change per unit volume per unit time, and is the final form used in the momentum source simulations. The use of the momentum source requires analytic calculations to yield the power and drag from the results of the simulations. Power is given by:

$$P_t = \frac{k\rho u_t^3 A}{2}, \quad (44)$$

and the turbine drag is calculated using:

$$F_t = P_t \frac{t}{l} = \frac{P_t}{u_t}. \quad (45)$$

The total drag is the sum of the drag on the shroud / diffuser assembly and the turbine drag:

$$F_{total} = F_t + F_s = \frac{P_t}{u_t} + F_s, \quad (46)$$

where  $F_s$  is the drag on the shroud assembly, a quantity that can be extracted from the numerical results by integrating the pressure distribution on the shroud assembly.

### 3.2.2.2 Momentum source error analysis

It is important to remember the momentum source method is an approximation, especially when using Equations (44) and (46). The nature of any black box method is that it cannot predict what takes place within the black box. That is, the output solution cannot be trusted within the region of the momentum source. Unfortunately, to calculate power and drag we need  $u_t$ , a quantity requiring averaging throughout the momentum

source region. It is important to understand this effect when analysing the simulation results.

The momentum source Equation (43) uses local velocity instead of average velocity. Therefore, the momentum source will see a larger distribution of velocities than it should. Since it depends on the square of the velocity, the larger values of  $u$  will tend to produce a general bias towards a higher momentum. Therefore too much momentum will be extracted from the fluid. The power Equation (44) is proportional to the cube of the velocity, therefore it will also suffer from this effect, resulting in an over-prediction of the power output. This over-prediction is in addition to the omission of the power converting devices – bearings, seals, gears, alternator and power electronics – which further reduces the effective power generation.

A Monte Carlo experiment was performed to demonstrate these effects. A dataset of 1000 velocities was randomly generated with varying distributions, using a mean velocity of 1.0. The square and cube of the mean velocity are both unity; however, if the mean is taken after squaring or cubing as occurs in Equation (43), the result is perturbed. The perturbation factors are calculated using:

$$A = \frac{N \sum_{i=1}^N (u_i^2)}{\left[ \sum_{i=1}^N (u_i) \right]^2} \quad \text{and} \quad B = \frac{N \sum_{i=1}^N (u_i^3)}{\left[ \sum_{i=1}^N (u_i) \right]^3}, \quad (47)$$

where  $A$  represents the perturbation factor seen in an equation using  $u^2$ , and  $B$  represents the perturbation factor seen in an equation using  $u^3$ . The results of these simulations are shown in Figure 7.

$$\frac{1}{N} \sum_{i=1}^N (u_i^2) \quad \frac{1}{N} \sum_{i=1}^N (u_i^3)$$

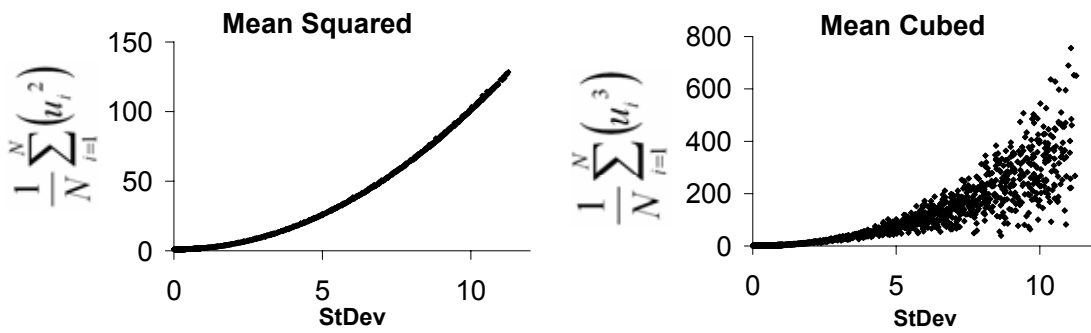


**Figure 7 – Perturbation factors: (a) squared functions  $u^2$ ; (b) cubic functions,  $u^3$ .**

As shown in Figure 7, larger distributions of velocity will lead to artificially larger values for  $u^2$ , and  $u^3$ .

The error in the CFD simulations is difficult to quantify. In fact, it is unknown whether the data can even be interpreted qualitatively. Furthermore, it is not known if the optimum case will be the same between a momentum source model and a rotating reference frame model.

A numerical experiment was performed and compared against the Betz theory to evaluate the performance of the momentum source model. For this experiment, a cylindrical

momentum source was placed in a freestream with uniform flow. There were no walls, apart from the symmetry-planes at the edges of the mesh. The only variable was  $k$  in the momentum source Equation (43), effectively altering the efficiency of the turbine. Nineteen simulations were performed with  $k$  ranging from 0 to 20. After the each numerical simulation converged, the power output was calculated from Equation (44). Efficiency was calculated by dividing the power output by the power available in the freestream. Wake velocity was determined from the flow field.

The velocity ratio and power ratio are plotted below in Figure 8, analogous to Figure 4. Note that the velocity ratio extends to the negative side of the graph. This is not physically realistic, but since the model is of a momentum source, then momentum can be added to the point that the wake velocity is negative.

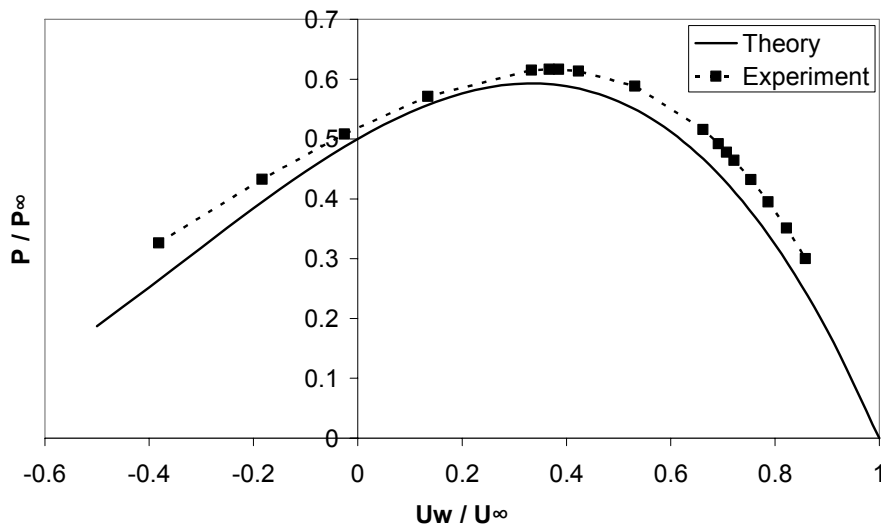


**Figure 8 – Momentum source versus theory**

The figure shows that the momentum source model is close to the theory. Although there is an obvious over-prediction of the power output, the over-prediction is fairly consistent

at around 5%, and the trend is correct. Another result of the experiment is the relationship between the momentum source factor  $k$  and the turbine efficiency  $\eta$ . Comparing the equations for the momentum source power in Equation (44) and power available in Equation (33) gives the impression that  $k$  is equivalent to  $\eta$ :

$$P_t = \frac{k\rho u_t^3 A}{2}, \quad \text{and} \quad P_a = \frac{\eta\rho u_\infty^3 A}{2}.$$

Results from the experiment show this is not the case. As seen in Figure 9, the relationship between  $k$  and  $\eta$  is more complex.

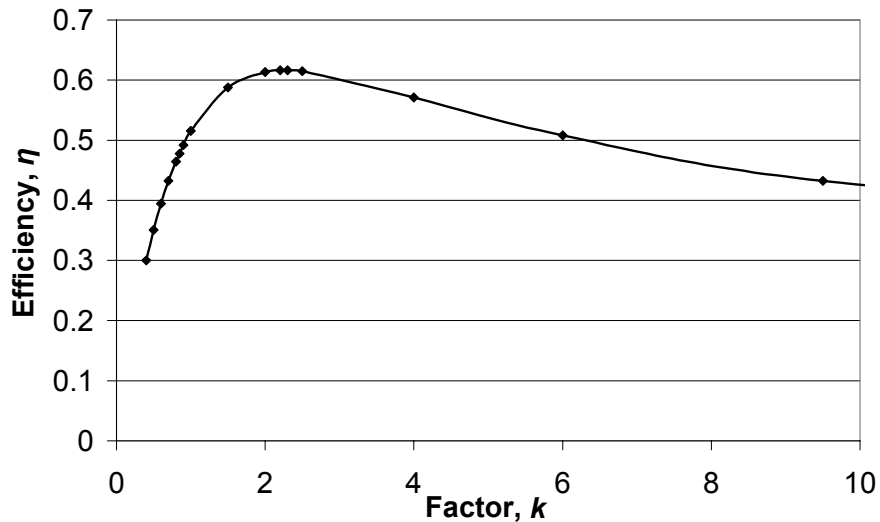


**Figure 9 – Efficiency,  $\eta$  versus factor,  $k$**

In the momentum source model,  $k$  is a factor applied locally at the turbine. Overall efficiency  $\eta$  is the fraction of the power output to the power in the freestream. Although the equations seem similar, they behave differently.



### 3.2.3 Averaging rotating reference frame

The momentum source model does not incorporate the geometry of the turbine; rather it uses a single variable,  $k$  to account for variations in geometry. The averaging rotating reference frame (ARRF) is a means of including the turbine geometry without requiring a transient numerical solution.

Two geometric regions are defined: a cylindrical rotating region enclosing the rotating parts, and a static region. Between the two regions are interface surfaces. Within the region of rotation, the governing equations are modified. The momentum equations include an additional source to account for centripetal forces, which, in vector notation is:

$$S_{M,rot} = -2\rho\omega \times \mathbf{U} - \rho\omega \times (\omega \times r), \quad (48)$$

where  $\omega$  is the vector of angular rotation;  $\mathbf{U}$  is the velocity vector relative to the rotating frame of reference; and  $r$  is the vector from the axis of rotation.

To avoid the necessity of a transient solution, the ARRF model uses circumferential averaging. At the interface surfaces, all fluid dynamic properties are averaged along the circumference of rotation. Therefore the final solution is static. This is an approximation; however it allows one to study the flow as it passes through the rotor. The solution is restricted to axisymmetric geometries with flow along the axis of symmetry.

### **3.2.4 Sliding mesh rotating reference frame**

The sliding mesh rotating reference frame model (SMRRF) is a calculation intensive method that captures the transient effects of the turbine. Rather than using circumferential averaging, the SMRRF model animates the turbine, producing a new mesh for each numerically converged iteration. The turbine region is rotated, and an interpolative method is used to connect elements together at the interface surfaces. The resulting simulation is transient, and the calculation time and output is several times longer than the ARRF model. Use of the SMRRF may be required, particularly if the shroud geometry is asymmetrical. Due to its computational intensity and the symmetrical nature of horizontal kinetic turbines, this model is not used in this study.

### **3.3 Shroud optimization experiment using a momentum source model**

Using a momentum source model for the turbine, a series of numerical experiments are performed to optimize the shroud geometry.

#### **3.3.1 Problem definition**

A series of numerical experiments are performed to evaluate the effect of installing a shroud on a river kinetic turbine. The experimental variables are diffuser angle and area ratio. The experimental parameters are outlined in Table 3.

**Table 3 – Momentum source experiment parameters**

| <b>MOMENTUM SOURCE EXPERIMENT</b> |  |                           |
|-----------------------------------|--|---------------------------|
| <b>EXPERIMENT</b>                 | Objective  |                           |
|                                   | Evaluate the effect of ducting on the power output of a kinetic turbine using a momentum source modelled turbine |                           |
|                                   | <b>Variable</b>  | <b>Trials</b>             |
|                                   | Area ratio   | 18                        |
|                                   | Angle  | 8                         |
|                                   | Momentum source factor   | 18                        |
| <b>FLUID SPACE</b>                | X (streamwise)   | 28.00 [m]                 |
|                                   | Y (cross stream)   | 15.00 [m]                 |
|                                   | Z (vertical)   | 15.00 [m]                 |
| <b>INLET</b>                      | Velocity   | 3.0 [m/s]<br>Uniform flow |
|                                   | Turbulence Intensity   | 0.10<br>("High" default)  |
|                                   | Eddy viscosity ratio   | 100<br>("High" default)   |
|                                   | <b>OUTLET</b>  | Outlet Pressure           |
| <b>BOUNDARY WALLS</b>             | Side walls ( $\pm Z$ )   | Symmetry plane            |
|                                   | Top wall (+Y)  | Symmetry plane            |
|                                   | Bottom wall (-Y)   | Symmetry plane            |
| <b>MESH</b>                       | Type   | Hexahedral                |
|                                   | Variations   | 26                        |
|                                   | Average size   | 713,000 elements          |

The model, with dimensions shown in Figure 10 is immersed in a body of fluid. The inlet has a uniform velocity of 3 m/s with a turbulence intensity of 0.1. The outlet has an imposed average static pressure of 0 kPa. The remaining walls are symmetry planes. The shroud was modeled as a cylindrical wall enclosing the turbine, and a conical wall as a diffuser. The ratio of the outlet area to inlet area and the diffuser angle were the design variables.

The standard  $k-\varepsilon$  turbulence model was found to be successful in modelling diffuser flow (Lai et al. 1989), although a Reynolds stress turbulence model has been found to be perform better (Cho et al. 1991) for internal flows. The standard  $k-\varepsilon$  was used for this simulation.

Convergence criteria is the criteria used to determine when the numerical solution is adequate close to the governing equations to warrant stopping numerical iterations.

When the maximum root mean square (RMS) of the residuals was less than  $10^{-4}$ , the solver was stopped.

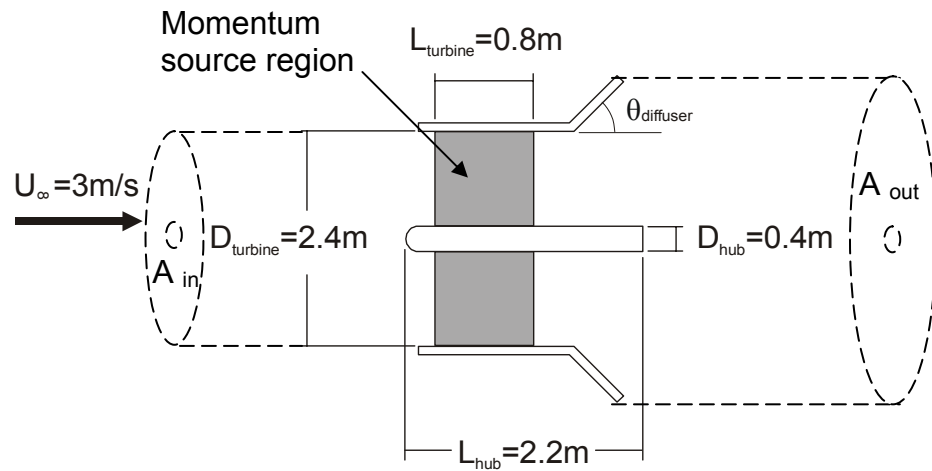


**Figure 10 – Shroud experiment dimensions**

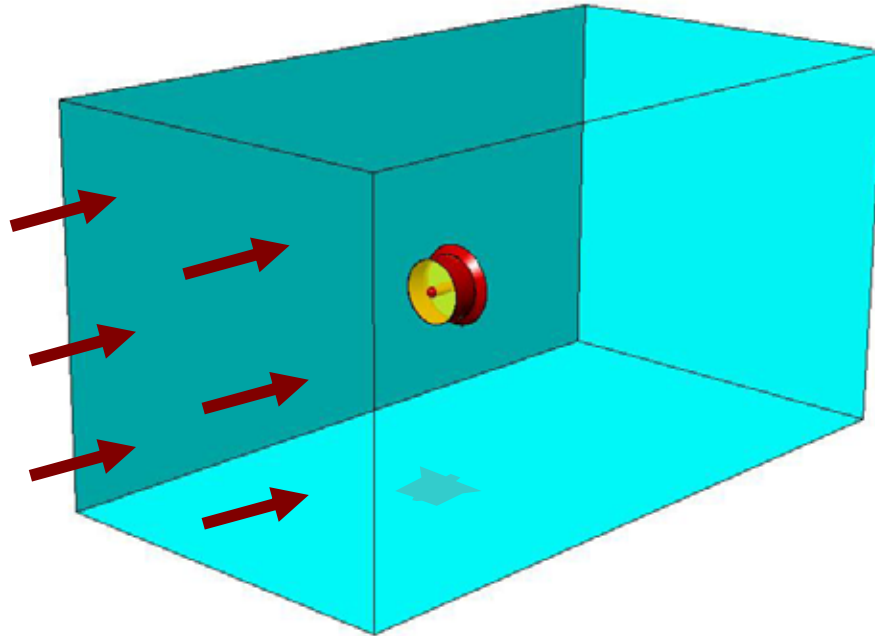


**Figure 11 – Shroud experiment flow domain**

The flow domain shown in Figure 11 presents a challenge for mesh generation. A high mesh density is desired; however the large external flow domain would produce an unmanageably large mesh. To accommodate the conflicting requirements, the mesh density is varied from a high density near the model to a lower density near the boundaries. Due to the relatively simple, axisymmetric geometry, a structured, hexahedral mesh is used, as shown in Figure 12. Grid independence and  $Y^+$  values were not considered over the course of this experiment.

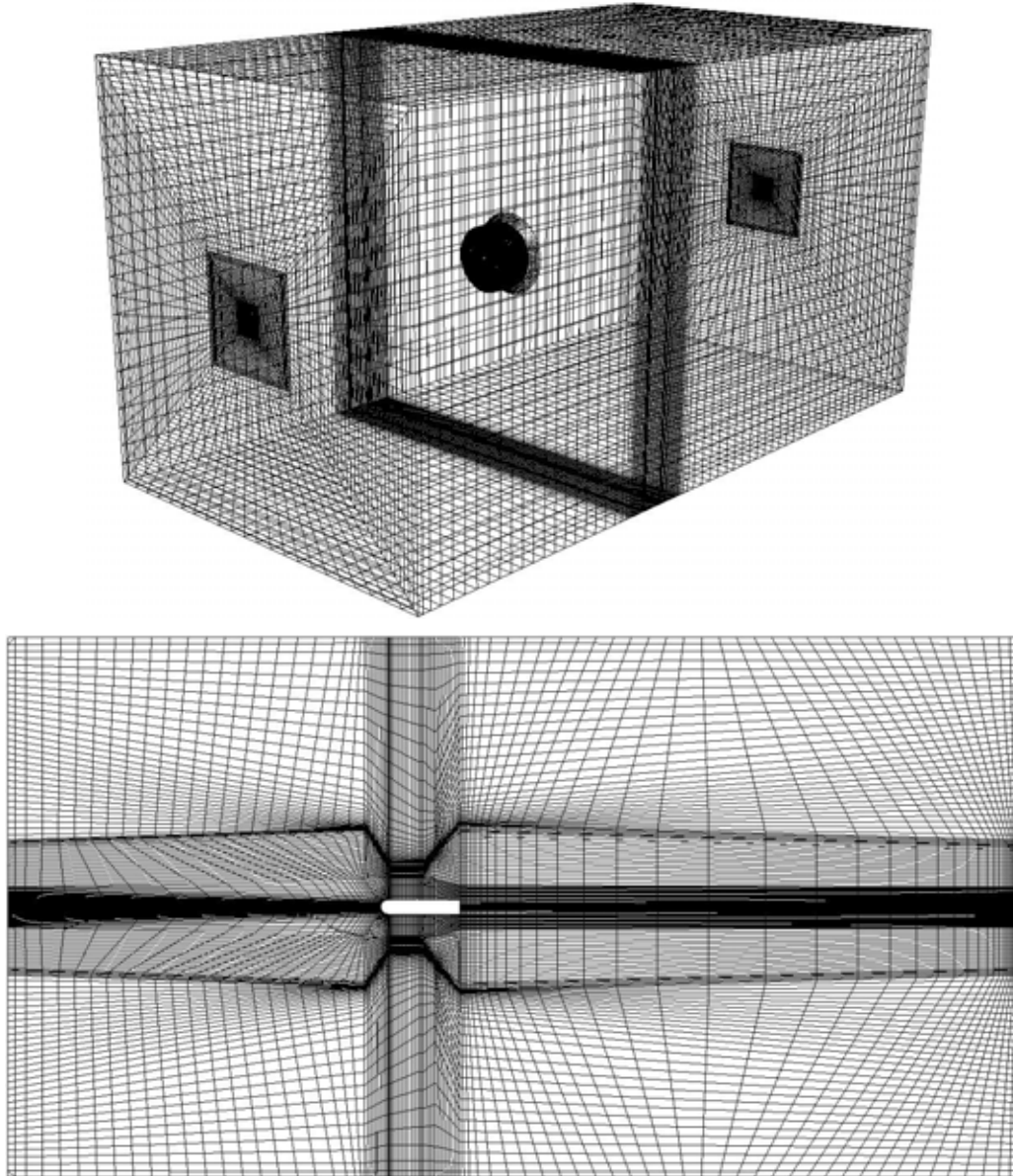


**Figure 12 – Shroud experiment 3-D surface mesh and 2-D mesh slice**

A momentum source model (see Section 3.2.2) is used for the main experiment, with factor  $k$  set to 0.5, giving an approximate turbine efficiency,  $\eta$  of 35.0% (see Figure 9). The first experimental parameter to be investigated is the area ratio. Once the optimum area ratio is found, this parameter was fixed, and the diffuser angle is investigated. The simulation parameters are summarized in Table 3.

### 3.3.2 Results and discussion

The results from the area ratio simulations using a momentum source are shown in Figure 13.

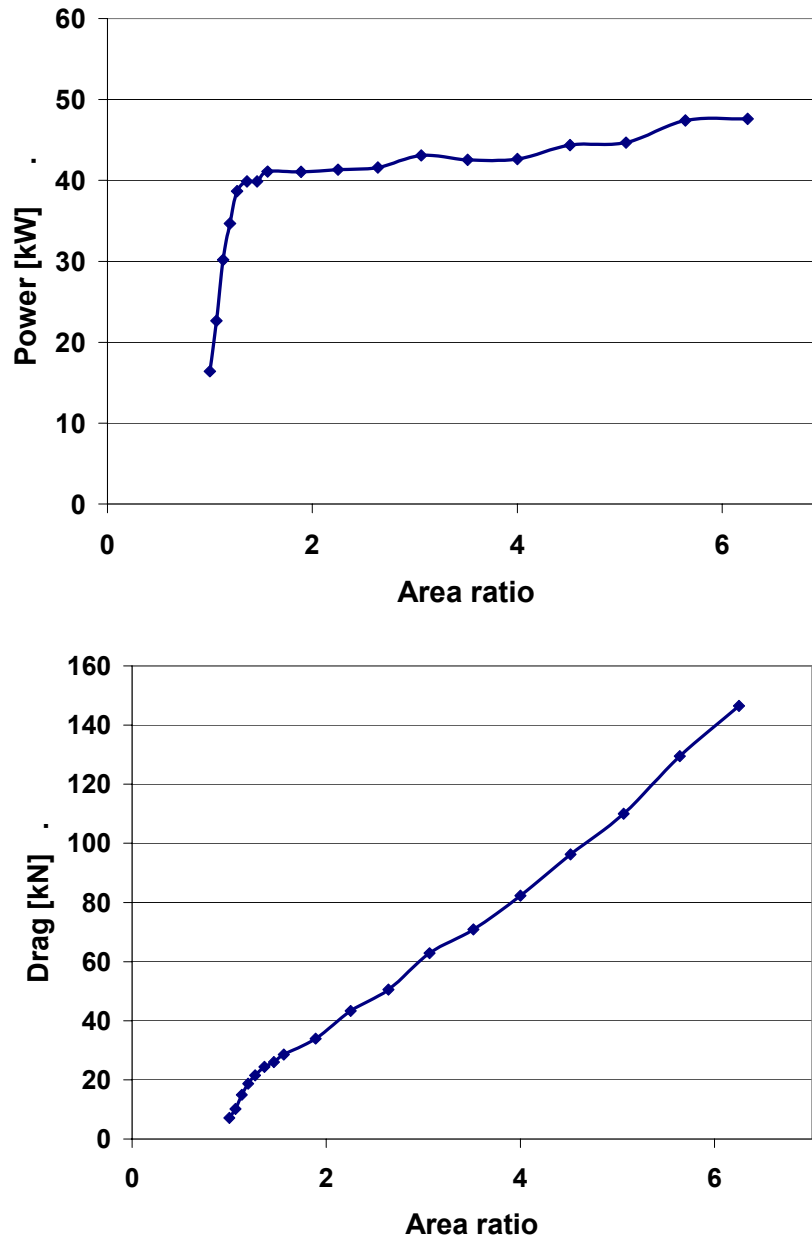


Figure 13 – (a) Power and (b) drag versus area ratio

The power output initially increases sharply with the area ratio, rising from 16.4 kW for no diffuser to 41.1 kW for an area ratio of 1.56. That is an increase of a factor of 2.5 where the diffuser radius grew by less than 30 cm. The trend levelled off beyond this size of diffuser, giving only small benefits to an increasing diffuser size. This is intuitively expected due to separation. Total drag responded almost linearly to area ratio. Drag impacts the cost of the technology by way of larger support structures. Furthermore, larger sizes are not desirable because this will limit the site selection to rivers with larger cross-sections. Therefore any increase in diffuser size must carefully be balanced with its negative effects. An area ratio of 1.56 was chosen as the best compromise, translating to an outside diameter of 3.0 meters, with a turbine rotor diameter of 2.4 meters.

The diffuser angle has a more complicated impact on the performance of the turbine, as shown in Figure 14. Power output is greatest at shallow diffuser angles of 20° to 30°, and drops off at angles outside of this. Drag shows a slight drop with decreasing angle, thus the power gained by optimizing the diffuser angle is not offset by any additional drag force. The change in drag was moderated by opposite trends in the turbine drag and diffuser drag.



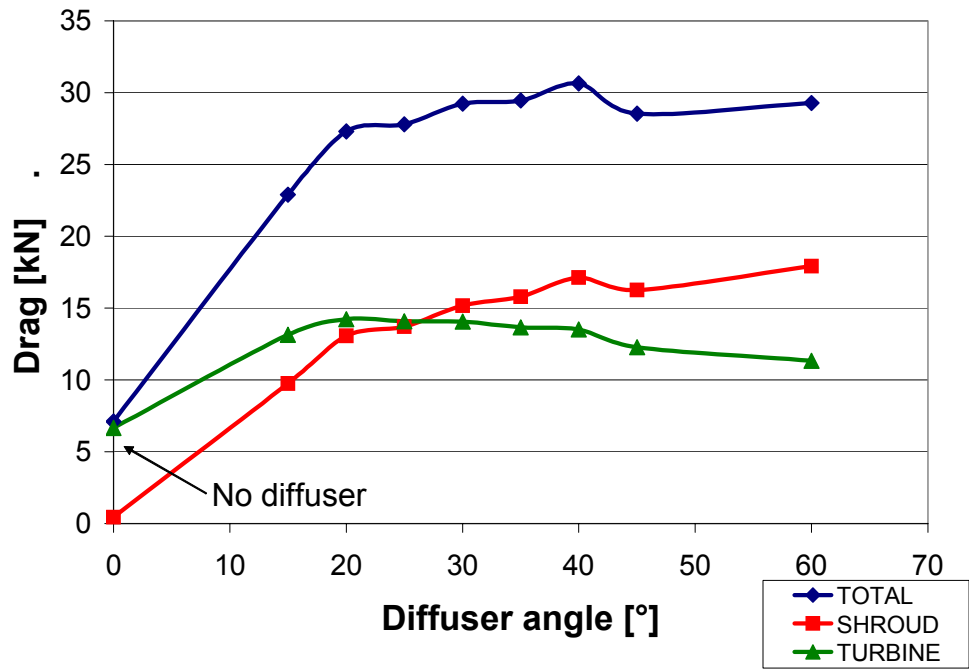
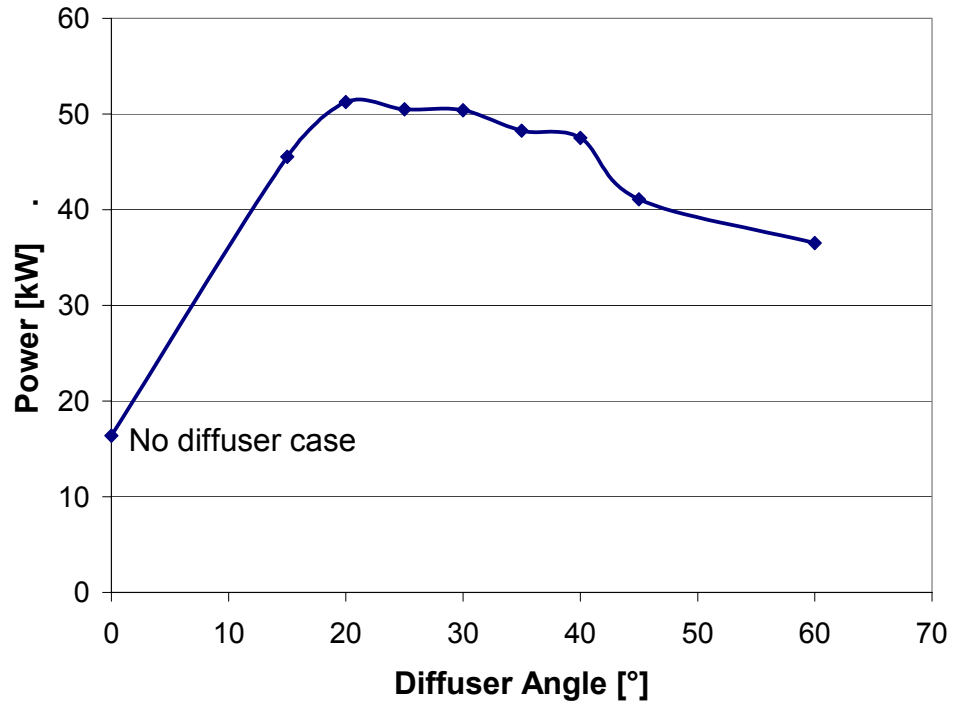
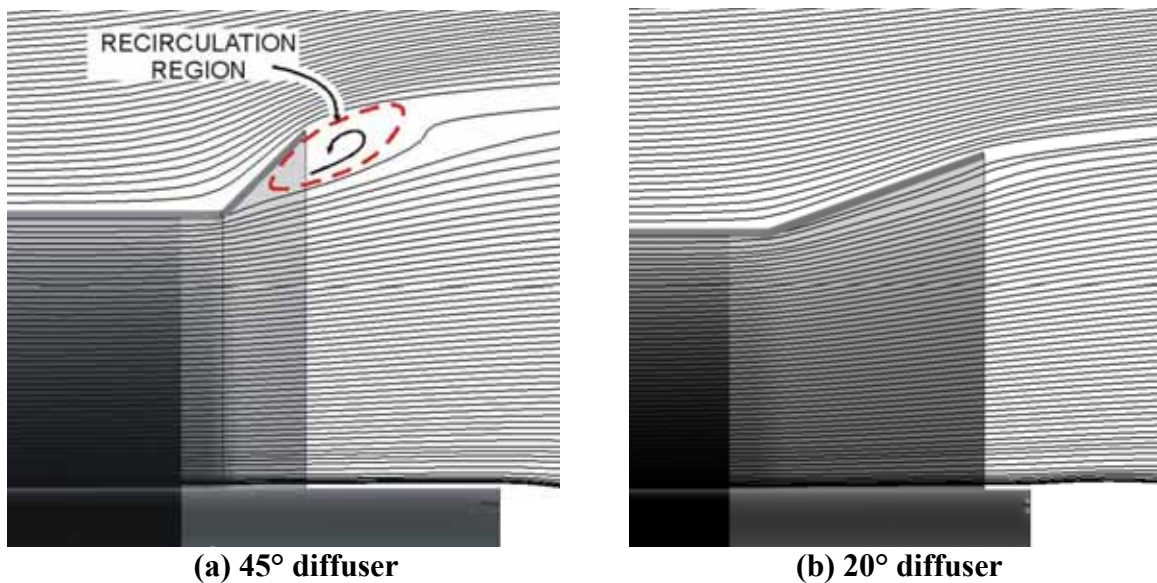


Figure 14 – (a) Power and (b) drag versus diffuser angle

Streamlines for the 20° and 45° diffusers are shown in Figure 15. There is a significant recirculation region in the 45° case that is not present in the 20° case. The optimized

diffuser angle most closely follows the streamlines as they exit the diffuser. Therefore it is likely that the optimum diffuser angle is a function of the freestream velocity. If this relationship can be determined, an adjustable diffuser can be developed that will make the turbine more versatile. This angle may be adjusted during maintenance, or even electronically controlled. It may be possible to construct the diffuser from a flexible material that will bend to the optimum angle, given the load conditions of the freestream. Debris in the river is a factor that must also be considered as this could damage the diffuser and add to the maintenance costs. The strength of the diffuser and its angle may cause it to be more susceptible to damage. A shallower angle is less likely to be exposed to strong impacts, especially when log collisions are expected.



**Figure 15 – Streamlines for the (a) 45° and (b) 20° diffusers**

It is worth noting that a strong relationship became apparent between diffuser angle and CFD computational time. As the diffuser angle increased, the convergence time also

increased. Whereas the 20° diffuser required less than 30 minutes to converge, the 60° diffuser required over 3,000 minutes (2 days) to converge. This is likely caused by the increasing complexity in the wake flow.

In Figure 16, the effect the diffuser has on the flow is demonstrated. The streamlines at the inlet of the turbine with no diffuser are divergent; whereas they are converging when a diffuser is present. Furthermore, the wake flow shows a larger recovery area when a diffuser is present, suggesting a larger pressure difference. This is analogous to Figure 5.

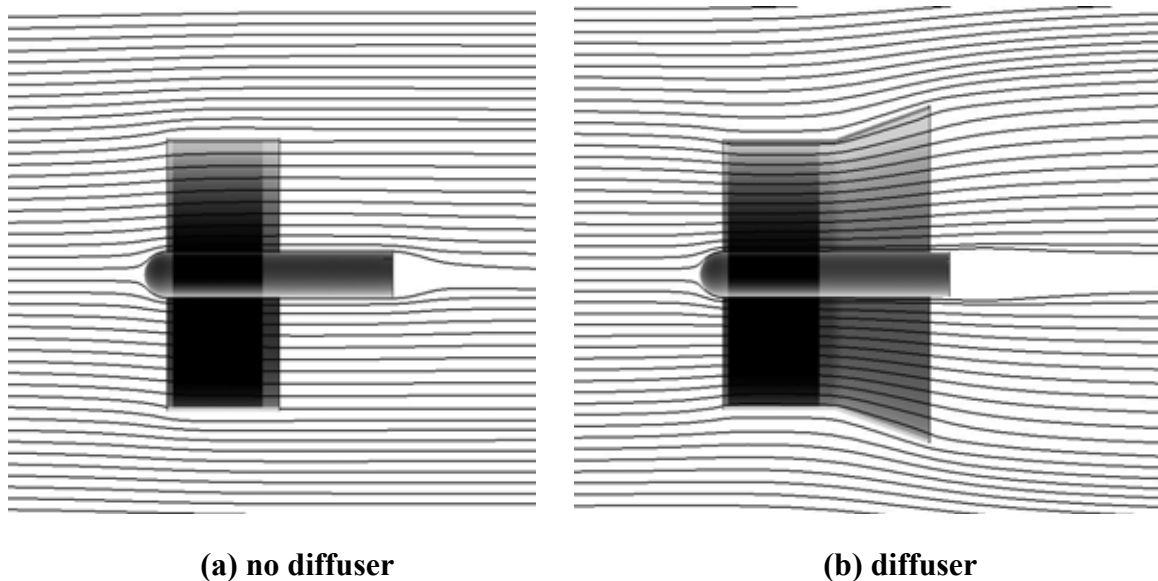


**Figure 16 – Streamlines around turbine configured (a) without and (b) with a diffuser**

The axial component of velocity at the centre line plane is shown in Figure 17. This plot illustrates the benefit of a diffuser, where the maximum axial velocity through the turbine is 2.8 m/s with no diffuser, compared to 4.1 m/s with a diffuser.

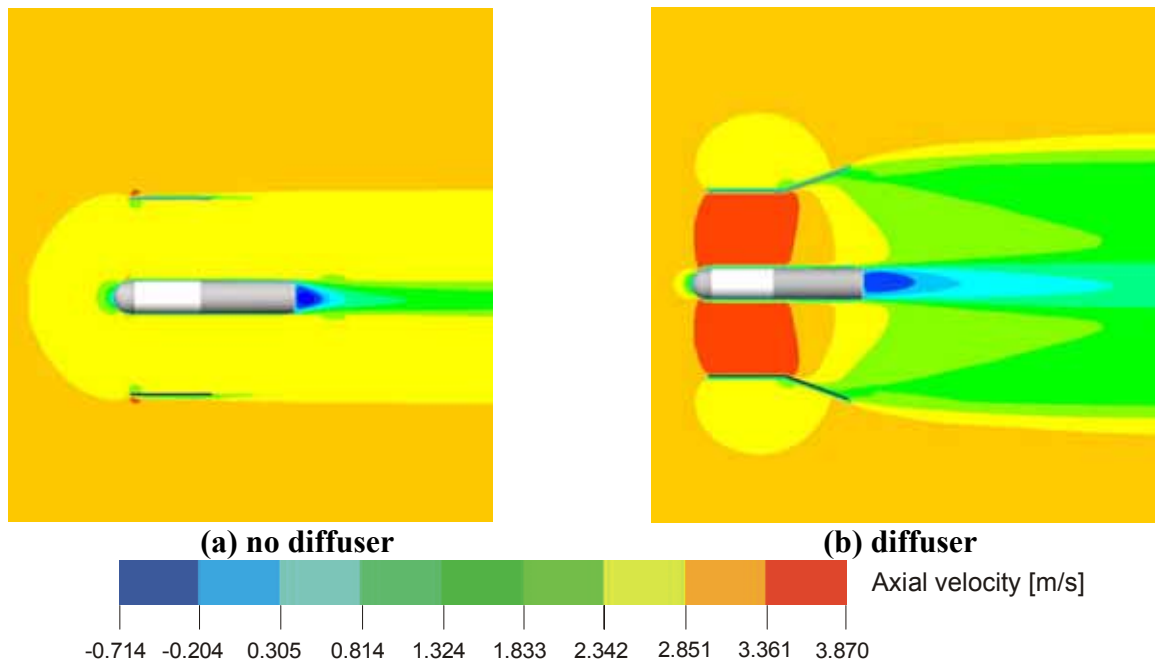


**Figure 17 – Axial velocity, (a) without and (b) with a diffuser**

The optimum case was a 20° diffuser with an area ratio of 1.56, or 3.0 meter diameter diffuser. In this case, power was increased by a factor of 3.1 compared to the turbine with no diffuser. Drag increased by a factor of 3.9.

In the optimal configuration, the turbine produced 51.3 kW of power. By way of comparison, the power in the freestream was 59.3 kW, giving an overall efficiency of 86.5%, a value that is well above the Betz limit. Therefore, this configuration exceeds the Betz limit by a factor of 1.45.

The Betz limit is fundamentally tied to continuity. Therefore any alleged violation of Betz limit also implies a violation of continuity. The use of a diffuser appears to defeat the Betz limit, but that is not actually the case. The area swept by the turbine rotor is used to calculate the efficiency; however if we used the total cross stream area, the turbine performs within the Betz limit. Based on the largest characteristic diameter – the diameter of the diffuser – the power in the freestream is 95.3 kW. Compared against this, the efficiency of the turbine is 53.8%, a value that is consistent with the Betz limit.

With a limited cross sectional area, the use of a diffuser reduces the size of the turbine. It is therefore important to understand whether there is a benefit to using a diffuser, rather than using a larger turbine. Scaling the results of the turbine with no diffuser from 2.4 m diameter to 3.0 m gives a power output of 25.6 kW. Conversely, a 2.4 m diameter turbine with a 3.0 m diameter diffuser produced 51.3 kW. Therefore, sacrificing turbine size to include a diffuser seems productive based on the simulation results. Again, these do not include other effects like the losses in the power generation equipment, rotational speed and blade geometry.

### **3.4 Rotating reference frame**

A series of simulations are performed using the ARRF turbine model, as described in Section 3.2.3.

#### **3.4.1 Turbine design and meshing**

Design optimization of the turbine blades was outside the scope of the research objectives, therefore a simplified technique was employed to obtain a working geometry.

A turbine blade is an airfoil section that is twisted helically around a central hub. As the distance from the hub increases, the angle of twist and chord length change. The angle of twist can be calculated based on angular velocity and the freestream flow.

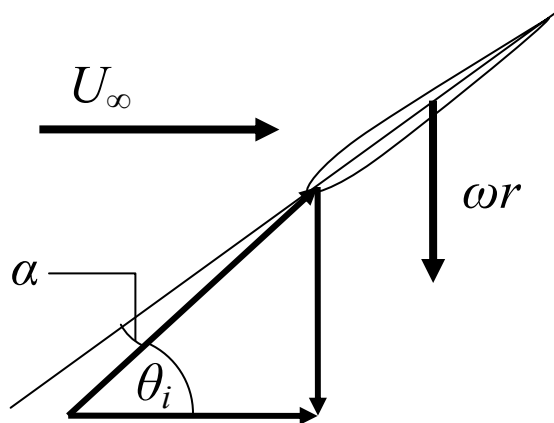


**Figure 18 – Velocity vectors at the turbine blade**

The angle of incidence,  $\theta_i$  is the angle of the freestream flow from the reference frame of the turbine blade. It can be calculated by geometry:

$$\theta_i = \tan^{-1}\left(\frac{\omega r}{U_\infty}\right), \quad (49)$$

where  $\omega$  is the angular velocity of the turbine blades, and  $r$  is the distance from the axis of rotation. Angle of attack,  $\alpha$  is the angle at which the turbine airfoil cross section meets the flow.

A NACA0012 airfoil profile was used for the turbine blades as this can be used in the design of propellers. The turbine was modelled assuming an angular velocity of 50 RPM, and a freestream velocity of 2.2 m/s. To create the blade, eleven cross-sections were plotted and interpolated using a cubic loft function available in the 3D geometry software, Autodesk Mechanical Desktop<sup>23</sup>. Airfoil profiles were drawn on Cartesian planes, rather than cylindrical planes concentric to the axis of rotation. This has the effect of exaggerating the airfoil profile on its chord-wise ends. The chord lengths followed a cubic function whose parameters were set by inspection. Details of the turbine blade are shown in Table 4. The turbine blade geometry is shown in Figure 19 and resembles the UEK design that will be tested in the Winnipeg River (Bibeau 2006).

**Table 4 – Turbine blade details**

| <b>Station</b> | <b>Radius<br/>[m]</b> | <b>Angle<br/>[°]</b> | <b>Chord<br/>[m]</b> |
|----------------|-----------------------|----------------------|----------------------|
| 0              | 0.1524                | 29.33                | 0.1524               |
| 1              | 0.2794                | 43.62                | 0.9144               |
| 2              | 0.4674                | 58.04                | 0.4674               |
| 3              | 0.5613                | 63.18                | 0.5613               |
| 4              | 0.6553                | 67.33                | 0.6553               |
| 5              | 0.7493                | 70.72                | 0.7493               |
| 6              | 0.8433                | 73.52                | 0.8433               |
| 7              | 0.9373                | 75.85                | 0.9373               |
| 8              | 1.0312                | 77.83                | 1.0312               |
| 9              | 1.1252                | 79.52                | 1.1252               |
| 10             | 1.2192                | 80.98                | 1.2192               |

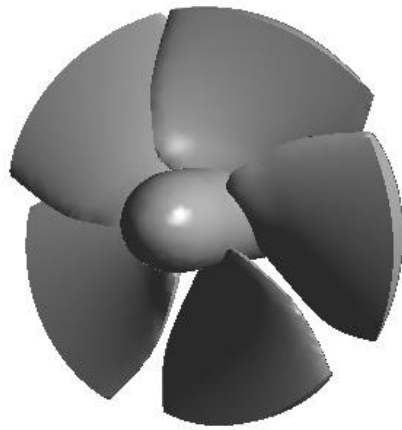


**Figure 19 – Turbine model**

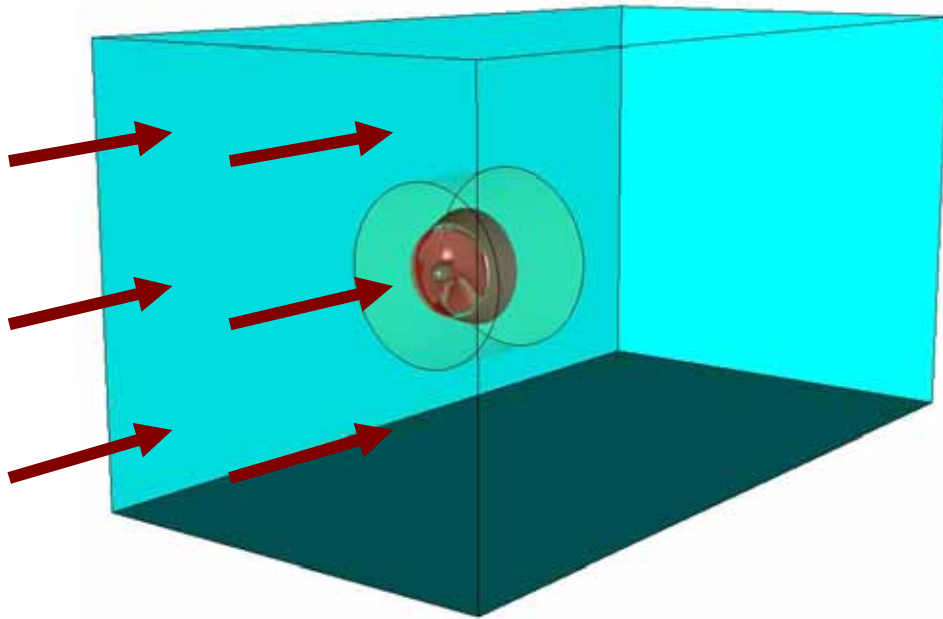


**Figure 20 – ARRf flow domain**

The same trade-off exists with a high mesh density desired, and a large external flow domain, as shown in Figure 20. Due to the complexity of the model, a hybrid mesh was



used, as shown in Figure 21. The bulk of the fluid was modelled using hexahedral elements to reduce the number of elements required in the open space, with a cylindrical volume omitted for the turbine. The turbine was modelled with tetrahedrons to facilitate rapid meshing, as shown in Figure 22.

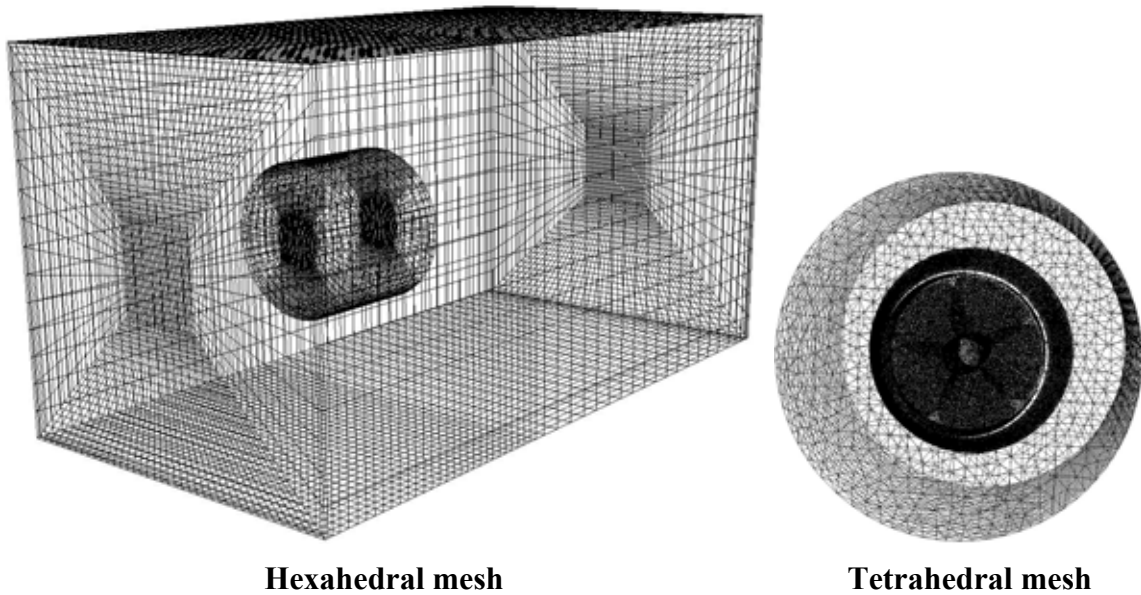


**Figure 21 – ARRF 3-D surface mesh**

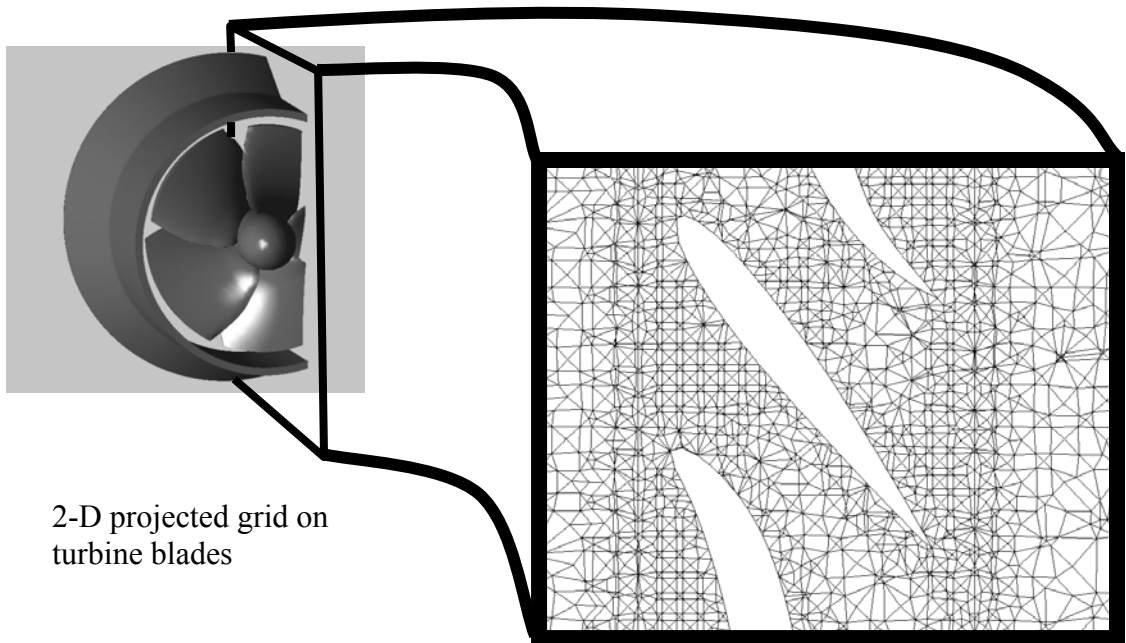


**Figure 22 – Sample mesh at the turbine blades**

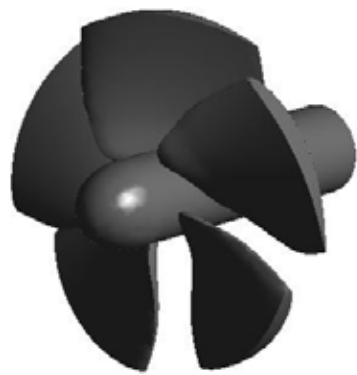
The rotating reference frame simulation parameters are shown in Table 5.

**Table 5 – Rotating reference frame experiment parameters**

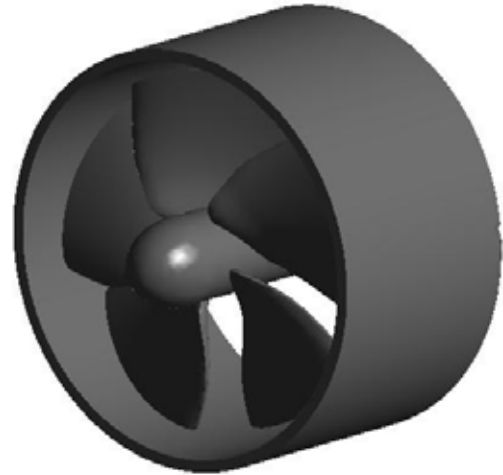
| <b>ROTATING REFERENCE FRAME EXPERIMENT</b> |  |                           |
|--|--|---------------------------|
| <b>EXPERIMENT</b>                          | Objective  |                           |
|  | Verify the results of the momentum source model against a rotating reference frame model |                           |
|  | <b>Variable</b>  | <b>Trials</b>             |
|  | Velocity   | 2                         |
|  | Configuration  | 4                         |
| <b>FLUID SPACE</b>                         | X (streamwise)   | 24.38 [m]                 |
|  | Y (cross stream)   | 12.70 [m]                 |
|  | Z (vertical)   | 12.70 [m]                 |
| <b>INLET</b>                               | Velocity   | 3.0 [m/s]<br>Uniform flow |
|  | Turbulence Intensity   | 0.10<br>("High" default)  |
|  | Eddy viscosity ratio   | 100<br>("High" default)   |
| <b>OUTLET</b>                              | Outlet Pressure  | 0 [kPa]                   |
| <b>BOUNDARY WALLS</b>                      | Side walls ( $\pm Z$ )   | Symmetry plane            |
|  | Top wall (+Y)  | Symmetry plane            |
|  | Bottom wall (-Y)   | Symmetry plane            |
| <b>MESH</b>                                | Type   | Hybrid                    |
|  | Variations   | 5                         |
|  | Average size   | 737,000 elements          |

### 3.4.2 Methodology

The optimum design from the momentum source experiment (see Section 3.3) was verified using a rotating reference frame turbine model (see Section 3.2.3). Four trials were conducted: no shroud; shrouded with no diffuser; with the optimum diffuser alone; and with both the shroud and the optimum diffuser, as shown in Figure 23. Other parameters were set to be identical to the momentum source experiment, with an inlet velocity of 3.0 m/s.



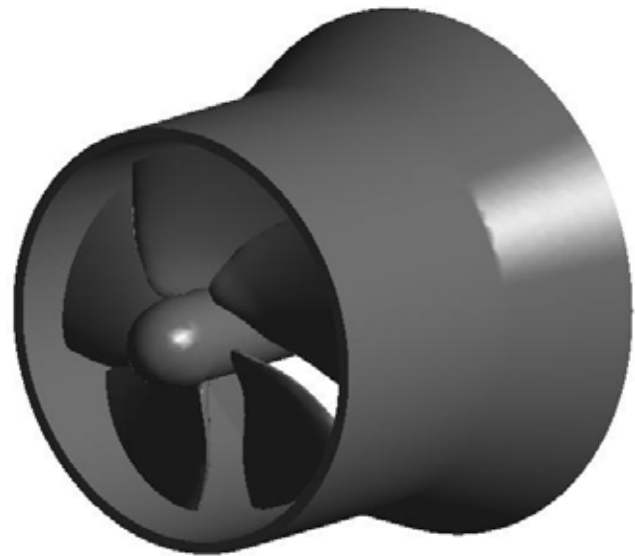
**(a) No shroud; no diffuser**



**(b) Shroud; no diffuser**



**(c) No shroud; with diffuser**



**(d) Shroud and diffuser**

**Figure 23 – Rotating reference frame models**

### **3.4.3 Results and discussion**

The power output of each model is shown in Figure 24. Both models with the rotor was enclosed by a cylindrical shroud, (b) and (c) from Figure 23, produced less power than the unshrouded model, (a). This appears to contradict the momentum source experiment,

where a diffuser was found to increase the power by a factor of 3.1. However, all geometries in the momentum source experiment enclosed the rotor with a cylindrical shroud. This is analogous to comparing models (b) and (c) in this experiment, which gives a power increase by a factor of 1.47. This result is not as dramatic as seen in the momentum source experiment. This may be due to inherent differences in the two turbine models. The momentum source model always extracts the same fraction of power from the flow. Therefore, its performance is uniform, regardless of the flow conditions. The ARRF, on the other hand, has a fixed geometry. The angle of attack on the rotor blades does not vary with the flow speed. Therefore the ARRF will have an optimum operating velocity, with performance losses on either side of this. In short, the momentum source does not take into account the performance curve of the rotor. A muted performance increase would therefore be expected in the ARRF experiment.

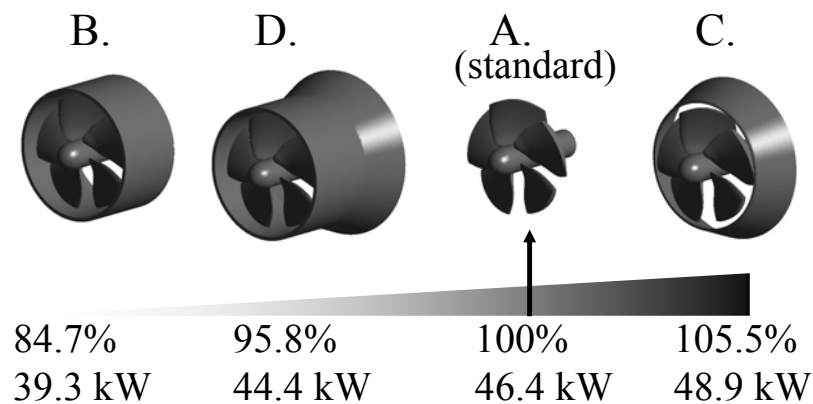


**Figure 24 – Power output comparison**

This experiment also shows that a cylindrical shroud is a source for significant power loss. Comparing the unshrouded rotor, (a) with the shrouded rotor with no diffuser, (b) reveals a power loss of over 15%. The importance of this power loss cannot be

understated. To gain insight into this effect, the streamlines are compared. Figure 25 shows the streamlines passing through the turbine for shrouded and unshrouded models. Inspection of the region near the tip of the blade reveals that the shroud interferes with the natural tendency for the fluid to expand as it is passing through the rotor.

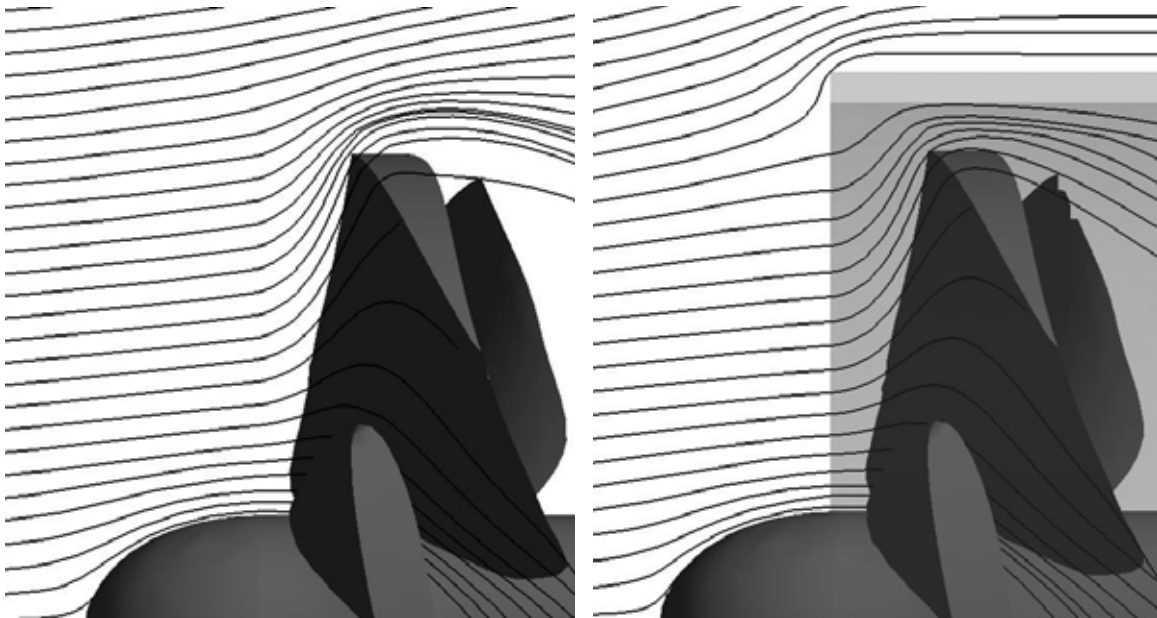
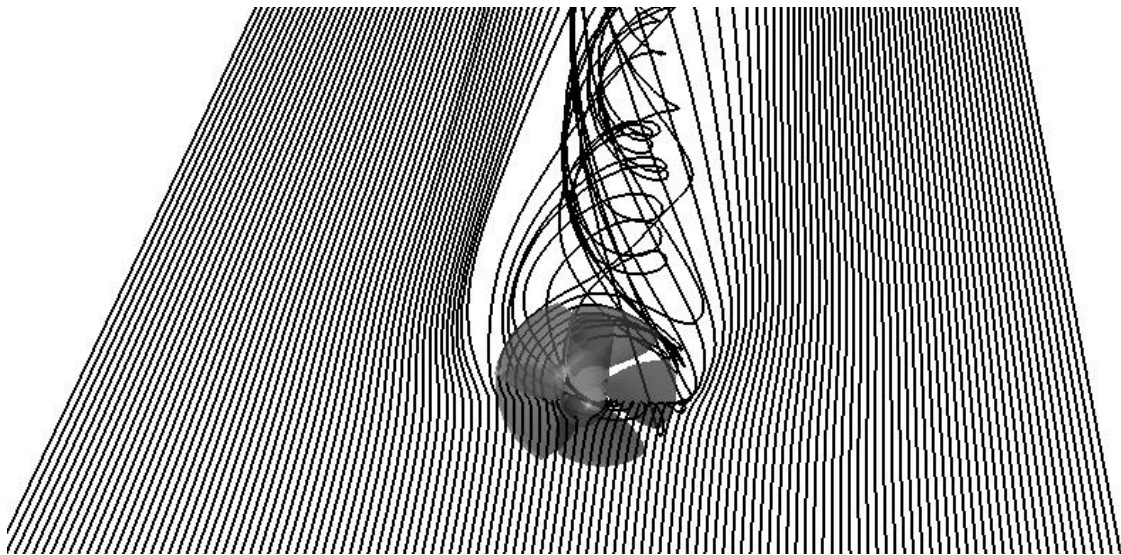


**Figure 25 – Streamlines across the turbine (a) with no shroud; (b) with a shroud**

A diffuser also causes the fluid to expand leading to theoretical performance increases; however in the experiment, the diffuser was placed further downstream of the rotor. It is likely to be far more beneficial to position the diffuser at the rotor such that its expansion regime coincides with that of the rotor, thus enhancing the expansion effect that is already present, instead creating a secondary fluid expansion downstream.

To test this idea, a model (c) in Figure 23 was developed. This diffuser was found to have a slight beneficial effect, providing a power increase of 5.5%. Therefore, according to these results, a diffuser is capable of increasing the power output of a turbine. The increase seen here is small, and would not likely offset the additional costs of the shroud. However, it should be noted that this diffuser shape was optimized in the momentum source experiment where a cylindrical shroud was present. It is unlikely that the same shape would be optimal with no cylindrical shroud. It is expected that a diffuser optimized for this configuration would produce a more substantial performance increase.

For a visual representation of these two designs, streamlines are plotted in Figure 16. The streamlines show a wider expansion behind the turbine when it is equipped with a diffuser.



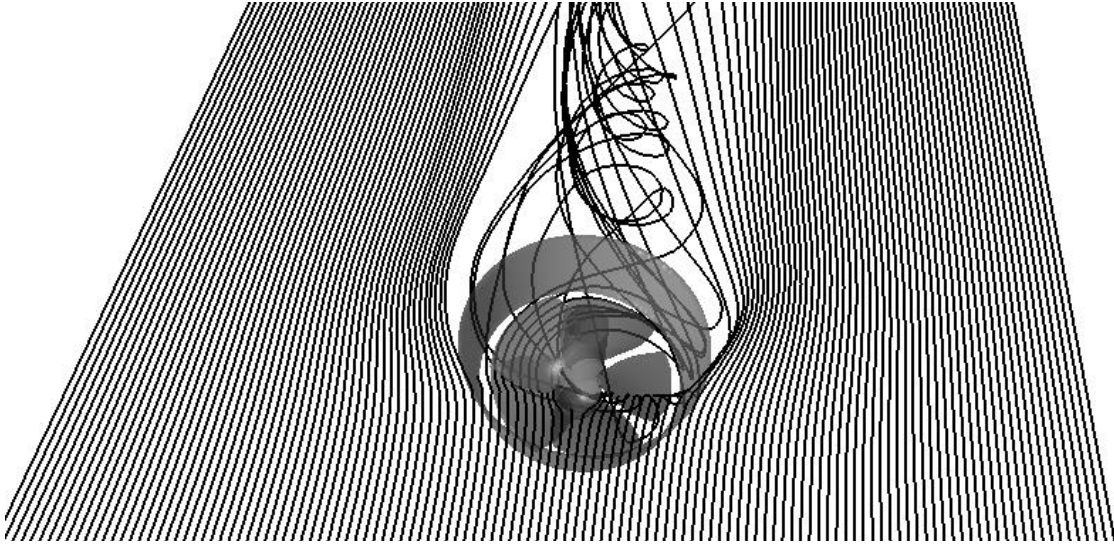


**Figure 26 – Streamlines across turbine (a) without diffuser, and (b) with diffuser**

The rotating reference frame model predicted a higher pressure drop than the momentum source model. Figure 27 shows the centre-line pressure for the averaging rotating reference frame (ARRF) model and the momentum source (MS) model. The ARRF model predicted a pressure drop of 7.38 kPa, whereas the MS model predicted a drop of 6.36 kPa. The pressure changes in the ARRF model took place over a larger distance than the MS model, an expected outcome as the MS model has a shorter streamwise turbine length.



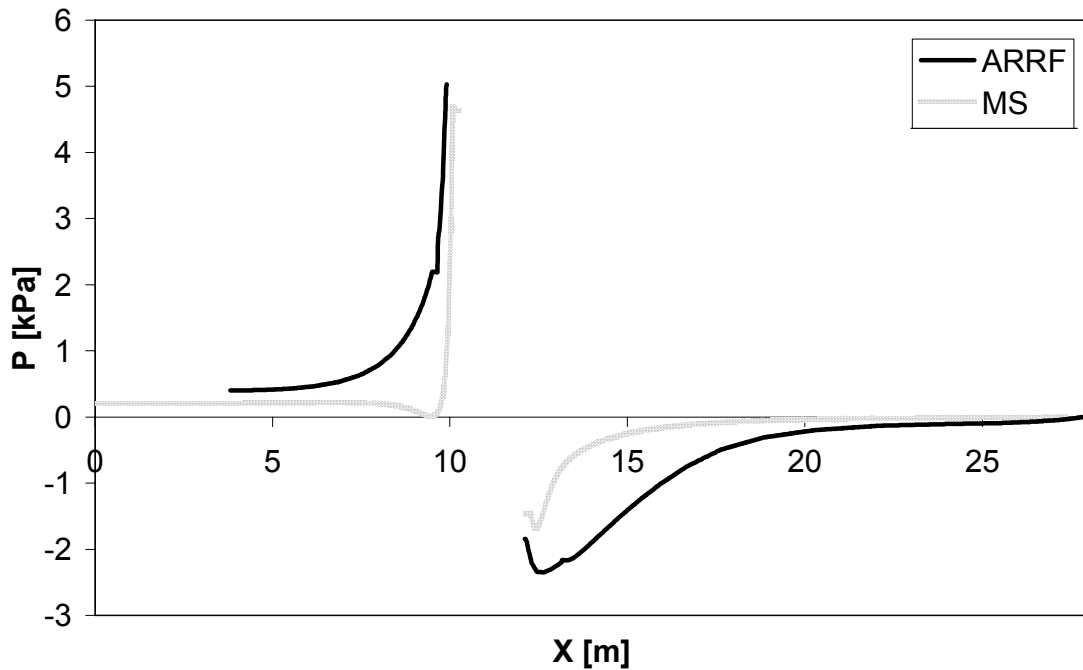


**Figure 27 – Centreline pressure for ARR and MS turbine models**

Further insight can be gained into the optimum geometry of the diffuser by studying the flow around the unshrouded turbine. The initial angle of the diffuser can be designed using the angle of the streamlines. In a similar manner to how the angles of the turbine cross sections were calculated (see Section 3.4.1), the diffuser can be treated as an airfoil section meeting the fluid at a specified angle of attack. Treating the diffuser as a cylindrical wing can give further insight into design possibilities, as wing design is well established. For instance, the use of upstream vortex generators and downstream slots can add energy to the boundary layer and increase the effect of the diffuser.

### **3.4.4 Cavitation**

Cavitation is an effect that causes wear on hydraulic turbo-machinery, leading to high maintenance costs and premature failure. Therefore it is important to understand whether

kinetic turbines are susceptible to this problem. A detailed study of cavitation is outside the scope of this thesis; however it is covered briefly here to provide recommendation for future studies. During cavitation, the fluid undergoes a momentary phase change into a gas, forming small vapour bubbles on the surface of turbine blades or impellers. As the vapour bubbles collapse, the returning fluid impacts the surface, causing wear (Brennen 1995). The phase change occurs when the fluid pressure drops below its vapour pressure, usually on the tips of rotating components.

The distribution of the relative pressure on the blade surfaces was calculated. A contour plot of this is shown in Figure 28.

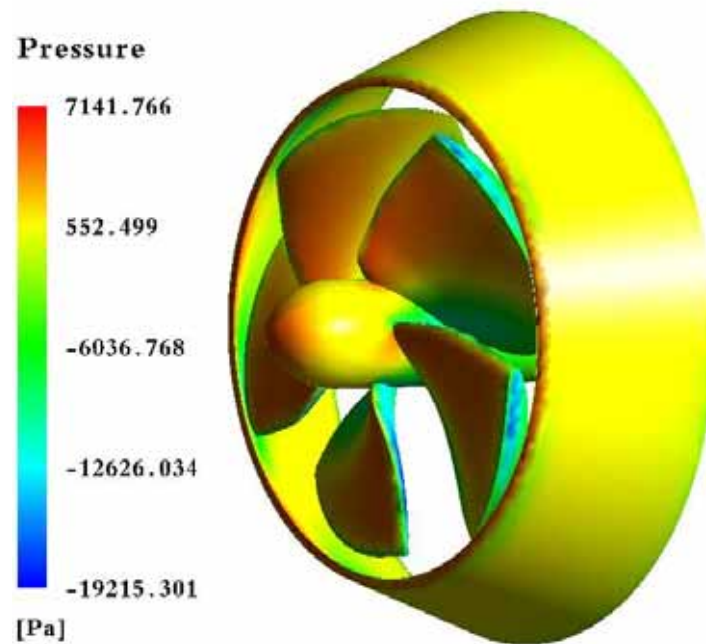


**Figure 28 – Surface pressure contour plot**

The low pressure areas are on the blade tips and the downstream side of the leading edge. The minimum relative pressure was found to be -19.22 kPa. The CFD reference pressure was taken to be 0 kPa at the outlet, therefore absolute pressure is given by:

$$P_{abs} = P_{rel} + P_{atm} + \rho g d . \quad (50)$$

The last term is depth pressure, where  $g$  is the acceleration due to gravity; and  $d$  is turbine depth. If we assume the turbine is very close to the surface (i.e. no depth pressure), the absolute pressure is 82.08 kPa. This is well above the vapour pressure of water, which is 2.49 kPa at 20° C. As the depth of the turbine increases, its absolute pressure also increases, therefore, according to this preliminary calculation, cavitation is not a concern. Further study is necessary to confirm this.

## **4 Boundary layer power loss mitigation**

One source of power loss is the boundary layer of the river. If the kinetic turbine is too deep within the boundary layer, it will only be able to produce a fraction of the potential power at that site. However, it may be possible to mitigate this power loss by altering the geometry of the anchor, a component used to secure the kinetic turbine to the riverbed.

### **4.1 Anchor geometry methodology**

The boundary layer of a river is a region where the flow velocity is less than the freestream. Since power density is a function of velocity, any reduction in the mean velocity translates into power loss. The anchor, a component of the kinetic turbine technology, is already within the boundary layer upstream. The question is: can the geometry of the anchor be altered to influence the riverbed boundary layer such that a downstream turbine will see a beneficial effect? The parameters of this experiment are shown in Table 6.



$F_c$  is the load on the cable;

$V$  is the volume of the anchor;

$\rho_a$  is the density of the anchor;

$\rho_f$  is the density of the fluid;

$g$  is gravity;

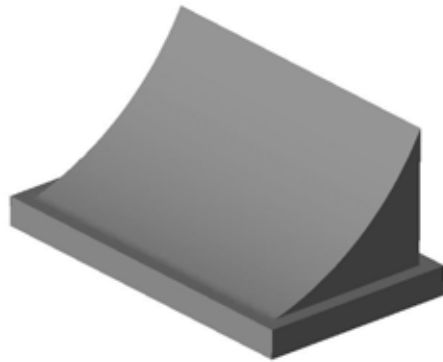
$\mu_s$  is the static coefficient of friction between the anchor and the riverbed; and

$F_d$  is the drag force on the anchor.

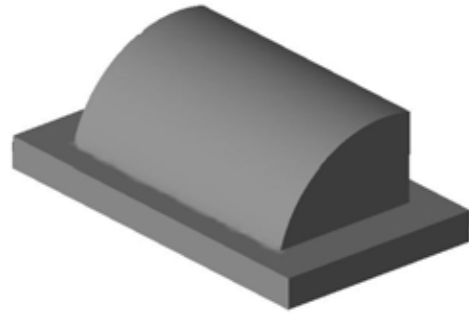
To simplify the problem, the drag force on the anchor is ignored, and it is assumed that the maximum force of the cable is a design limitation. Therefore, the volume of the anchor was chosen to be a constant.

#### **4.1.2 Anchor design**

The shapes of the anchors were designed qualitatively, as a broad overview of the effects of different techniques. Anchors A and B are shown in Figure 29, and anchors C and D are shown in Figure 30.

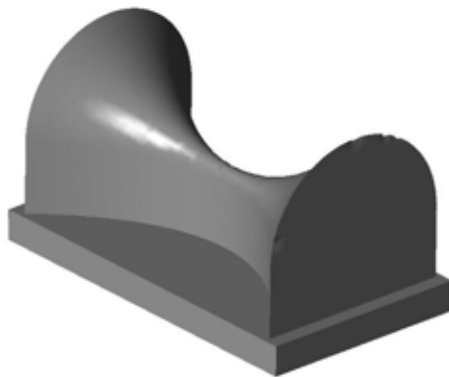


**ANCHOR A**

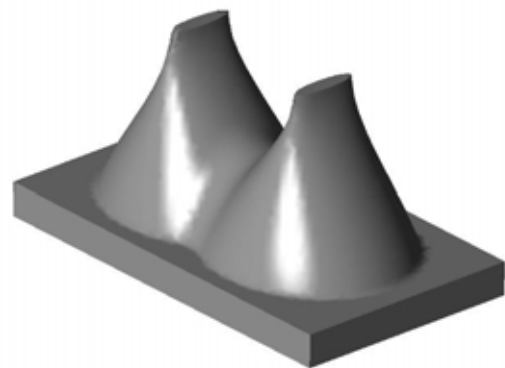


**ANCHOR B**

**Figure 29 – Anchor A and anchor B isometric view**



**ANCHOR C**



**ANCHOR D**

**Figure 30 – Anchor C and anchor D isometric view**

Anchor A was designed with the aim of maximizing its interference with the boundary layer. It is the tallest of the anchors, and produces the largest vertical velocities. Anchor B was based on the function of a contraction cone in a wind tunnel. Anchors C and D were designed with the goal of producing a wake flow with a high velocity central core, similar to a jet. All anchor designs can also be used to shelter the turbine from debris, especially during spring runoff.

### 4.1.3 Mesh strategy

A hybrid mesh was used for all four simulations. A hexahedral mesh has the advantage of using fewer elements than a tetrahedral mesh. Eight nodes require only one hexahedral element, where six tetrahedrons are required. However, tetrahedrons can mesh any complex geometry quickly, whereas some geometries are difficult to mesh with hexahedrons. A hybrid mesh can use hexahedrons for the bulk of the fluid, and tetrahedrons around the complex curves of the model, thus taking advantage of both types of meshing.

The freestream fluid was modelled using a hexahedral mesh with a rectangular volume omitted. The rectangular volume was large enough to encompass all anchor designs, thus enabling it to be reused for all simulations. The anchors were meshed using a tetrahedral structure. A smoothing algorithm was used on the tetrahedral meshes to ensure high quality. Grid independence and convergence independence were not tested. The mesh sizes are shown in Table 7.

**Table 7 – Anchor mesh sizes**

| <b>Anchor</b> | <b>Hexahedral Mesh</b> | <b>Tetrahedral Mesh</b> | <b>Total Elements</b> |
|---------------|------------------------|-------------------------|-----------------------|
| <b>A</b>      | 103712                 | 94963                   | 198675                |
| <b>B</b>      | 103712                 | 83481                   | 187193                |
| <b>C</b>      | 103712                 | 125798                  | 229510                |
| <b>D</b>      | 103712                 | 86158                   | 189870                |



#### 4.1.4 Fully-developed boundary layer

The fully-developed inlet conditions for the anchor simulations were developed using a standard  $k-\varepsilon$  turbulence model. A 12 x 12 meter river cross-section was numerically simulated. The sides and top surface had symmetry boundary conditions; whereas the bottom surface was a rough wall with a roughness height of 0.3 meters. After a distance of 1,460 meters, the boundary layer stabilized with a thickness of 9 meters. This flow profile was used as an inlet velocity profile for the anchor simulations.

#### 4.2 Results and discussions

The fully developed profile is used as a basis of comparison. The power of the fluid passing through a 1 meter circular area calculated at various heights above the riverbed is shown in Figure 31.

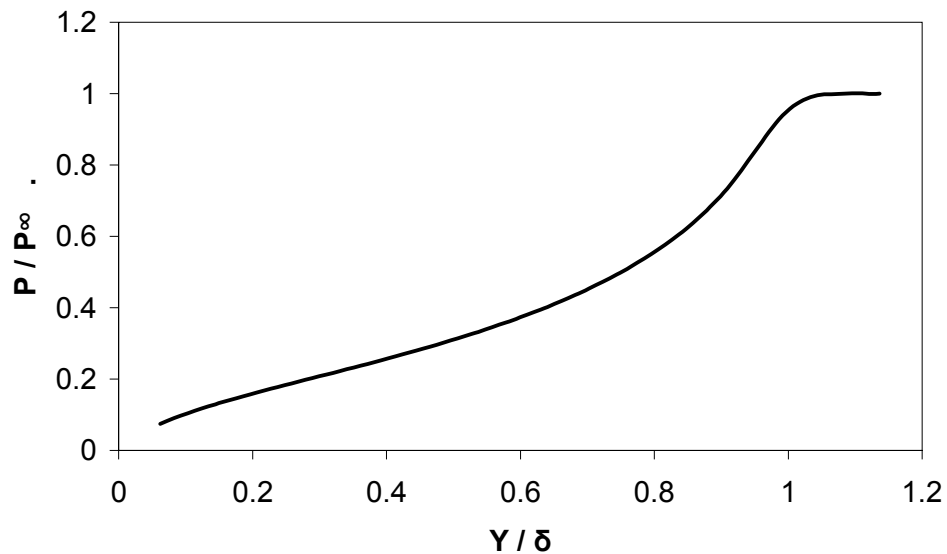


**Figure 31 – Boundary-layer power loss**

The results show that if the turbine is resting on the surface of the riverbed it would see less than 10% of the power in the freestream. In addition, this flow variation across the

turbine may affect the turbine efficiency because the asymmetric pressure distribution leads to off-axis loading on the bearings.

In a similar manner, the power profiles were calculated for the anchor simulations. The power profiles were taken at a distance of 2.5 meters, 7.5 meters, and 12.5 meters downstream from the trailing edge of the anchor. At a distance of 2.5 m from the anchor trailing edge, the power passing through a one meter diameter turbine is shown in Figure 32. The curves have a jagged appearance, an effect caused by truncation in the numerical power calculations.

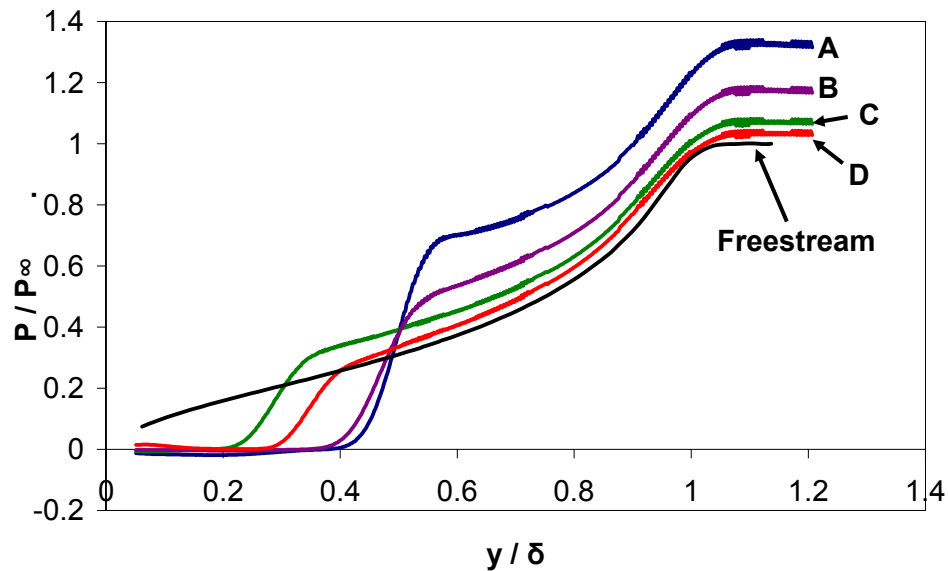


**Figure 32 – Power ratio versus  $Y^*$  at 2.5 meters from the anchor**

At a distance of 7.5 meters, the power passing through a 1 meter turbine is shown in Figure 33; Figure 34 shows the results at a distance of 12.5 meters.

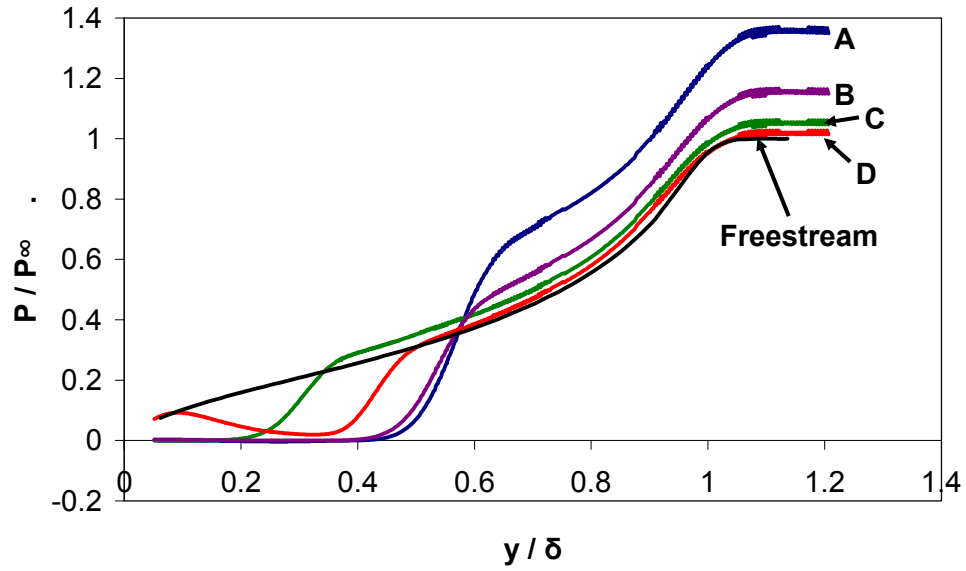


**Figure 33 – Power ratio versus  $Y^*$  at 7.5 meters**

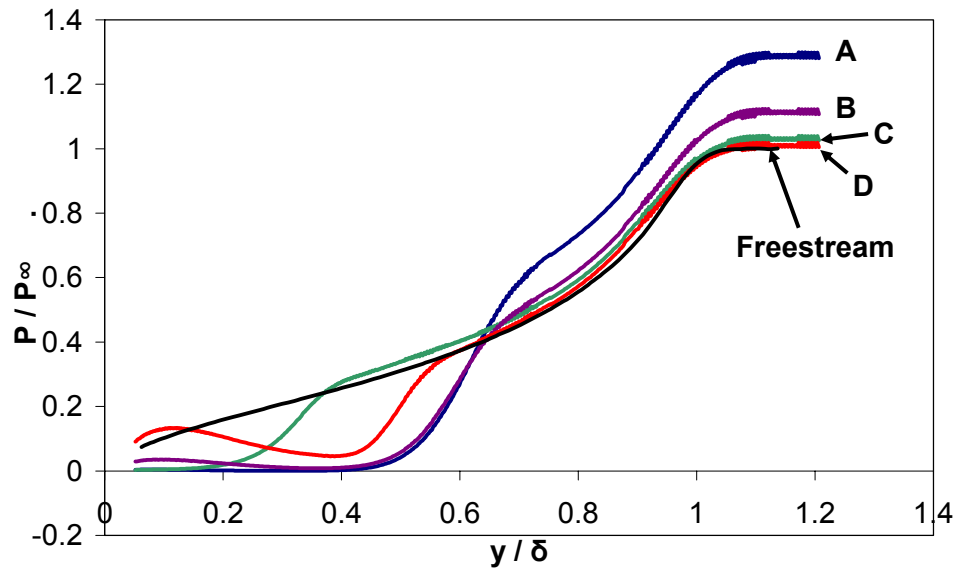


**Figure 34 – Power ratio versus  $Y^*$  at 12.5 meters**

For a visual representation of the flow, a series of streamlines is plotted at an initial height of 1.5 meters above the riverbed. These are shown in Figure 35. Mid-stream velocity contour plots are shown in Figure 36.

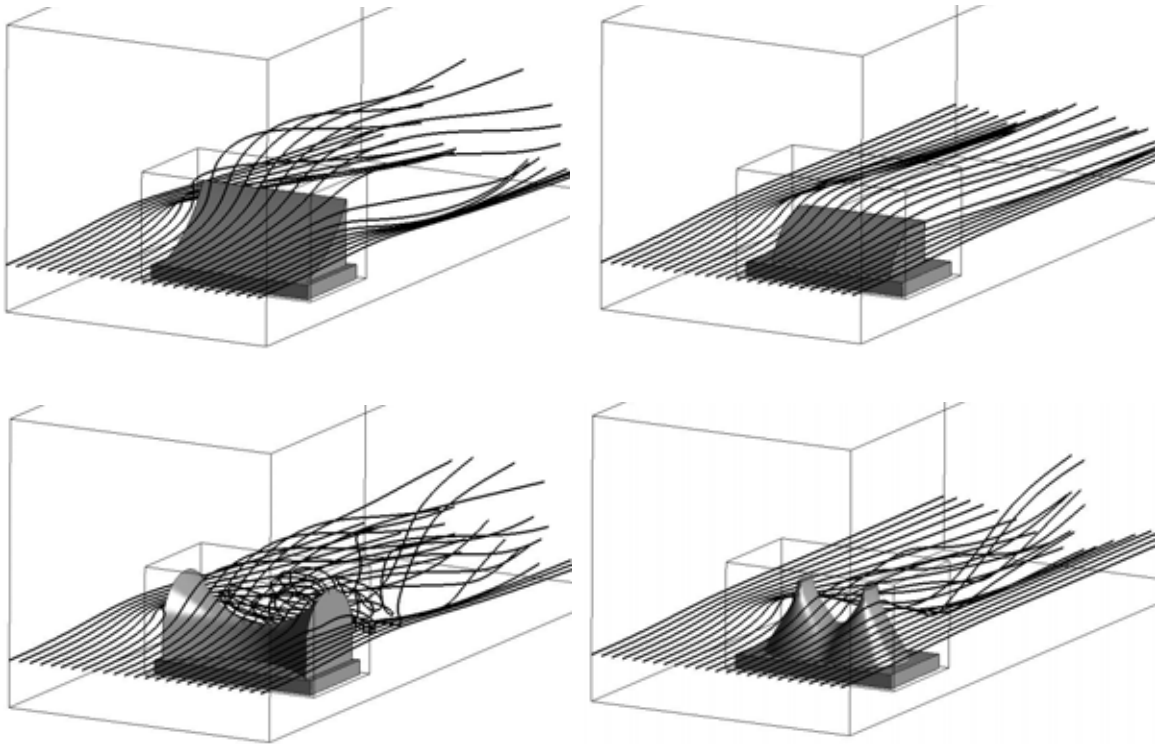


Figure 35 – Streamlines around each anchor

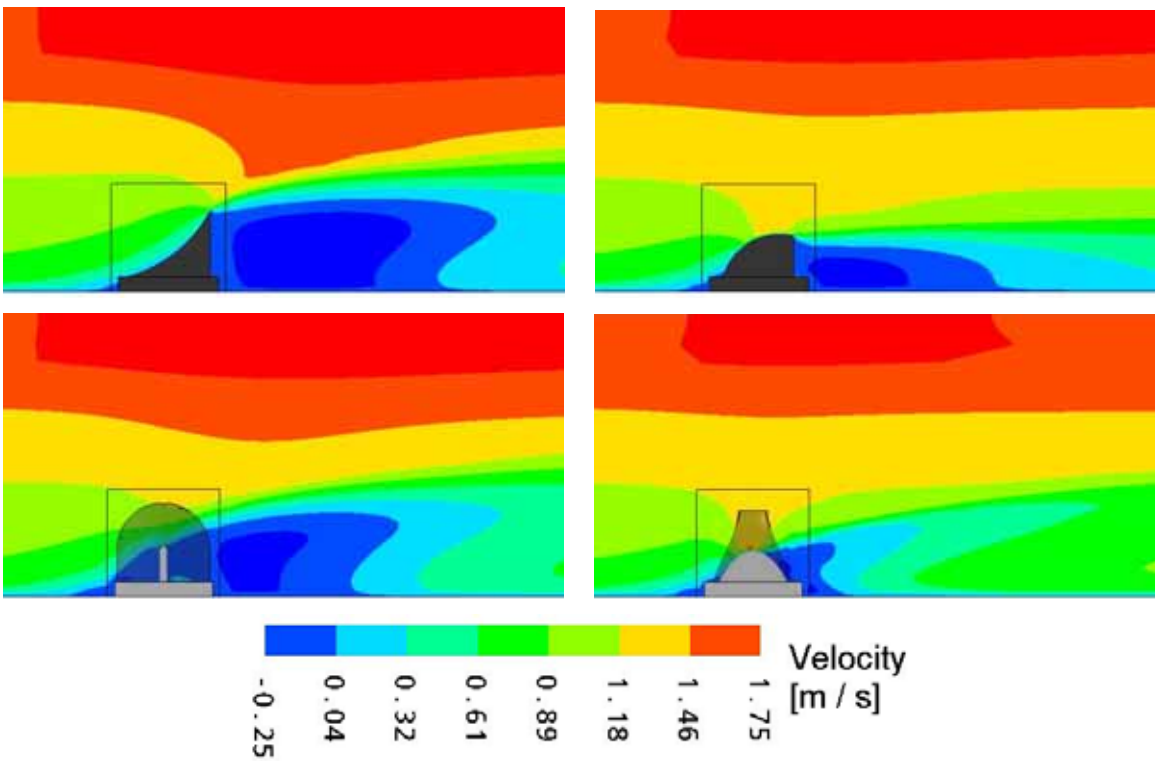


Figure 36 – Mid-stream velocity magnitude contour plot

From these results, it is apparent that the power available in the flow can be increased by modifying the geometry of an upstream anchor block. The strength and distance of this effect is significant, with a power increase by a factor of 1.33 at a distance of 12.5 meters. The obvious high performing anchor shapes are A and B, shapes designed to interfere with the boundary flow; as opposed to C and D, shapes intended to create wake with flow structures similar to jets. The controlled variable was anchor volume, intended to simulate the benefit against practical design limitations like concrete use; however this may have obscured the fundamentals of the problem. The best performing anchor, A, was also the tallest. It is likely that the downstream power boost is a factor of cross stream area. Furthermore, it should be noted that the benefits from these anchor shapes only occur in the upper half of the river depth. If the turbine is to be situated well below the surface of the water, the positive effect of these anchor designs would be their protection against debris, as the power would be significantly reduced.

## **5 Particle Image Velocimetry (PIV) experiment**

In this chapter, PIV is introduced as a method to validate some of the numerical results obtained for the simulation of the diffuser in Chapter 6.

### **5.1 PIV overview**

Particle Image Velocimetry (PIV) is an instantaneous, two dimensional, non-invasive flow-mapping technique. A PIV system consists of five main components, as shown in Figure 37:

- a high intensity light source and optics;
- a camera or other recording device;
- a data acquisition system;
- a fluid with embedded seeding particles; and
- a computer with appropriate software.

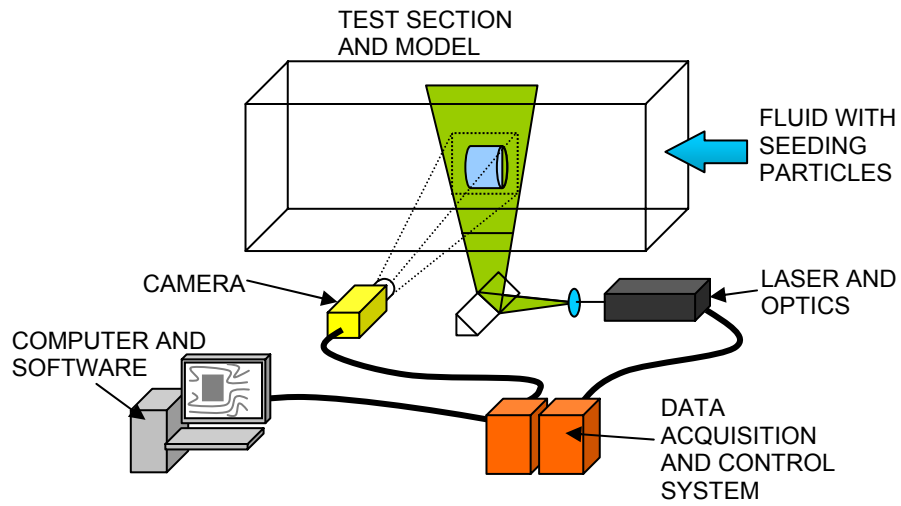


**Figure 37 – PIV apparatus overview**

The fluid is illuminated by a plane of intense light, and a camera or other recording device captures an image of the flow. The fluid is typically seeded with reflective particles, although some multi-phase mixtures do not need seeding at all. When two images are captured in quick succession, the fluid velocities can be inferred from the displacement of the particles, as shown in Figure 38.

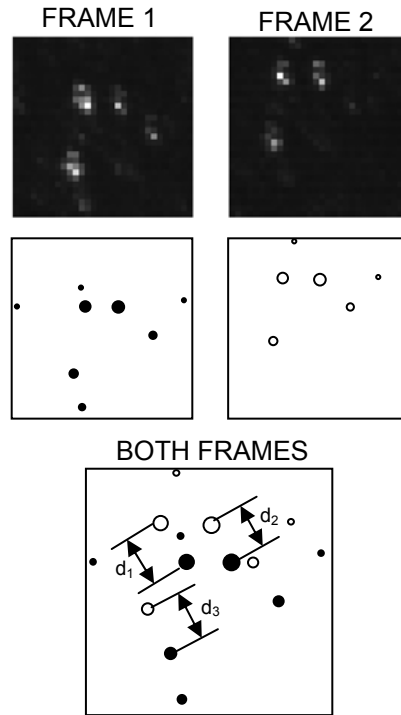


**Figure 38 – PIV displacement comparison**

The velocity at this location can be calculated from:

$$U = \frac{d}{\Delta t}, \quad (52)$$

where  $d$  is the distance the particle moved between the two images, and  $\Delta t$  is the time lapse.

## 5.2 PIV theory

There are some practical limitations to tracking individual particles. Sometimes a particle will not be within the plane of light in the first or second frame, and will therefore be missing. Or there may be multiple particles in close proximity, and it is difficult to determine their motion, as shown in Figure 39.



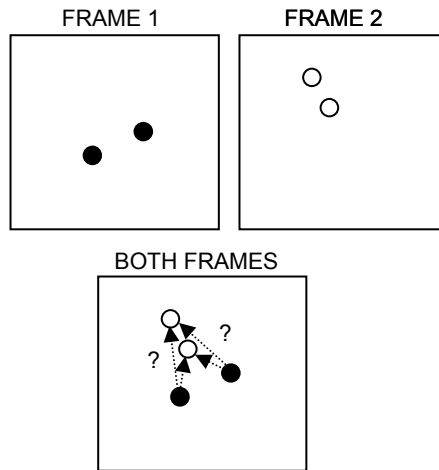


**Figure 39 – Particle tracking problems**

Rather than track individual particles, the PIV software divides the images into an array of interrogation regions. An interrogation region is a small rectangular subset of the original image, as shown in Figure 40.

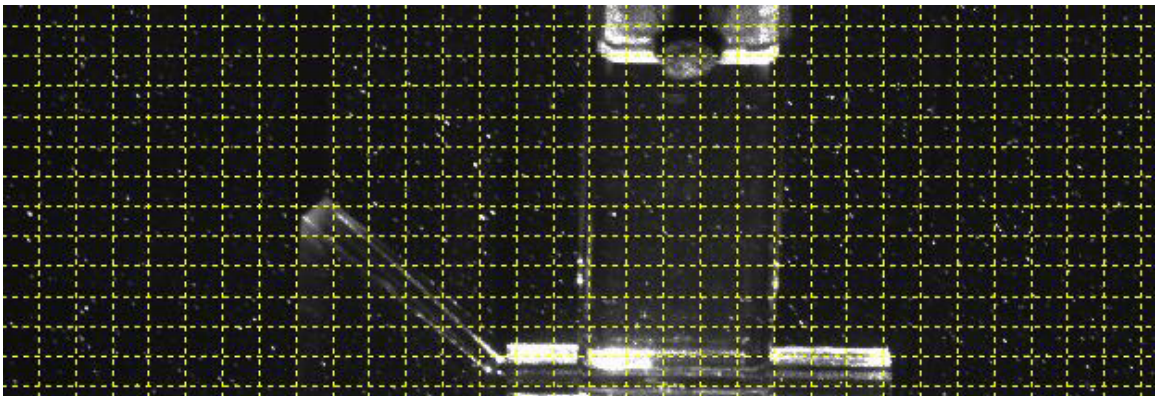


**Figure 40 – Interrogation regions**

Each interrogation region represents two datasets:  $f(k,l)$ , and  $g(k,l)$ , pixel intensity arrays of the first and second images respectively. The goal of the calculation process is to

determine the average displacement of the particles within an interrogation region. This is achieved by finding a displacement,  $m$  and  $n$  that gives the best cross-correlation between the two images. The cross-correlation is calculated for a range of  $m$  and  $n$ :

$$\phi_{fg}(m, n) = \sum_{k=-\infty}^{\infty} \sum_{l=-\infty}^{\infty} f(k, l) \bullet g(k + m, l + n) \quad (53)$$

Normally, cross-correlation is calculated with a denominator to produce a unit-less quantity between zero and one, but since we are only concerned with relative values, the denominator is unnecessary. The function  $\phi_{fg}(m, n)$  describes a surface called the correlation plane. When a particle in  $f$  matches up with its own image in  $g$ , there will be a large spike in the correlation plane. When it matches up with another particle, there will be a small spike in the correlation plane. Once the optimum values for  $m$  and  $n$  are calculated, these are converted into  $u$  and  $v$  velocities.

To speed up the calculation process, the software uses a fast-Fourier-transform (FFT) on  $f$  and  $g$ , which eliminates the need for the summation in (53):

$$\Phi_{FG}(u, v) = F(u, v) \bullet G(u, v), \quad (54)$$

where  $\Phi$ ,  $F$  and  $G$  are the FFT of  $\phi$ ,  $f$  and  $g$  respectively. Once  $\Phi$  is calculated, the inverse FFT is calculated, and the velocities are derived.

The use of a FFT algorithm also introduces a source of error. An FFT function is fundamentally continuous and cyclic in nature; therefore the correlation plane will have errors near the edges of the interrogation region. A series of window functions are

available to bias the correlation calculation towards the centre of the interrogation region (Dantec 2000).

### **5.3 Apparatus**

The experiment was performed using a water tunnel with a 1.8 m long test section and a cross section of 0.6 m x 0.6 m. The water was embedded with polyamide seeding particles with a mean diameter of 20 microns. The fluid was illuminated with a New Wave Gemini double pulsed Nd:YAG laser, frequency doubled to emit light at a wavelength of 532 nm. A Kodak Megaplug ES1.0 CCD camera was used to record images with a resolution of 1008 x 1016 pixels. Figure 41 shows the experimental apparatus.

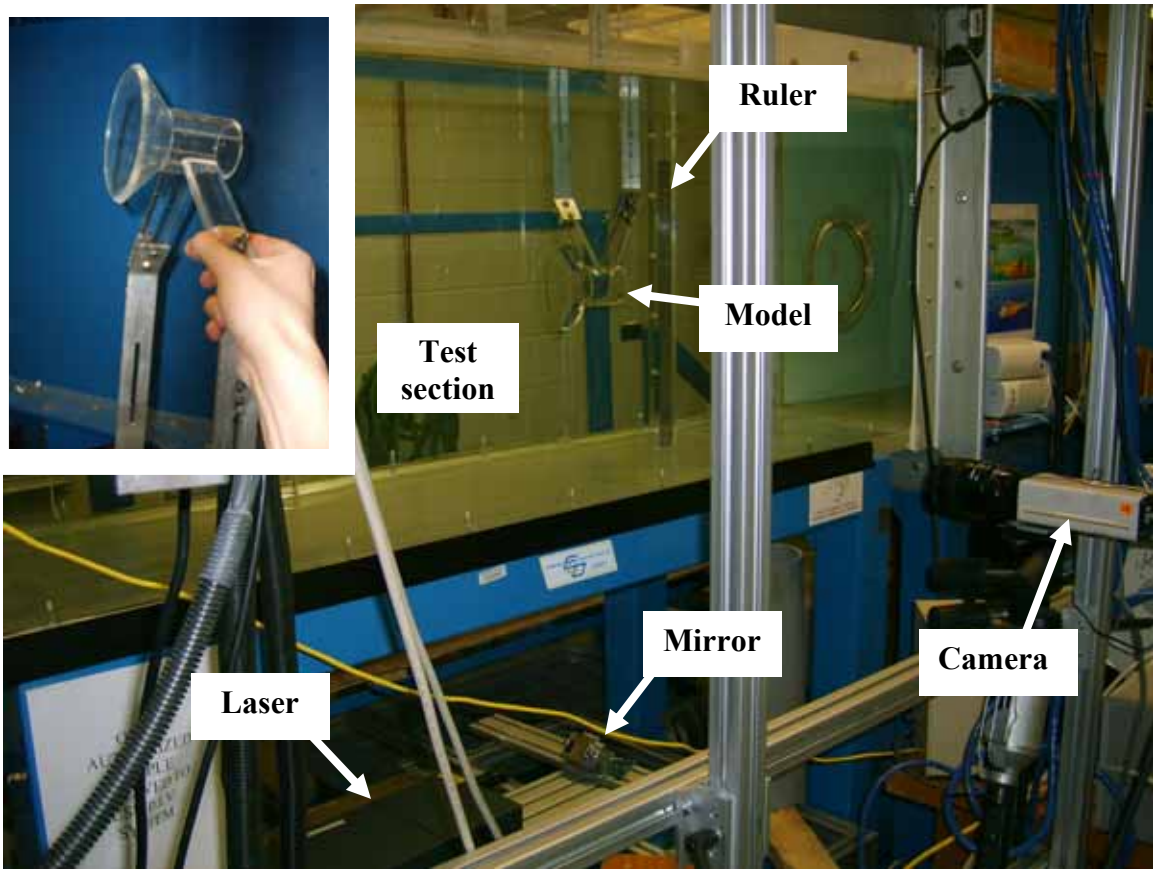


**Figure 41 – Experimental apparatus**

The PIV is an optical measurement system; therefore a transparent construction material is necessary for the model if interior flow is to be visualized. An acrylic material was selected. It was machined to the dimensions shown in Figure 42, and polished until transparency was achieved.

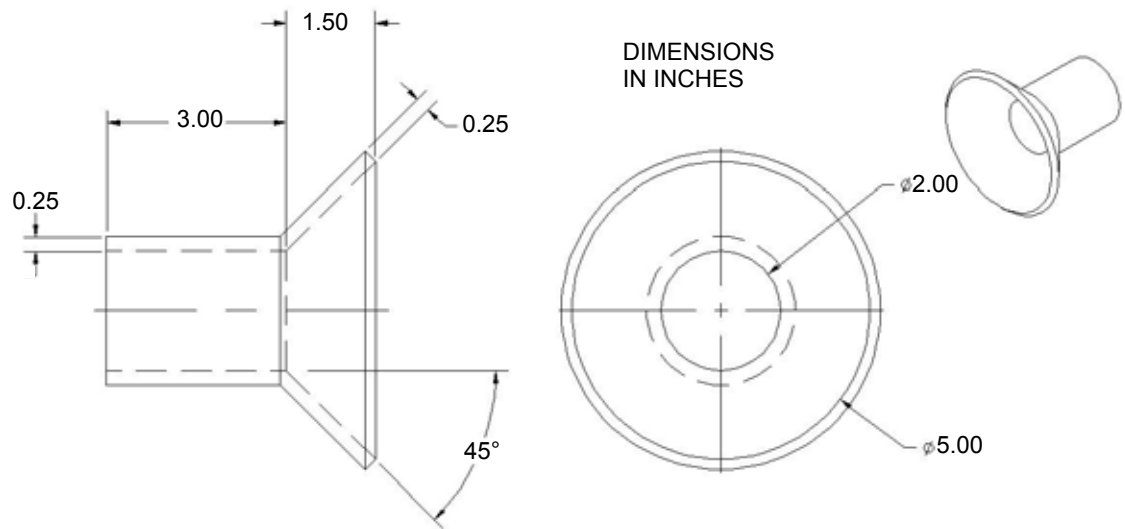


**Figure 42 – Acrylic model dimensions**

The model needed to be secured against strong drag forces from the water; however, the walls of the water tunnel are smooth. The only means to secure the model was from above. Therefore, it was mounted to two transparent brackets which were secured to an aluminium frame. The frame was secured at the top of the water tunnel test section.

## 5.4 Procedure

The set-up and experimentation are detailed below.

### 5.4.1 Set-up

The test section was illuminated by the laser from below, through its transparent base. The laser was aligned with the cylindrical axis of the model, thus producing an image of the flow along the geometric symmetry plane. The alignment was achieved by eye, using reference marks measured on the model and support structure. The camera was set on a tripod and aligned by reference to cues in the image it produced. Focus and scale were achieved by securing a ruler within the light plane, and focusing on the ruler under

normal lighting conditions. Any time the model or camera was moved, this process was repeated.

The timing between laser pulses and the settings for the auto-correlation calculation process were adjusted by trial and error. The model was oriented as a diffuser, and the water tunnel was operated at its maximum speed. The time interval was adjusted, and for each setting, twenty images were captured. Time intervals tested were:

- 1  $\mu\text{s}$ ;
- 100  $\mu\text{s}$ ;
- 250  $\mu\text{s}$ ; and
- 800  $\mu\text{s}$ .

For each dataset, a series of cross-correlation calculations were performed. It was found that the data was interspersed with some outliers. A range validation was used to identify some of the obvious outliers. That is, if the velocities were outside a set range, they were marked as *rejected*. The same range validation was applied to all datasets, and the time interval that produced the least amount of rejected vectors was found to be 250  $\mu\text{s}$ .

The settings for the cross-correlation processing were selected in a similar manner. A dataset of twenty paired images were captured using the 250  $\mu\text{s}$  time interval. These were processed using various software settings, and the averaged vector maps were compared. Interrogation regions were chosen to be 32 x 32 pixels with a 50% overlap.

No image filters or window functions were found to be beneficial. A moving average validation was chosen to identify outliers, and replace them with substitute vectors.

### **5.4.2 Experimentation**

There were two variables under investigation: model orientation (nozzle or diffuser); and flow speed, set according to the frequency of the water tunnel pump. This gave a total of six datasets.

- D60 – Diffuser-configured model with the pump set to 60 Hz;
- D45 – Diffuser-configured model with the pump set to 45 Hz;
- D30 – Diffuser-configured model with the pump set to 30 Hz;
- N60 – Nozzle-configured model with the pump set to 60 Hz;
- N45 – Nozzle-configured model with the pump set to 45 Hz; and
- N30 – Nozzle-configured model with the pump set to 30 Hz.

Although more detailed studies on the inlet conditions will be presented in Section 6.3, the pump frequencies approximately corresponded to free stream velocities as shown below.

- 60 Hz was approximately 1 m/s;
- 45 Hz was approximately 0.8 m/s; and
- 30 Hz was approximately 0.5 m/s.

For each configuration, one thousand paired images were taken over a period of eight minutes. This resulted in six thousand paired images as an experimental data set.

## **5.5 Data processing**

To process the data, a method for dealing with reflections and other noise needed to be developed. Once this method was established, an adaptive-correlation algorithm was employed, and the vector maps were averaged.

### **5.5.1 Refraction correction**

Due to differences in the indices of refraction, there is distortion in the images recorded by the PIV system. As can be seen in Figure 43, there are apparent reflections in the top and bottom third of the cylinder, obscuring the particles.

It was postulated that this noise was due to total internal reflection, and an image correction algorithm was sought. Refractive effects proved to be insignificant, and the noise remained obscuring the inner cylinder walls, a region of interest. The calculations for the refractive effects, and the correction algorithm are detailed in Appendix B. The algorithm was applied to one of the images from the PIV experiment. Before and after images are shown in Figure 44.



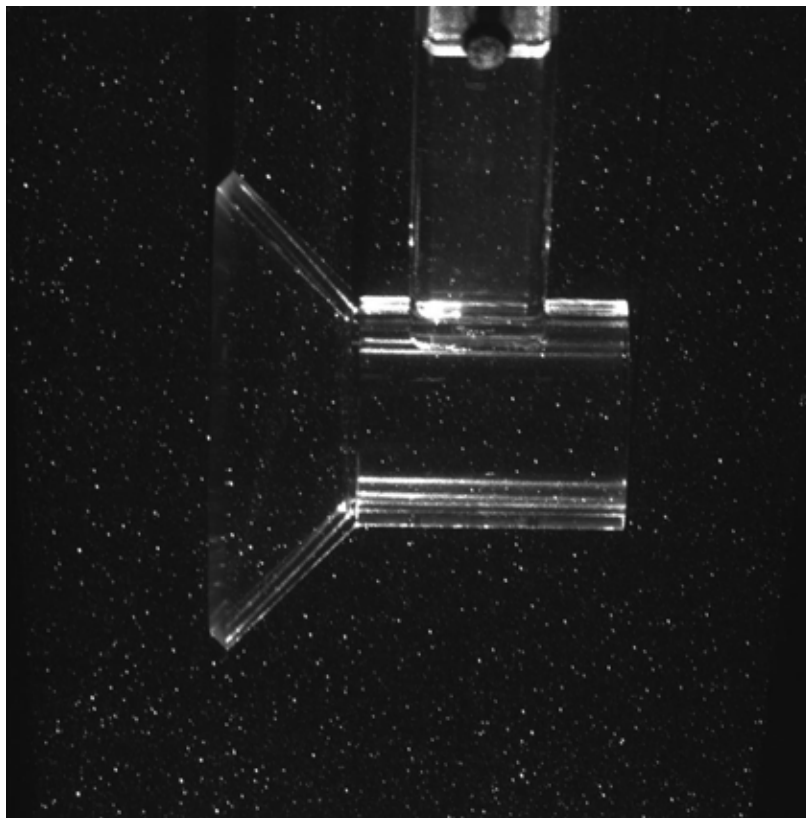


**Figure 43 – Sample PIV raw image**

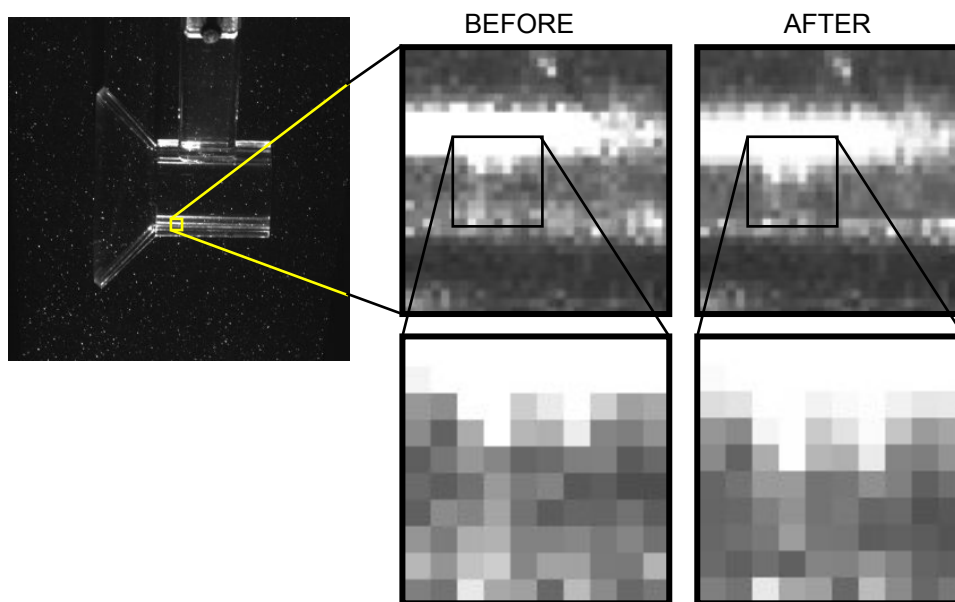


**Figure 44 – Refraction correction, before and after**

Note how minimal the distortion is. Regions in which the distortion is greater than half a pixel are highlighted in Figure 45, with a maximum distortion of 2.14 pixels.

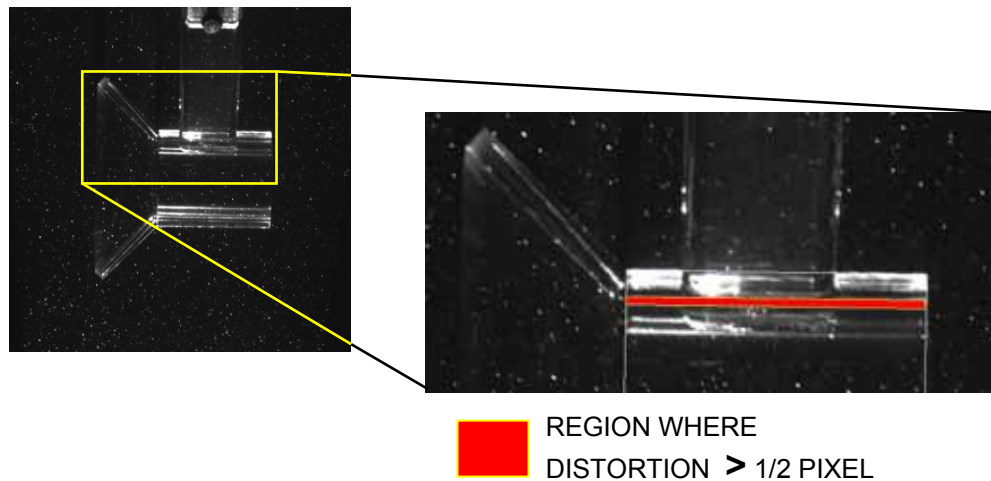


**Figure 45 – Half-pixel distortion region**

Interrogation areas in the PIV system were 32 pixels by 32 pixels. Therefore this distortion was determined to be insignificant. An alternate technique to deal with the noise was necessary.

### **5.5.2 Masking and value blanking**

A digital mask was manually created from one image of each experimental run. The masks block off regions of obvious reflections or obstructions, as shown in Figure 46 below.

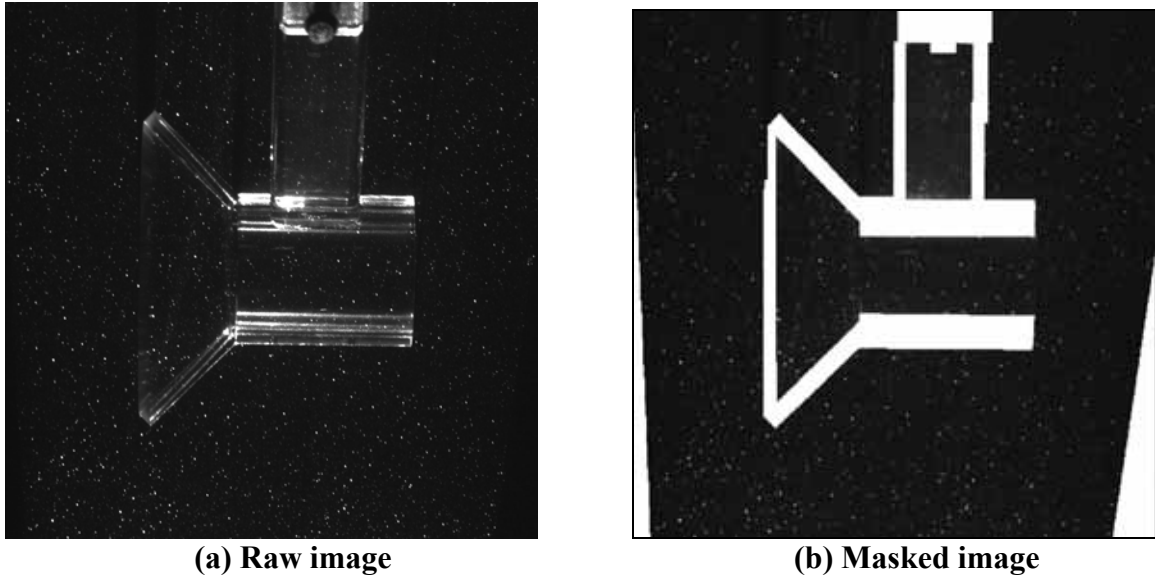


**Figure 46 – Typical image mask**

Masks can be used in two ways. The raw image can be masked prior to any data processing. This way, the cross-correlation algorithm will never see any noise at all. Alternately, the mask can be applied to the vector map, marking any vectors within the masked region as *rejected*. Both processing techniques were applied to the data sets, and compared. The vectors produced from a masked image suffered from obvious signal drop-off near the mask edge, thus producing unrealistic velocities near the model. Those produced from the raw image were qualitatively superior; therefore this latter dataset was selected for further analysis.

After the data were processed and plotted, it was apparent that some optical effects were still producing bias. For example, the seam line at the diffuser and the shadows above the model tended to increase the  $u'$ , as seen in Figure 47.

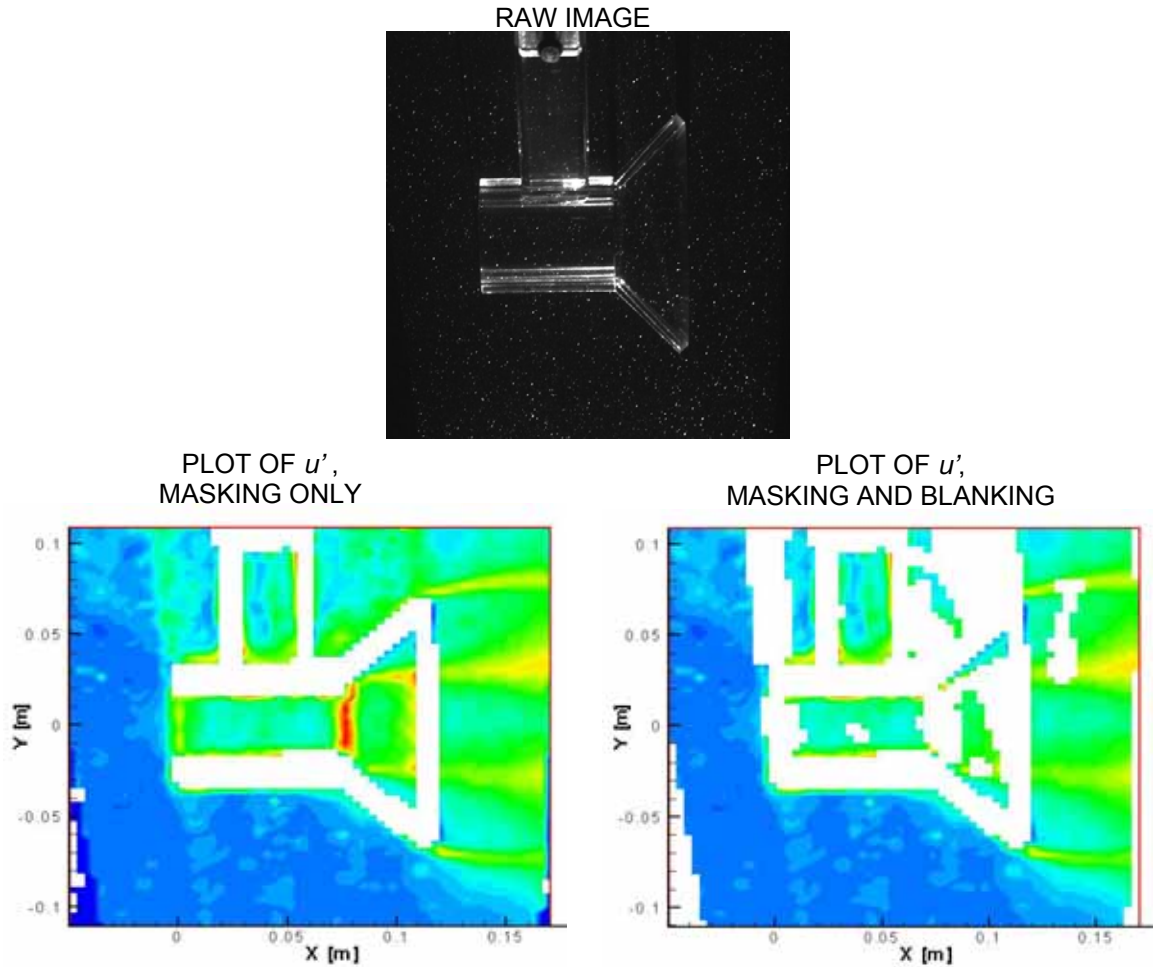


**Figure 47 – Value blanking**

To handle this problem, nodes that had less than 90% validity were blanked. That is, if more than 10% of the vectors at that location were marked as “rejected”, the node was omitted in its entirety. This value blanking was employed for all calculations.

### 5.5.3 Adaptive-correlation and averaging

To process the data, an adaptive-correlation algorithm was used. Adaptive-correlation is the combination of cross-correlation and validation. Interrogation regions of 32 x 32 pixels were used with an overlap of 50%. The overlap was used due to errors inherent at the edges of interrogation regions. No window functions or image filters were used. A

moving average validation was used to identify and substitute vector outliers. Once all the paired images were processed, the vector maps were statistically averaged, producing:

- the mean  $x$  and  $y$  velocity components;
- the standard deviation for each velocity components;
- the correlation coefficient; and
- the number of valid vectors.

The substituted vectors from the moving average validation were not included in the statistical calculations.

#### 5.5.4 Derived quantities

Further quantities can be derived from the data. The standard deviation of the velocity is actually the root-mean-square of the fluctuating component.

$$\sigma_u = \sqrt{\frac{1}{N} \sum_{i=1}^N (\bar{U} - U_i)^2}, \quad (55)$$

where  $\bar{U}$  is mean velocity and  $U$  is instantaneous velocity. But since

$$\bar{U} - U = u, \quad (56)$$

where  $u$  is the fluctuating component, then (55) is the root-mean-square of  $u$ . This gives  $u'$ :

$$u' = \sigma_u = \sqrt{\frac{1}{N} \sum_{i=1}^N (u_i)^2}. \quad (57)$$

Therefore, we have  $u'$  and  $v'$ , but not  $w'$ . The dataset is only two-dimensional; therefore the  $z$  direction is missing. To produce turbulence quantities, an assumption needs to be

made for  $w'$ . It seems tempting to choose  $w' = v'$ , but experimentation shows that for developing flows,  $w'$  usually falls between  $u'$  and  $v'$  (Davidson 2004, p. 135). Therefore, we will assume that  $w'$  is the average of  $u'$  and  $v'$ :

$$w' = \frac{1}{2}(u' + v') \quad (58)$$

The correlation coefficient can be used to derive  $-uv$  Reynolds shear stress:

$$-uv = -Ru'v', \quad (59)$$

where  $R$  is the correlation-coefficient. Turbulence kinetic energy,  $k$ , can be calculated:

$$k = \frac{1}{2}(u'^2 + v'^2 + w'^2). \quad (60)$$

Turbulence intensity,  $I$ , is given by

$$I = \frac{U'}{\bar{U}}, \quad (61)$$

where  $U'$  is the total fluctuating root mean square (RMS) velocity, defined by:

$$U' = \sqrt{\frac{1}{3}(u'^2 + v'^2 + w'^2)}, \quad (62)$$

and  $\bar{U}$  is the total velocity magnitude, defined by:

$$\bar{U} = \sqrt{\bar{U}^2 + \bar{V}^2 + \bar{W}^2}. \quad (63)$$

The two dimensional nature of the PIV data also requires us to assume a value for  $\overline{W}$ .

For the purpose of these analyses,  $\overline{W}$  was assumed to be equal to  $\overline{V}$ <sup>26</sup>.

## 5.6 Error analysis

It is important to understand the quality of the experimental data before it is analysed. A Monte Carlo simulation is used to check for consistency, and the experimental conditions are studied in more detail.

### 5.6.1 Monte Carlo simulation

A useful tool to gain insight into the quality of PIV data is a Monte Carlo simulation (Keane et al. 1992). Monte Carlo simulations comparing subsets of a large data set have been used in previous studies to establish uncertainty (Oerlemans 2005). The D60 dataset was chosen for analysis. From the thousand available vector maps, two data subsets of equal size were randomly selected, with no duplications permitted. Rejected vectors were removed, and statistical data was calculated for each dataset:

- The mean velocities,  $\overline{U}$  and  $\overline{V}$  ;
- The standard deviations of the velocities,  $u'$  and  $v'$ ; and
- The correlation coefficient between the velocities,  $R$ .

The two datasets were compared against one another and the differences were calculated using root-mean-square error:

---

<sup>26</sup> In retrospect, an assumption of  $\overline{W} = 0$  may be more realistic; however since  $\overline{V}$  is small compared to  $\overline{U}$ , the impact on the analyses will be small.

$$\theta_{RMSE} = \frac{\sqrt{\frac{1}{N} \sum_k \sum_l [\theta_1(k,l) - \theta_2(k,l)]^2}}{\theta_s}, \quad (64)$$

where  $\theta_1$  and  $\theta_2$  are variables in datasets 1 and 2 respectively;  $k$  and  $l$  are indices on the vector map; and  $\theta_s$  is a standard value.  $\theta_s$  is the root-mean-square of the variable in question, calculated across the full field, from the entire D60 dataset, excluding rejected vectors.

This comparison was performed ten times for each subset size ranging from 1 to 500, totalling 5000 data points. The MATLAB algorithm to perform the simulation is included in Appendix C. The results are plotted below Figure 48.

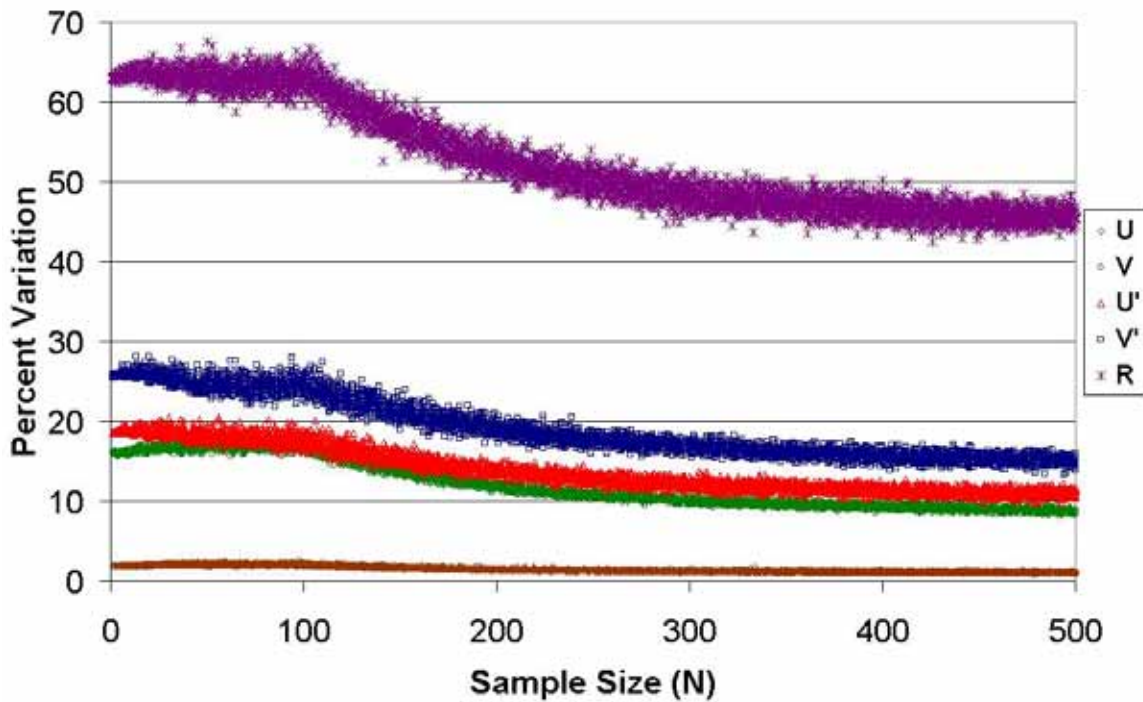


Figure 48 – Monte Carlo simulation results



Care must be taken in evaluating the results of this study. It only reveals the consistency of the data, not its accuracy. A systemic error in the data will not show up here. That being said, if steady state conditions are expected, then variation in the data can be interpreted as a minimum to the error range. Table 8 summarizes the results.

**Table 8 – Monte Carlo simulation summary**

| Quantity | Average variation<br>( $N = 500$ ) |
|----------|------------------------------------|
| $U$ mean | 1.08%                              |
| $V$ mean | 8.68%                              |
| $u'$     | 11.08%                             |
| $v'$     | 14.93%                             |
| $R$      | 45.62%                             |

The variation in  $U$  is small; however,  $V$  varies by nearly 9%. It is likely that the specific set-up used in the experiment made the PIV somewhat insensitive to detecting small velocities, as  $V$  is small compared to  $U$ . It is therefore desirable to compare total velocity vectors in the validation, as opposed to individual components. The last three quantities all vary by greater than 10%. These are all required for calculations involving turbulence. Although these values represent minimum values for the error range, we will use these values to see how they propagate through the turbulence calculations presented in Section 5.5.4.

The uncertainty from the Monte Carlo simulation has been normalized to a standard RMS value for each quantity. To conduct an error analysis we return to the absolute values.

The RMS standards used in the Monte Carlo simulation were:

**Table 9 – RMS standards and errors**

| Quantity              | $U$ mean  | $V$ mean  | $u'$  | $v'$  | $R$    |
|-----------------------|---|---|---|---|--------|
| <b>RMS standard</b>   | 0.9636<br>[ms <sup>-1</sup> ]                   | 98.78 × 10 <sup>-3</sup><br>[ms <sup>-1</sup> ] | 0.1922<br>[ms <sup>-1</sup> ]                   | 0.1590<br>[ms <sup>-1</sup> ]                   | 0.2869 |
| <b>Absolute error</b> | 10.40 × 10 <sup>-3</sup><br>[ms <sup>-1</sup> ] | 8.572 × 10 <sup>-3</sup><br>[ms <sup>-1</sup> ] | 21.31 × 10 <sup>-3</sup><br>[ms <sup>-1</sup> ] | 23.74 × 10 <sup>-3</sup><br>[ms <sup>-1</sup> ] | 0.1309 |
| <b>% error</b>        | 1.08%   | 8.68%   | 11.08%  | 14.93%  | 45.62% |

Error can be expressed as the sum of a mean value and its uncertainty:

$$\theta = \bar{\theta} \pm \Delta\theta \quad (65)$$

There are many techniques to define the uncertainty,  $\Delta\theta$ , including (Robonovich 2005):

- maximum error, where  $\Delta\theta$  refers to the largest error in the dataset;
- probable error, where  $\Delta\theta$  refers to the largest error within a specified probability range;
- average error, where  $\Delta\theta$  refers to the mean absolute value of the deviation; and
- standard deviation, where  $\Delta\theta$  refers to the standard deviation of the values.

In the Monte Carlo analysis from Section 5.6.1, RMS error is used. To handle the error propagation, it is treated as a standard deviation of the values. The basic rules for standard deviation error propagation are outlined below (Robonovich 2005).

Two values,  $A$  and  $B$ , with error  $\Delta A$  and  $\Delta B$  respectively undergo an operation. The result is  $Z$  with error  $\Delta Z$ . It is assumed there is no covariance in the errors between  $A$  and  $B$ . Under addition or subtraction:

$$Z = A \pm B, \quad (\Delta Z)^2 = (\Delta A)^2 + (\Delta B)^2. \quad (66)$$

Under multiplication or division:

$$Z = AB, \quad \left(\frac{\Delta Z}{Z}\right)^2 = \left(\frac{\Delta A}{A}\right)^2 + \left(\frac{\Delta B}{B}\right)^2. \quad (67)$$

Under exponentiation:

$$Z = A^n, \quad \frac{\Delta Z}{Z} = n \frac{\Delta A}{A} \quad (68)$$

Equations (67) and (68) require the mean values  $A$  and  $B$  to calculate the error  $\Delta Z$ . For the analysis below, we use the RMS standards as the mean values. Now we apply these rules to the equations from Section 5.5.4. In calculating  $w'$  with equation (58), the error is:

$$\Delta w' = \frac{1}{2} \sqrt{\Delta u'^2 + \Delta v'^2}. \quad (69)$$

From equation (59), the error is:

$$\Delta uv = uv_s \sqrt{\left(\frac{\Delta R}{R_s}\right)^2 + \left(\frac{\Delta u'}{u_s}\right)^2 + \left(\frac{\Delta v'}{v_s}\right)^2}, \quad (70)$$

The error in equation (60) is:

$$\Delta k = (u'_s \Delta u' + v'_s \Delta v' + w'_s \Delta w'). \quad (71)$$

The error in  $U'$  from equation (62) is:

$$\Delta U' = \frac{u'_s \Delta u' + v'_s \Delta v' + w'_s \Delta w'}{\sqrt{3(u_s'^2 + v_s'^2 + w_s'^2)}}. \quad (72)$$

The error in absolute velocity equation (63) is given by:

$$\Delta \bar{U} = \frac{\bar{U}_s \Delta U + \bar{V}_s \Delta V + \bar{W}_s \Delta W}{\sqrt{U_s^2 + V_s^2 + W_s^2}}. \quad (73)$$

Lastly, the turbulence intensity from equation (61) has the error:

$$\Delta I = I_s \sqrt{\left(\frac{\Delta U'}{U'_s}\right)^2 + \left(\frac{\Delta \bar{U}}{\bar{U}_s}\right)^2}. \quad (74)$$

Using the RMS standards and the errors from the Monte Carlo simulation, the propagated errors through the turbulence calculations are summarized in Table 10.

**Table 10 – Derived quantities and associated errors**

| Quantity                    | $w'$                           | $-uv$   | $k$   | $U'$  | U mean  | $I$                      |
|-----------------------------|--------------------------------|---|---|---|---|--------------------------|
| <b>Derived RMS standard</b> | 0.1756<br>[ms <sup>-1</sup> ]  | 8.772 x 10 <sup>-3</sup><br>[m <sup>2</sup> s <sup>-2</sup> ] | 46.55 x 10 <sup>-3</sup><br>[m <sup>2</sup> s <sup>-2</sup> ] | 0.1762<br>[ms <sup>-1</sup> ]                   | 0.9737<br>[ms <sup>-1</sup> ]                   | 0.1809                   |
| <b>Absolute error</b>       | 0.01595<br>[ms <sup>-1</sup> ] | 1.182 x 10 <sup>-3</sup><br>[m <sup>2</sup> s <sup>-2</sup> ] | 10.67 x 10 <sup>-3</sup><br>[m <sup>2</sup> s <sup>-2</sup> ] | 20.20 x 10 <sup>-3</sup><br>[ms <sup>-1</sup> ] | 12.03 x 10 <sup>-3</sup><br>[ms <sup>-1</sup> ] | 29.08 x 10 <sup>-3</sup> |
| <b>Percent error</b>        | 9.08%                          | 13.47%  | 22.93%  | 11.46%  | 1.24%   | 16.1%                    |

Again we see the velocity has a favourable error. Unfortunately the quantities required for turbulence all have errors of over 10%, the worst one being turbulence kinetic energy,  $k$ , with an error over 20%.

The Monte Carlo simulation has shown the minimum errors in the PIV data to be substantial. Whereas the velocities appear to have a low minimum error, the turbulence related quantities have high minimum errors. Therefore the turbulence data should be interpreted with caution.

### 5.6.2 Resolution errors

The field of view chosen for the PIV experiment was selected to capture a full image of the test model. Although it was expected that such a field of view would reduce the accuracy of the vector plots, it was not anticipated that the errors would be greater than 10%. Later analysis revealed physical impossibilities in some regions, such as a wake flow with accelerating stream-wise velocities, and very large, negative eddy viscosities. The effect of resolution was studied in more detail after the experiment was concluded.

For adequate resolution of the turbulence quantities, the interrogation area size should be close to the same order of magnitude as the Kolmogorov microscale. For instance, at a resolution twenty times larger than this, only 50% of the eddy viscosity dissipation can be calculated (Jung et al. 2005). The Kolmogorov microscale is given by (Smith et al. 1993):

$$\eta_K = \left( \frac{\nu^3}{\varepsilon} \right)^{\frac{1}{4}}, \quad (75)$$

where  $\nu$  is the kinematic viscosity, defined as  $\nu = \mu / \rho$ ; and  $\varepsilon$  is the turbulence eddy dissipation. If the validity of the PIV data is questioned, one cannot use the data itself to measure the velocity gradients to ascertain whether or not it meets the criteria in the equations above. A CFD simulation of the D60 experiment was performed, using the standard  $k$ - $\varepsilon$  turbulence model (refer to Section 6). The results of this simulation were applied to Equation (75). In regions of high turbulence, the Kolmogorov length scale is found to be 0.03 mm. In the PIV experiment, the length of an interrogation area is 7 mm,

more than 200 times larger than the Kolmogorov length scale. Therefore the turbulence quantities cannot be trusted in the experiment.

Furthermore, to select the field of view, interrogation region size, and time between light pulses, two rules are to be balanced (Dantec 2000). First it is recommended that the total change in velocity across an interrogation region be kept small:

$$\frac{|u_{\max} - u_{\min}| \Delta t}{S \bullet d_{IA}} < 0.03, \quad (76)$$

where  $u_{\max}$  and  $u_{\min}$  are maximum and minimum velocities within the interrogation region,  $\Delta t$  is the time between light pulses,  $S$  is the Object: Image scale factor,  $d_{IA}$  is the length of an interrogation area. Second, the maximum expected velocity must be no greater than to displace a seeding particle across 1/4 of the interrogation region:

$$\frac{u_{\max} \Delta t}{d_{IA}} < 0.25. \quad (77)$$

If both these criteria are met, the probability of valid detection remains above 95%. If the criteria are violated, the probability of valid detection declines quickly (Keane et al. 1992). Equation (76) was applied to the standard  $k-\varepsilon$  simulation results, and it was found to have an RMS value of 0.1129. According to the analyses of Keane and Adrian, at this value, the probability of valid detection is approximately 60%. Therefore in regions of high velocity gradients, the velocities cannot be trusted in the PIV results.

### **5.6.3 Seeding density**

The seeding density also must meet some criteria in order for high quality results. To choose seeding density, it was suggested that five seeding particles per interrogation region would give good results (Dantec 2000). A brief inspection of the raw PIV data reveals that in some areas there is an average of less than three seeding particles per interrogation area. The effect of a low seeding density is to cause zero-biasing on the velocities (Keane et al. 1992). Less than three seeding particles per interrogation area can produce a measured velocity up to 55% less than the actual velocity. Therefore the velocities are expected to be under-reported.

## **5.7 Results**

Although the error analysis shows the PIV experiment is unreliable, the results will be reviewed from a qualitative perspective.

### **5.7.1 Velocities and streamlines**

The streamlines are shown in Figure 49 to Figure 51 below. The black silhouette represents the masked vectors, and acts as a good proxy for the shape of the model. In order to give a good visual representation of the flow, streamlines were added as necessary to give an approximately even spacing.

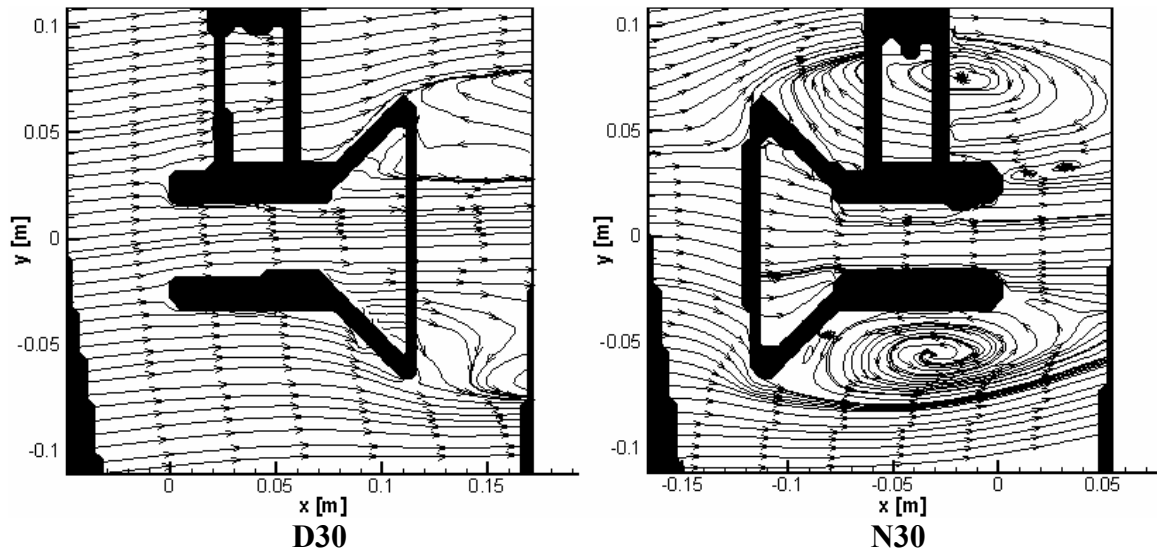


Figure 49 – D30 and N30 streamlines

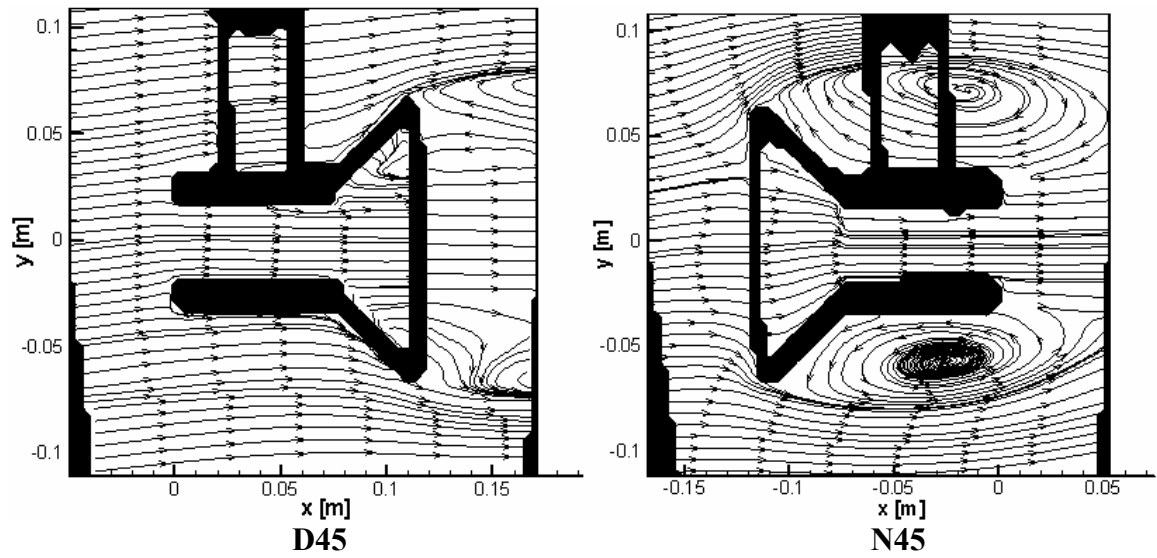


Figure 50 – D45 and N45 streamlines



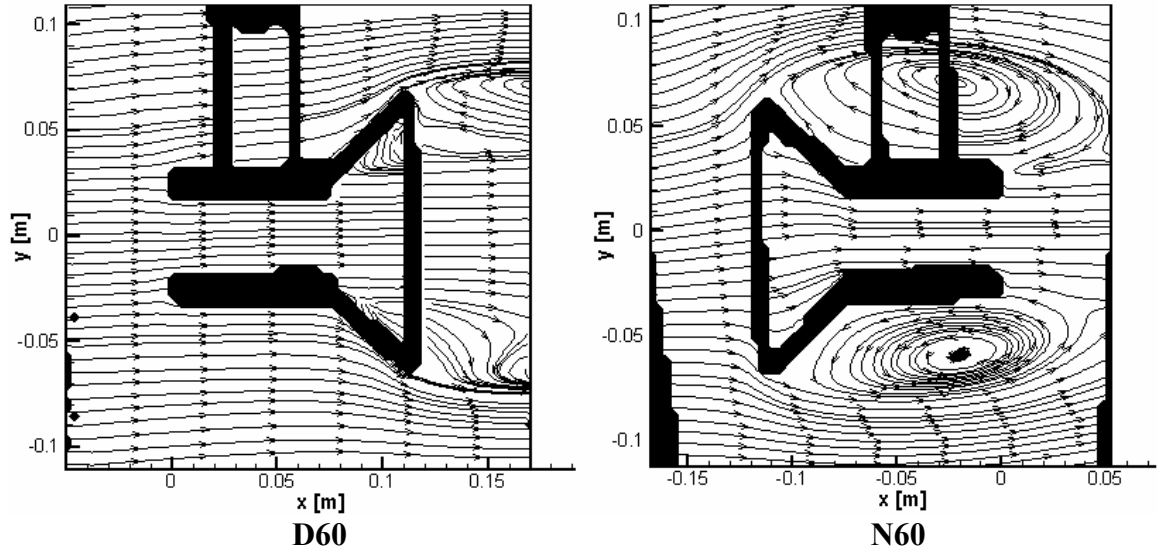


Figure 51 – D60 and N60 streamlines

Velocity contour plots are shown in Figure 52 to Figure 54.

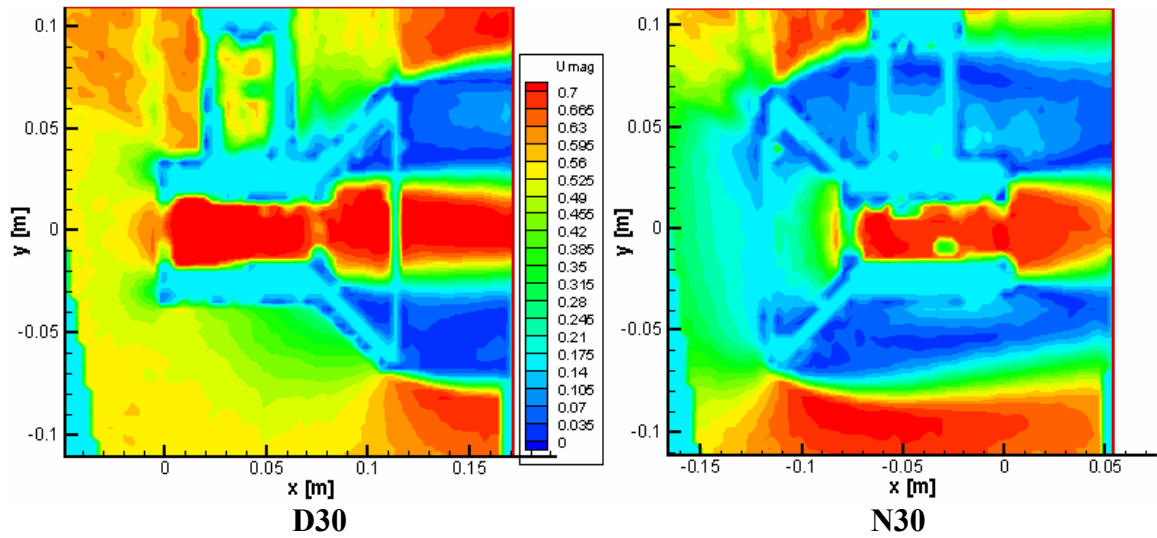


Figure 52 – D30 and N30 velocity contour plots

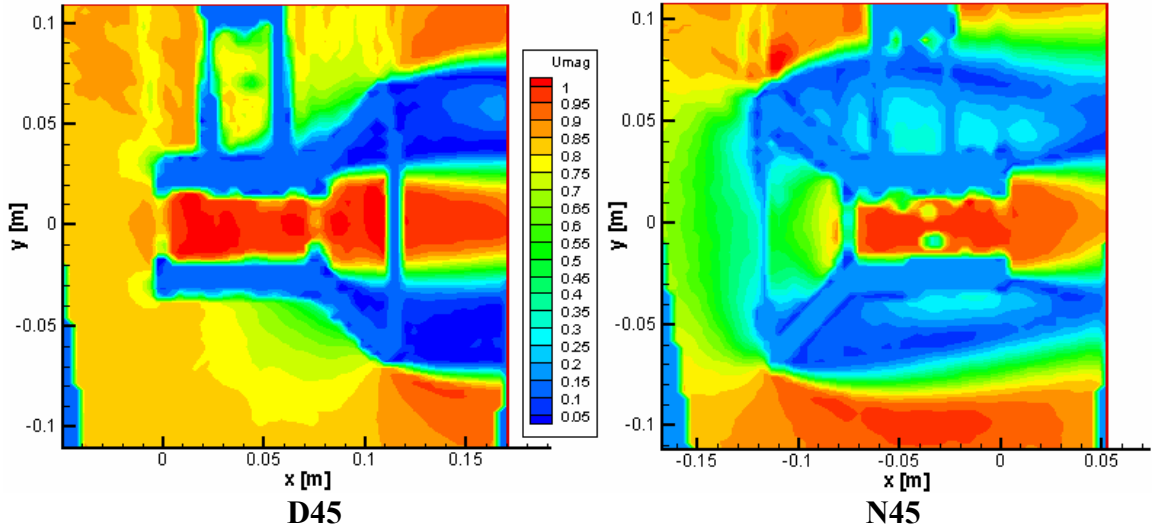


Figure 53 – D45 and N45 velocity contour plots

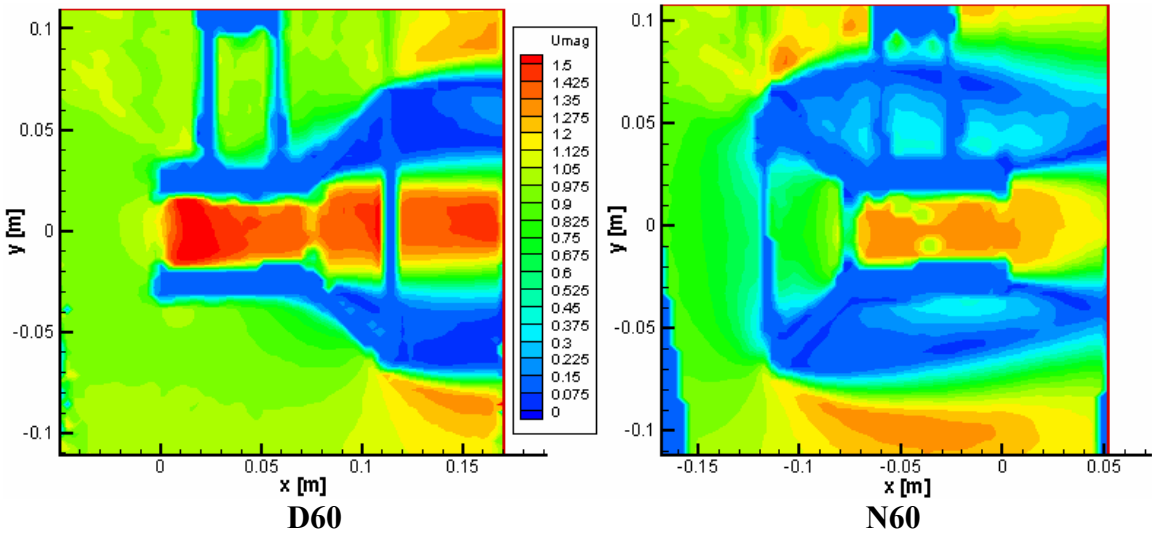


Figure 54 – D60 and N60 velocity contour plots

### 5.7.2 Turbulence

Due to relative similarities in the contour plots, only the 45Hz datasets will be shown below. The turbulence kinetic energy contour plots,  $k$ , are shown in Figure 55.

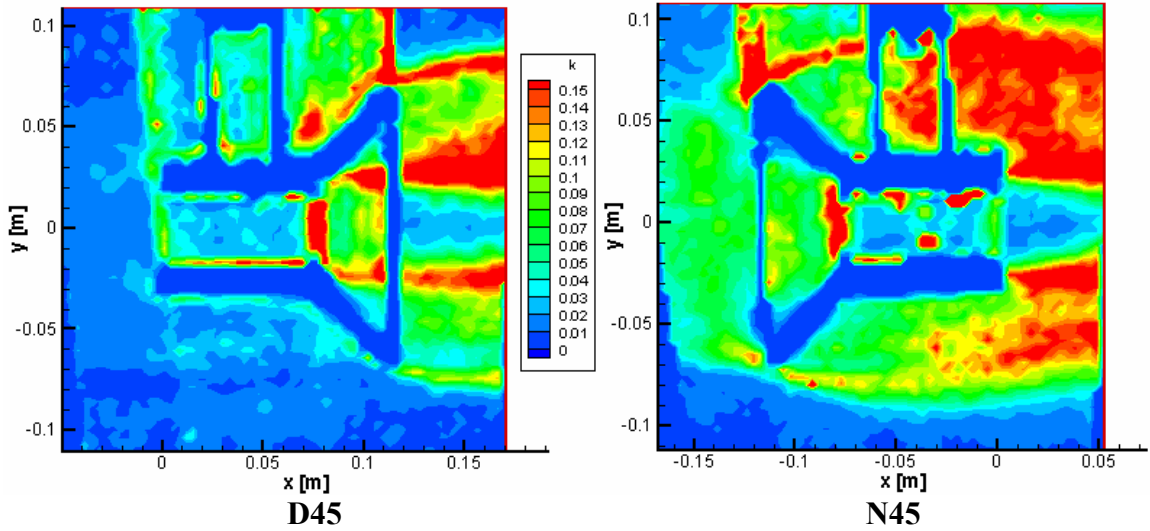


Figure 55 – D45 and N45 turbulence kinetic energy contour plots

Turbulence intensity,  $I$ , is shown in Figure 56.

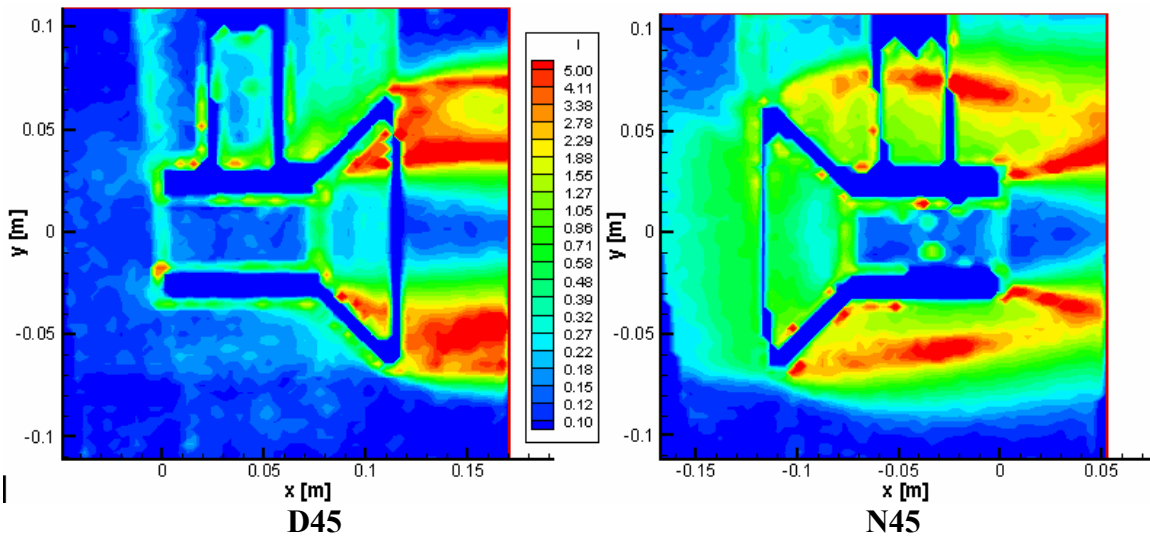
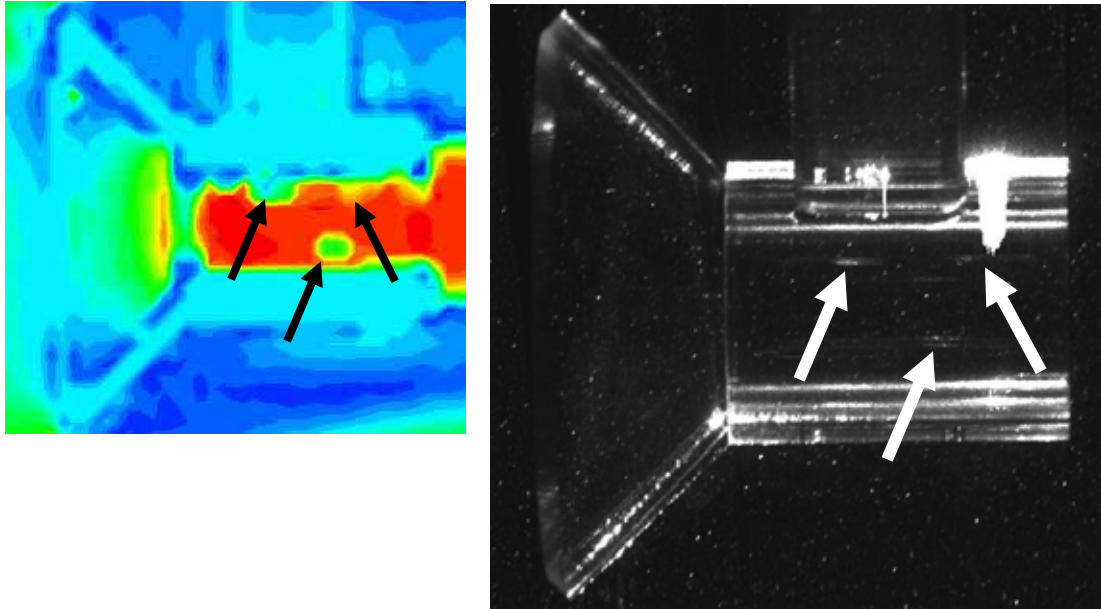


Figure 56 – D45 and N45 turbulence intensity contour plots

## 5.8 Discussion

In Section 5.6, the quality of the PIV was shown to be questionable, and the data here is to be interpreted cautiously. In order to provide a full visual representation, these figures do not include the masking or value blanking described in Section 5.5.2, therefore some unusual features are apparent. All nozzle configurations have unusual spots near the

walls inside the cylindrical section. These spots correspond to optical noise such as over-exposure or reflections, as shown in Figure 57.



**Figure 57 – Nozzle configuration noise**

Similarly, all seam lines and shadow lines show turbulence anomalies, as covered in Section 5.5.2. Masking and blanking are used for all calculations, therefore these sources of error are removed.

In general, the results show significant differences in the flow through a nozzle and a diffuser of the same dimensions. The streamlines show large recirculation zones in the nozzle configuration, and smaller recirculation for the diffuser. The velocity contour plots show that the diffuser consistently produces a larger core velocity than the nozzle. This can be seen in Figure 59, a cross-stream velocity profile, taken from lines shown in Figure 58.

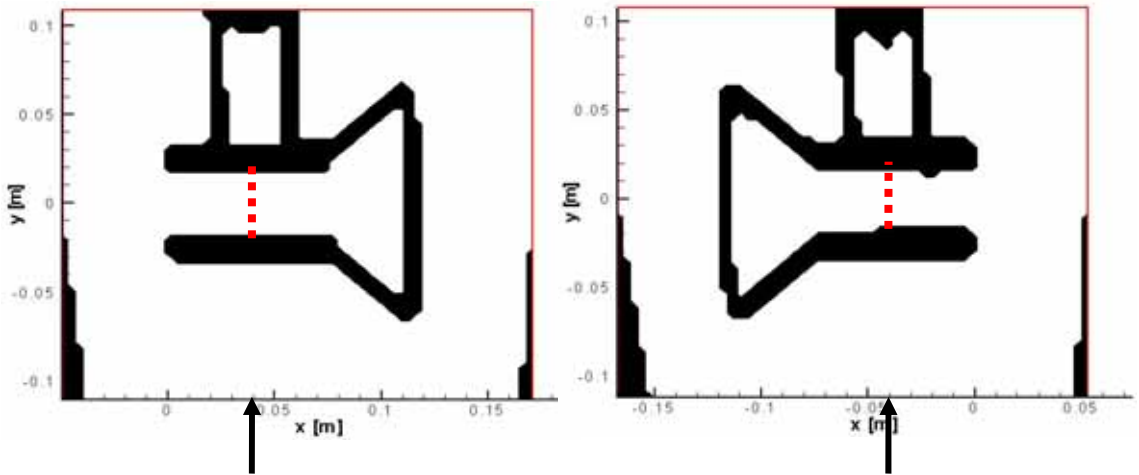


Figure 58 – Cross-stream data extraction

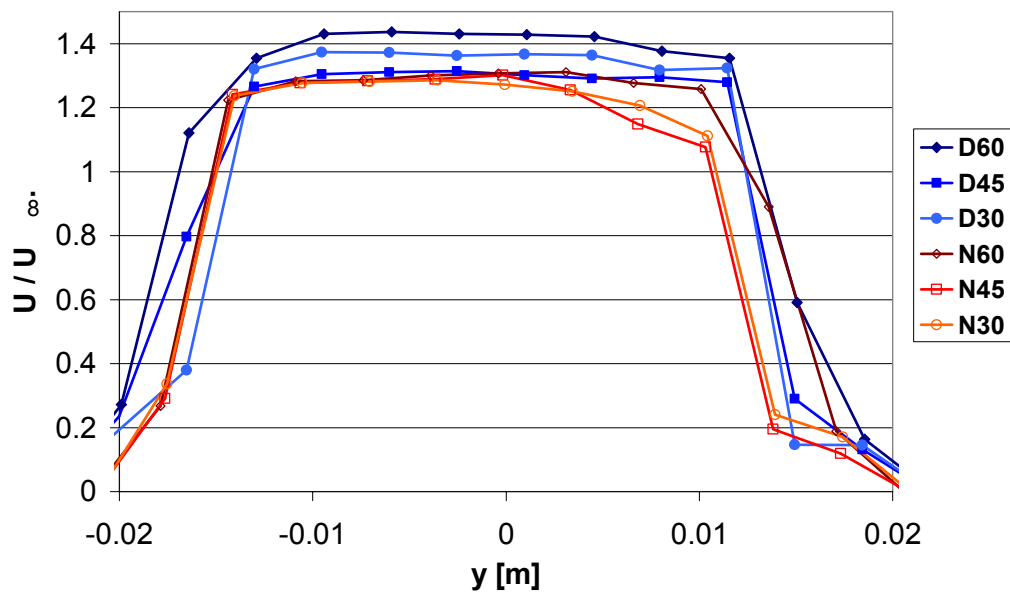


Figure 59 – Velocity profile,  $U / U_\infty$  versus  $y$

The turbulence contours seem to show that the nozzle configuration has a larger effect on the flow, with large upstream influences. It also appears evident that there is a turbulent calm spot within the cylindrical section which continues downstream. This region seems

to have less turbulence than the freestream, a positive prospect for kinetic turbines. The large error in the turbulence quantities renders this discussion purely speculative.

## 6 Validation computational model

A series of numerical simulations are performed to compare various turbulence models for the simulation of the diffuser (no turbine blades). This section details the results of these numerical simulations. A comparison between the numerical simulations and the PIV data is covered later, in Section 7.

**Table 11 – Validation experiment parameters**

| VALIDATION EXPERIMENT |  |   |                |
|-----------------------|--|---|----------------|
| <b>EXPERIMENT</b>     | Objective  |   |                |
|                       | Validate various turbulence models against experimental data |   |                |
|                       | <b>Variable</b>  | <b>Trials</b>   |                |
|                       | Turbulence model, configuration, inlet conditions            | 24  |                |
| <b>FLUID SPACE</b>    | X (streamwise)   | 1.778 [m]   |                |
|                       | Y (cross stream)   | 0.610 [m]   |                |
|                       | Z (vertical)   | 0.610 [m]   |                |
| <b>INLET</b>          | Velocity   | 60 Hz 1.000 [ms <sup>-1</sup> ]<br>45 Hz 0.825 [ms <sup>-1</sup> ]<br>30 Hz 0.535 [ms <sup>-1</sup> ] |                |
|                       | Turbulence Intensity   | 60 Hz 0.12<br>45 Hz 0.12<br>30 Hz 0.35  |                |
|                       | Eddy viscosity ratio   | 60 Hz 120<br>45 Hz 120<br>30 Hz 120   |                |
|                       | <b>OUTLET</b>  | Outlet Pressure 0 [kPa]   |                |
|                       | <b>BOUNDARY WALLS</b>  | Side walls ( $\pm Z$ )  | Smooth wall    |
|                       |  | Top wall (+Y)   | Symmetry plane |
| Bottom wall (-Y)      |  | Smooth wall   |                |
| <b>MESH</b>           | Type   | Tetrahedral   |                |
|                       | Variations   | 2   |                |
|                       | Average size   | 485,000 elements  |                |

All six of the PIV experiment runs were modelled in CFD using four different turbulence models:

- the standard  $k-\varepsilon$  model, described in Section 2.3.3;
- shear stress transport (SST), described in Section 2.3.4;
- Speziale, Sarkar and Gatski (SSG) Reynolds, described in Section 2.3.6; and
- baseline (BSL) Reynolds, described in Section 2.3.7.

## 6.1 Mesh strategy

The Acrylic model and its two brackets were modeled within a block of fluid of equal dimensions as the water tunnel test section. Only two meshes were required for the experiment: the diffuser configuration and the nozzle configuration, not including varying the grid spacing for grid independence tests.

The meshes were created using the software described in Section 2.3.8. Tetrahedrons were used to facilitate rapid meshing. A smoothing algorithm was employed to ensure a high quality mesh. A mesh density requirement was included within the region enclosing the model and the PIV image boundaries to ensure sufficient points were available to interpolate to the PIV grid.

Grid independence was established using the standard  $k-\varepsilon$  model. Identical simulations were performed on three meshes with different grid spacing. Two proxies were used as a means of measuring the relative characteristics of the results: mass flow rate through the

centre of the cylinder was used as a proxy for the overall velocity field; and drag was used as a proxy for the wake zone. The results are summarized in Table 12.

**Table 12 – Grid independence**

| <b>Mesh</b> | <b>No. of elements</b> | <b>Flow rate [kg/s]</b> | <b>Drag [N]</b> |
|-------------|------------------------|-------------------------|-----------------|
| Fine        | 1,151,892              | 2.700                   | 7.567           |
| Medium      | 473,430                | 2.756                   | 7.925           |
| Coarse      | 364,187                | 2.811                   | 8.209           |

The mass flow rate varied by 2% between all three simulations. The drag varied by 4.7% between the Fine and Medium meshes, and by 3.6% between the Medium and Coarse meshes, suggesting that mesh density impacts wake flow more significantly than the overall flow field. These variations were deemed acceptable, and the Medium mesh was selected for further experimentation.

## 6.2 Convergence

Convergence criteria independence was also established. Two identical simulations were performed with different convergence criteria. The results are summarized in Table 13.

**Table 13 – Convergence independence**

| <b>Criteria</b> | <b>Flow rate [kg/s]</b> | <b>Drag [N]</b> |
|-----------------|-------------------------|-----------------|
| 1.00E-04        | 2.796                   | 8.276           |
| 1.00E-05        | 2.794                   | 8.287           |

Drag varied by 0.12% and mass flow rate varied by 0.05%. The variation was insignificant, therefore a convergence criteria of  $1.00 \times 10^{-4}$  was selected for further experimentation.



### 6.3 Inlet conditions

The water tunnel is designed with a contraction cone to give an approximately uniform flow profile at the test section inlet. The inlet in the CFD model corresponded with the test section inlet. Therefore, selecting inlet conditions that are uniform should be an adequate representation for the CFD simulations. Inlet conditions were selected using PIV data for each experiment run. It was determined during the analysis that the inlet for the CFD experiment is further upstream than the viewing window in the PIV experiment. Flow profiles were plotted of the furthest upstream line in the PIV data, as shown in Figure 60.

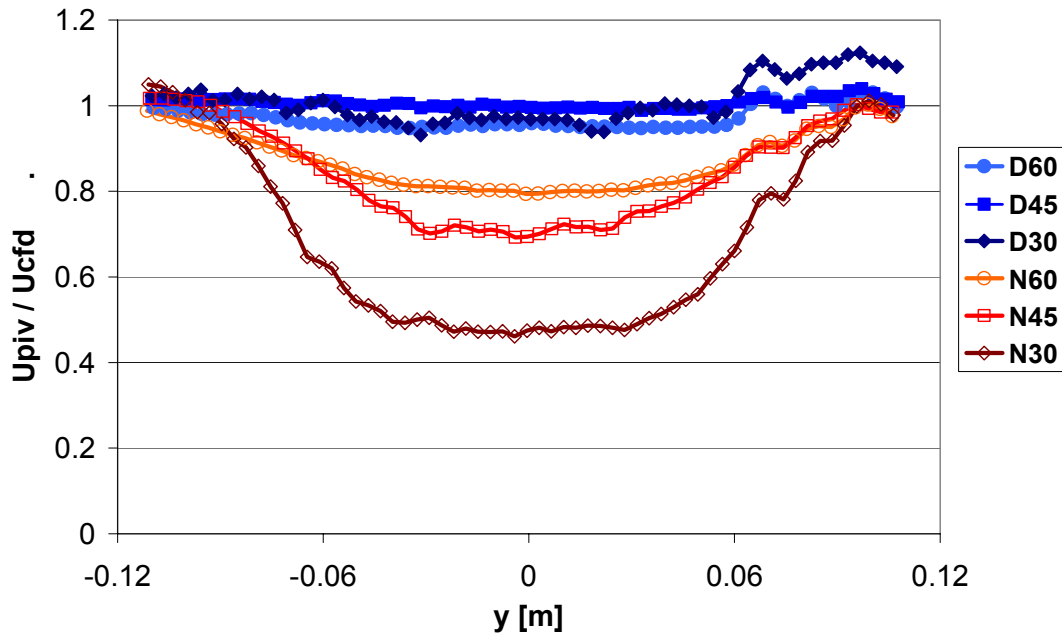


Figure 60 – Inlet flow conditions

The nozzle-configured experiments were found to have obvious disturbances originating from the model. The diffuser profiles were more uniform. Therefore, the inlet conditions were selected as the average of each of the diffuser profiles. It is believed that the

additional upstream distance in the CFD model will allow the flow to develop from uniformity, to capture the disturbances seen in the nozzle-configured experiments. The inlet conditions are shown in Table 14.

**Table 14 – Inlet conditions**

| <b>Pump frequency</b> | <b>Velocity [ms<sup>-1</sup>]</b> | <b>Turbulence intensity</b> | <b>Eddy viscosity ratio</b> |
|-----------------------|-----------------------------------|-----------------------------|-----------------------------|
| 30 [Hz]               | 0.535                             | 0.35                        | 100                         |
| 45 [Hz]               | 0.825                             | 0.12                        | 100                         |
| 60 [Hz]               | 1.000                             | 0.12                        | 100                         |

To improve on this technique, rather than using uniform flow, one can produce an inlet profile from the PIV data, and apply this profile across the CFD inlet, making some reasonable assumptions for variation across the  $z$  axis.

## **6.4 Results**

The velocity and turbulence profiles are described in this section. The discussion is in Section 6.5.

### **6.4.1 Velocities and streamlines**

All four turbulence models are presented below for comparison. Only the 60 Hz simulations are shown for brevity. Streamlines and velocity contours for the diffuser configurations are shown in Figure 61 and Figure 62.

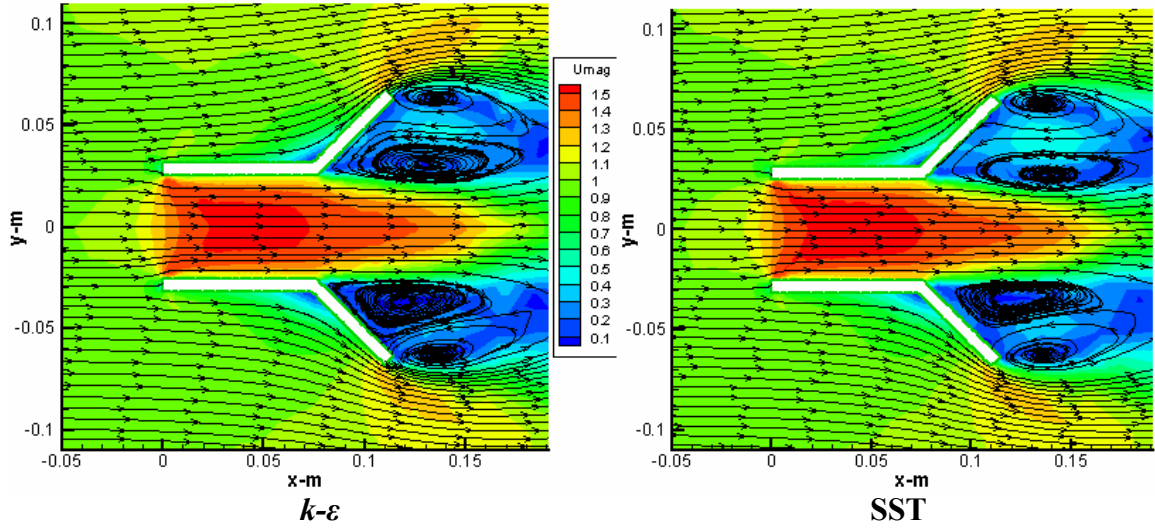


**Figure 61 – D60 streamlines and velocity contours for  $k-\epsilon$  and SST**

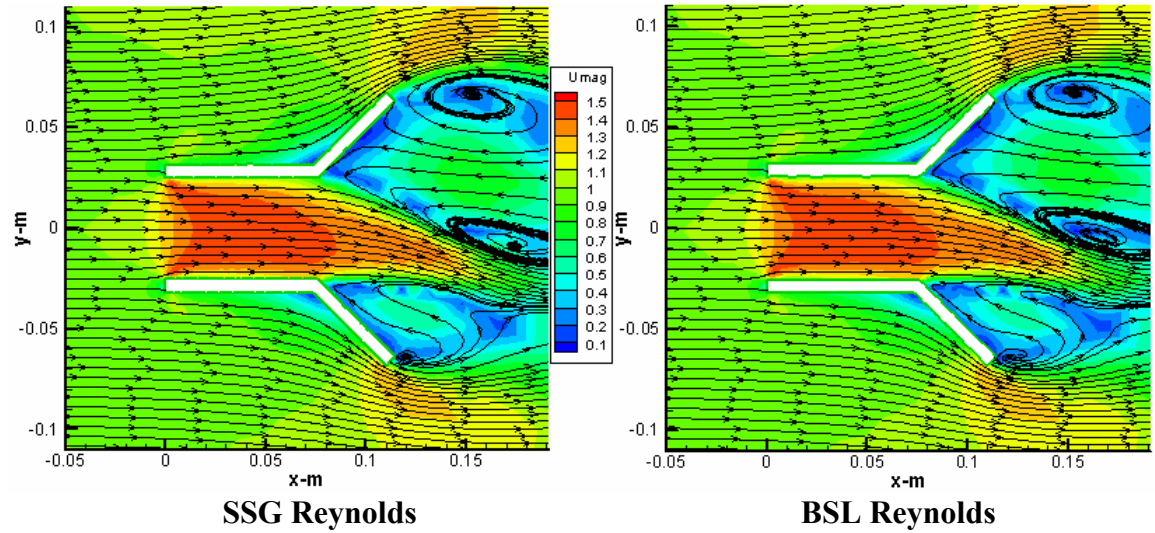


**Figure 62 – D60 streamlines and velocity contours for SSG and BSL**

The unusual downward tapering of the core flow seen in Figure 62 is addressed in the discussion below. Streamlines and velocity contours for the nozzle configuration are shown in Figure 63 and Figure 64.

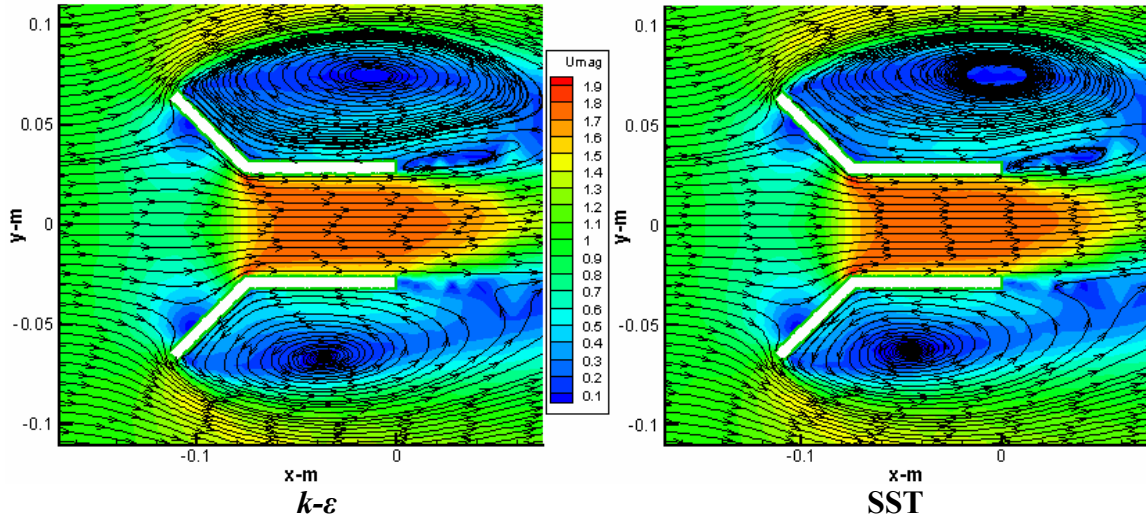


Figure 63 – N60 streamlines and velocity contours for  $k-\varepsilon$  and SST

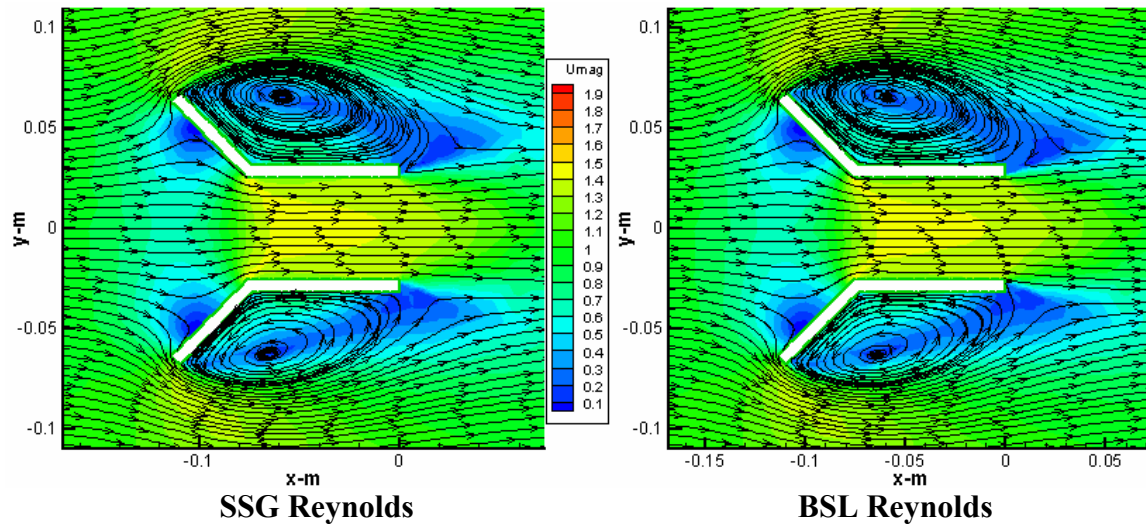


Figure 64 – N60 streamlines and velocity contours for SSG and BSL

#### 6.4.2 Turbulence

Turbulence kinetic energy contours are shown in Figure 65 to Figure 68. Note the difference in colour scales between the eddy-viscosity turbulence models ( $k-\varepsilon$  and SST) and the Reynolds stress turbulence models (SSG and BSL). The two turbulence model types calculated dramatically different turbulence quantities.

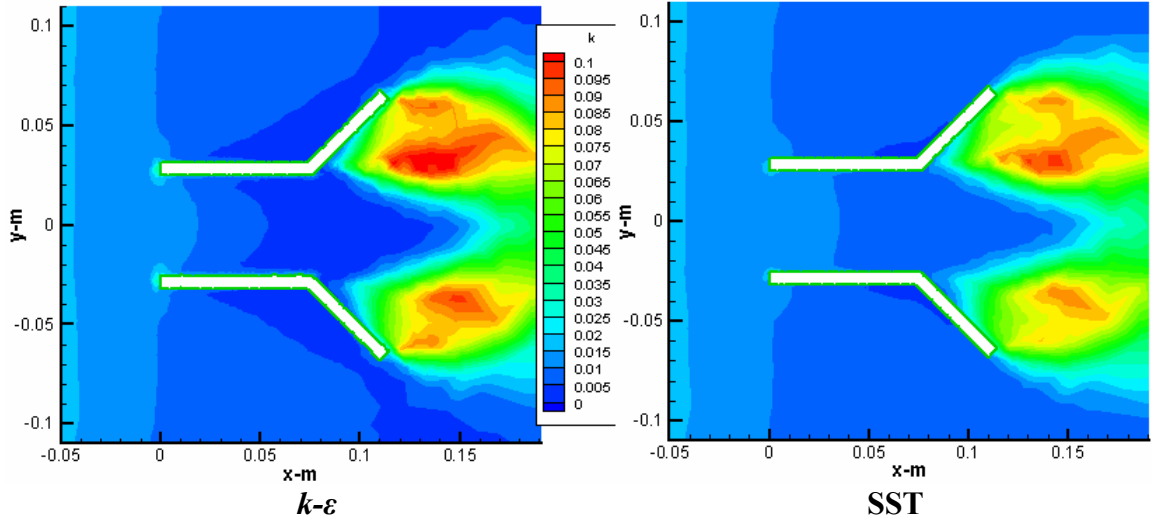


Figure 65 – D60 turbulence kinetic energy contours for  $k-\varepsilon$  and SST

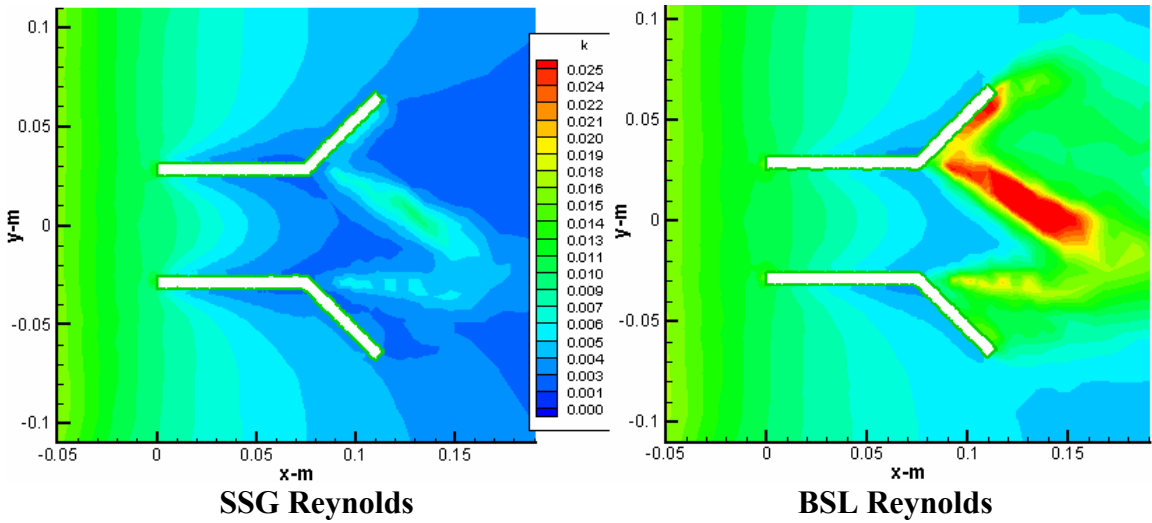
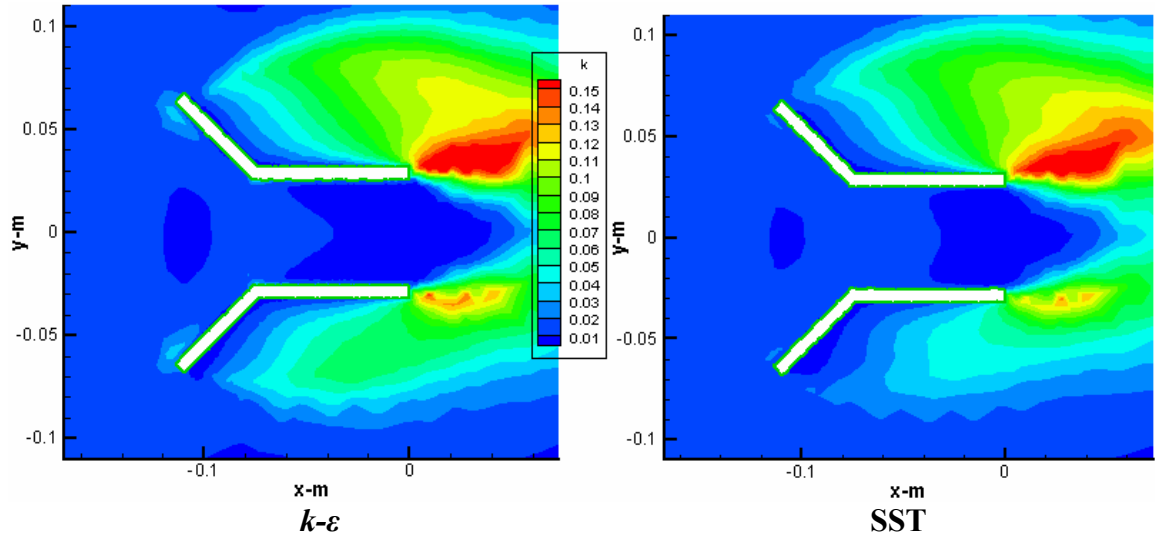
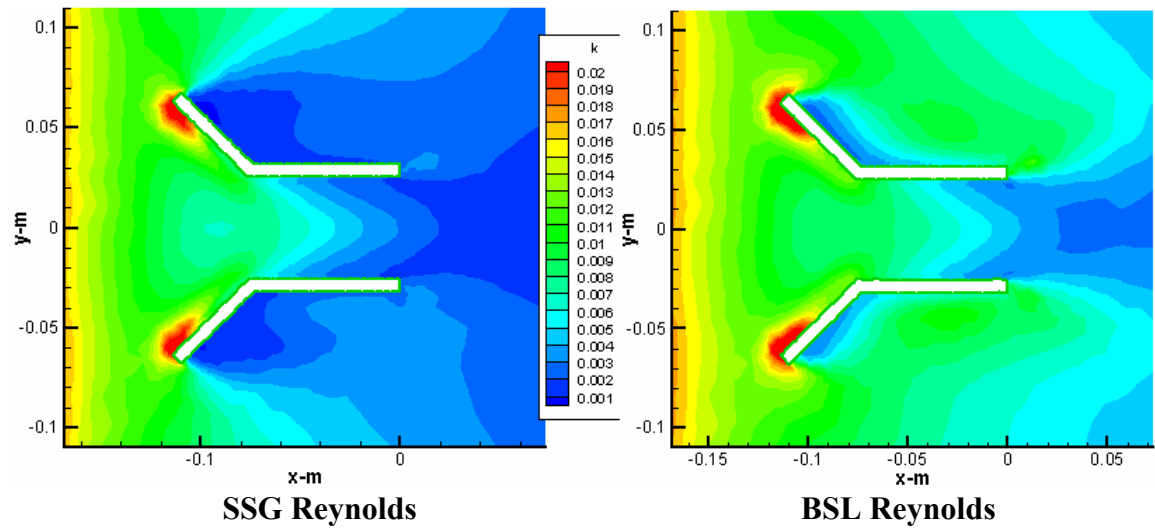


Figure 66 – D60 turbulence kinetic energy contours for SSG and BSL



**Figure 67 – N60 turbulence kinetic energy contours for  $k-\epsilon$  and SST**



**Figure 68 – N60 turbulence kinetic energy contours for SSG and BSL**

Turbulence intensity contour plots are shown in Figure 69 to Figure 72.

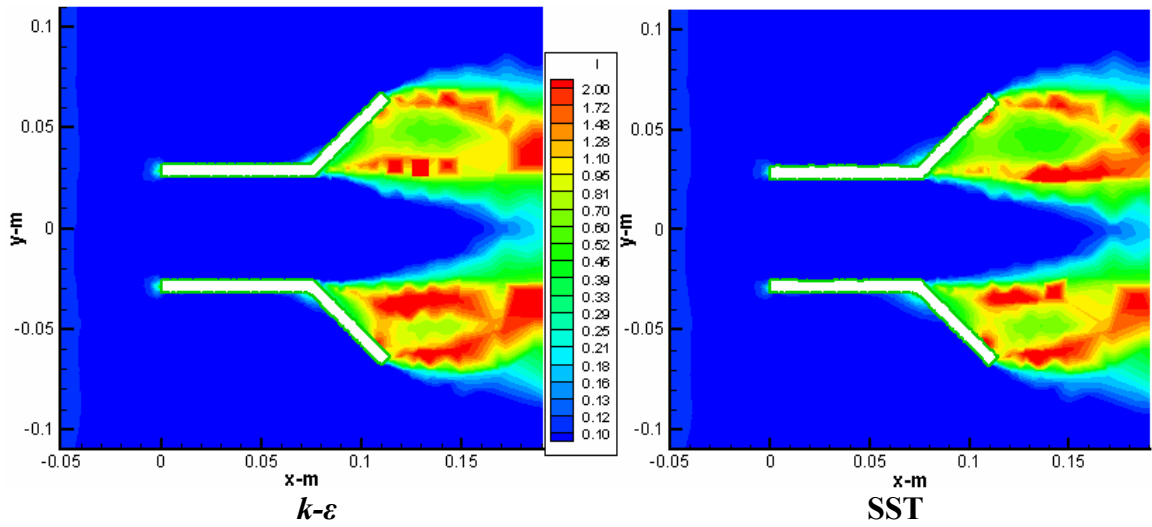


Figure 69 – D60 turbulence intensity contours for  $k-\epsilon$  and SST

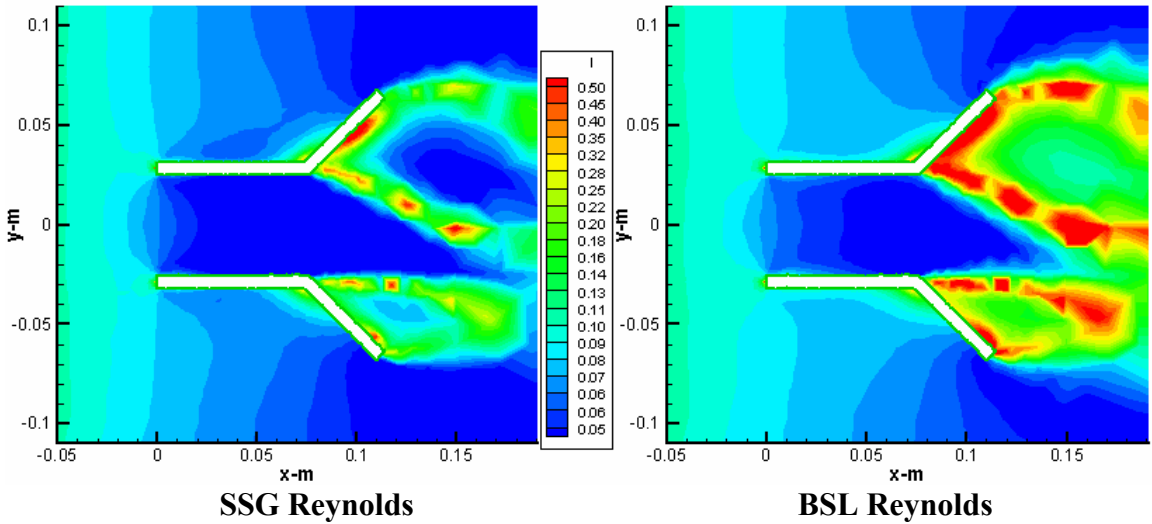


Figure 70 – D60 turbulence intensity contours for SSG and BSL

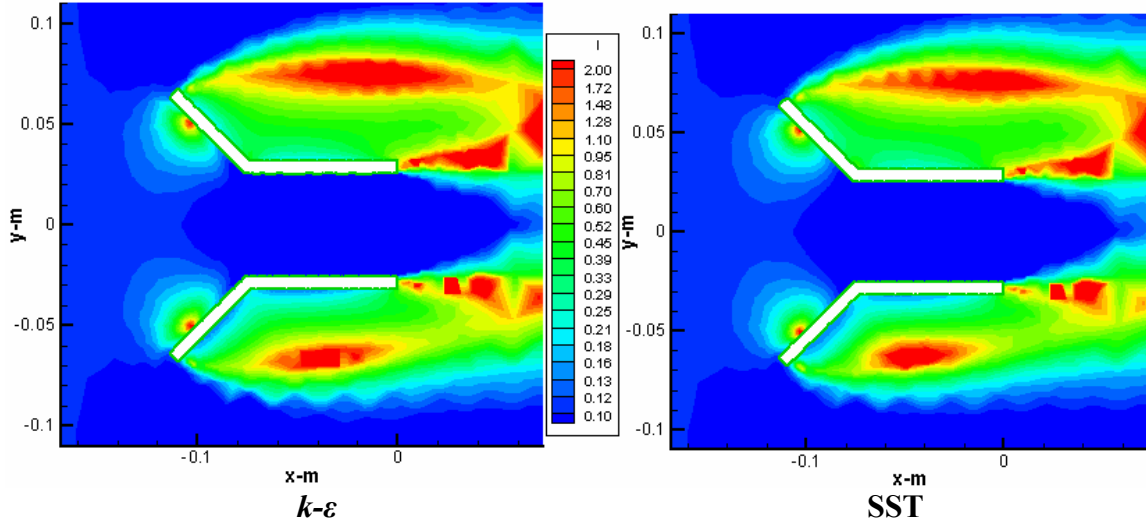


Figure 71 – N60 turbulence intensity contours for  $k-\varepsilon$  and SST

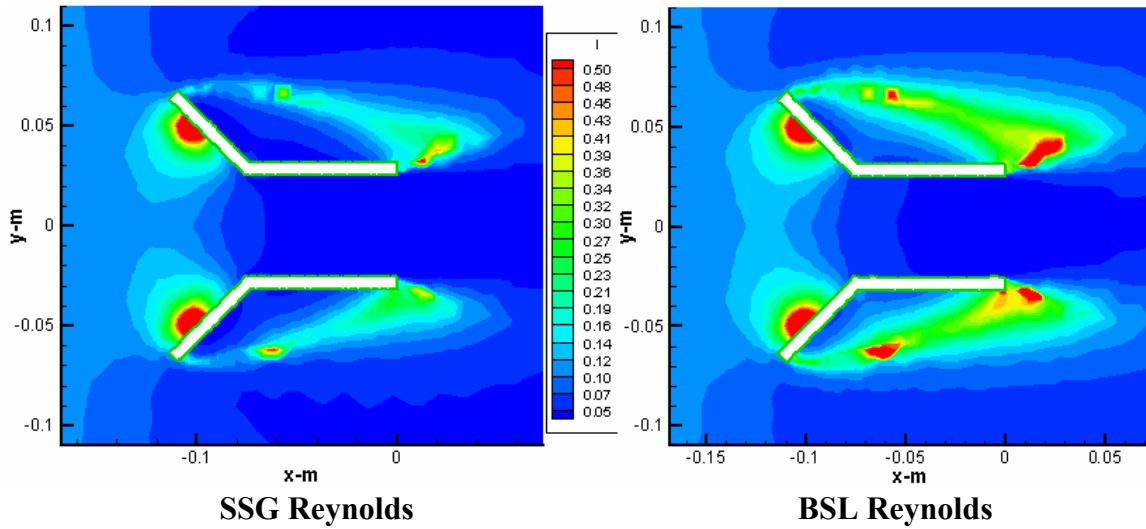


Figure 72 – N60 turbulence intensity contours for SSG and BSL

## 6.5 Discussion

The results separate the eddy-viscosity turbulence models from the Reynolds stress transport models (RSTM), as described in Sections 2.3.2 and 2.3.5 respectively. There is little difference between the results of the standard  $k-\varepsilon$  simulations, and the SST simulations; this was also the case between the SSG Reynolds and the BSL Reynolds simulations. However, between these two groups, there were significant differences.



Comparing the velocity fields, the Reynolds stress transport models (SSG and BSL) both show a peculiar downward motion of the core wake in the D60 simulation, as shown in Figure 62. The eddy-viscosity models ( $k-\varepsilon$  and SST) also showed asymmetry, such as the position of the wake vortices, but there was far less asymmetry in these models. The CFD model included the brackets, so asymmetrical flow is expected; however the flow seen in Figure 62 appears excessively asymmetrical. Closer inspection of the three-dimensional output reveals this downward tapering motion is part of a more complex flow structure in which the bulk of the wake splits into two parts, as shown in Figure 73.

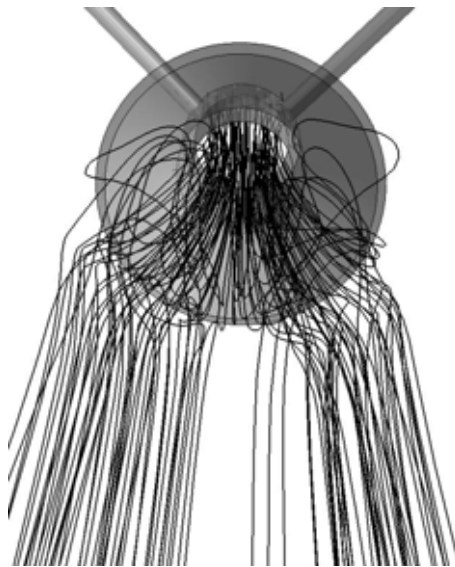


**Figure 73 – D60 wake streamlines for the SSG Reynolds turbulence model**

The asymmetry of the flow does correspond to the asymmetry of the model.

The nozzle simulations also show differences between model types, particularly evident when studying the location of recirculation zones. The eddy-viscosity turbulence models predict the recirculation zones to be asymmetrically located on the top and bottom of the cylinder, with an additional recirculation zone at the top trailing edge of the cylinder, as shown in Figure 63. On the other hand, the Reynolds stress transport models have the two recirculation zones further forward with less asymmetry, as shown in Figure 64. The additional recirculation zone at the trailing edge of the eddy-viscosity models is not present in these.

The turbulence fields also show dramatic differences. For example, comparing Figure 67 with Figure 68, we see entirely different turbulence structures. In this series of experiments, Reynolds stress models tended to predict considerably less turbulence than eddy-viscosity turbulence models. In the N60 simulation, the difference was several orders of magnitude. The differences in the turbulence predictions developed as the flow moved downstream. Upstream, the differences were small, whereas downstream, the differences quickly developed to several orders of magnitude. The different scales on the contour plots above renders this difficult to see, but at the inlet of the model, the turbulence kinetic energy and turbulence intensity show very little variation between trials. For example, turbulence intensity plots are shown in Figure 74 with identical scales.



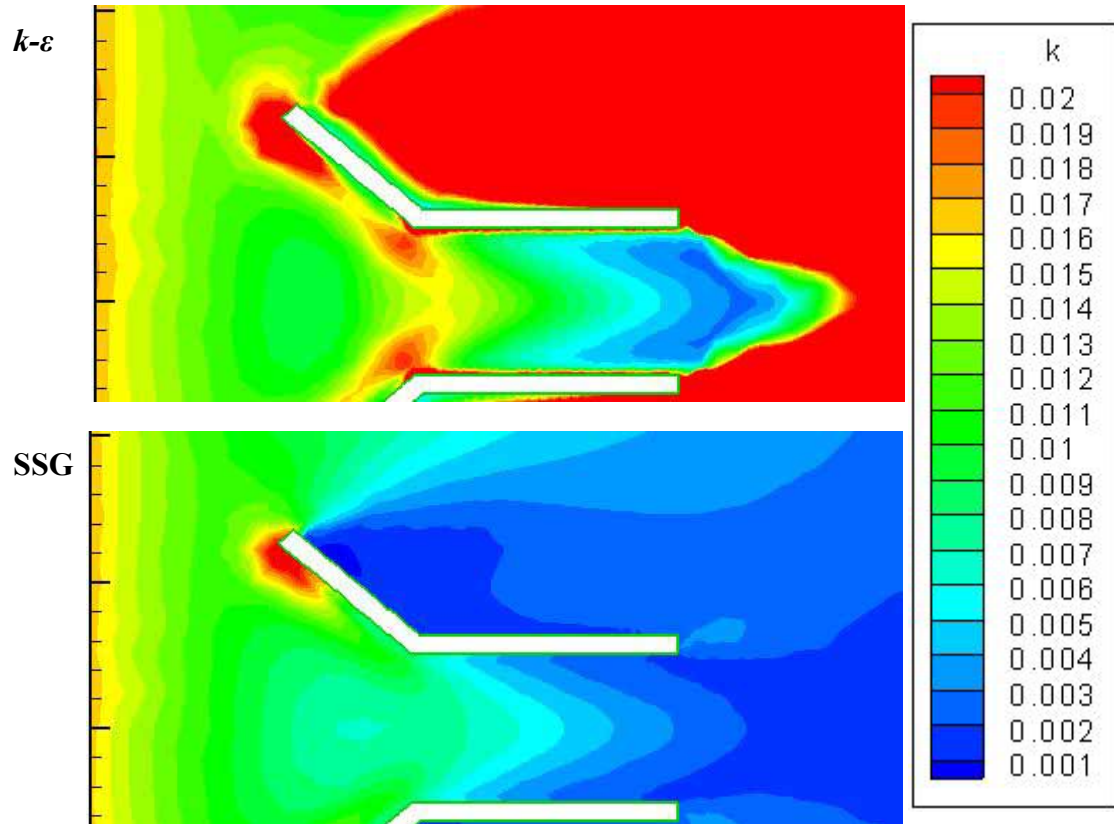


**Figure 75 – N60 turbulence kinetic energy using identical scales**

As seen above, the two models behave similarly until the flow separates from the top leading edge of the nozzle, at which point the  $k-\epsilon$  model predicts significantly higher turbulence energy. Furthermore, the flow in the downstream portion of the cylindrical section is similar until exiting at the trailing edge.

The two eddy-viscosity turbulence models,  $k-\epsilon$  and SST, showed very little differences in their solutions. The models differ most significantly with their near-wall treatment, as their calculations of unbounded shear flow are both based on the  $k-\epsilon$  model<sup>27</sup>. It is

<sup>27</sup> The SST model is actually based on a  $k-\omega$  formulation. In unbounded shear flows, the SST turbulence model uses a  $k-\omega$  adaptation of the  $k-\epsilon$  model. The results show the differences are small for these conditions.

apparent that the near-wall differences do not significantly affect the full-field solutions of these models under these conditions.

The two Reynolds models did show some discernable differences. The BSL Reynolds model predicted slightly higher turbulence quantities than the SSG.

To evaluate the differences between the nozzle configuration and the diffuser configuration, drag and flow rate quantities were calculated from the solution sets, as shown in Figure 76.

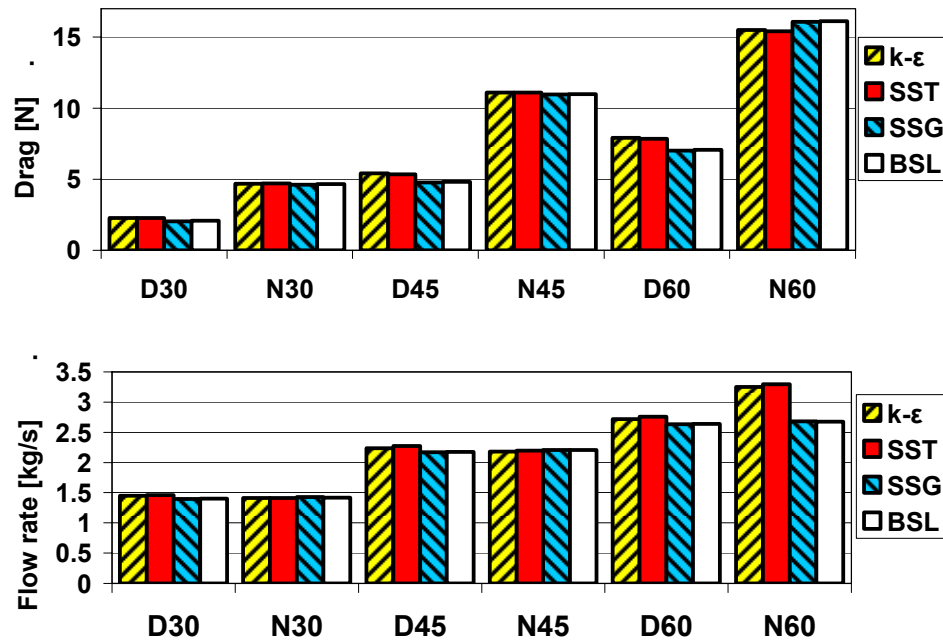


**Figure 76 – Drag force and mass flow rate**

On average, the nozzle configuration produced 2.14 times more drag than the diffuser.

There was no statistical significance to the difference in the mass flow rate pass through

the model. These results show that a diffuser has improved performance over a nozzle of the same dimensions.

The significant differences between turbulence models highlights the importance of conducting a validation. The similarities seen within each category of turbulence model, and the stark differences seen between these categories shows that it is important to include one turbulence model from each category when conducting a validation. It may seem tempting to use a single turbulence model to characterise the performance of the entire category, thus facilitating rapid turbulence model selection, but this practice is equivalent to apply a statistical average to a single instance. With these differences understood, we now turn to a comparison with experimental data.

## 7 Validation comparison

The reliability of a CFD model varies dramatically depending on the flow conditions. In this section, the CFD results will be compared against the PIV data.

### 7.1 Validation procedure

To compare the data, the CFD results are interpolated to the PIV grid by kriging, an interpolation algorithm included with Tecplot<sup>28</sup> (Amtec 2003). Derived quantities are calculated for PIV and CFD as described in Section 5.5.4. The PIV data is masked and blanked as described in Section 5.5.2, to remove sources of error. The remaining data are then compared. The RMS error is calculated to determine the overall performance of each turbulence model. Contour plots of the local errors are used to identify regions of poor performance.

### 7.2 Results

The validation calculation is performed locally and across the full field.

#### 7.2.1 Local validation

Local calculations are performed to find the error between the CFD model and the PIV data. The error is calculated using this template:

$$e = \frac{|\theta_{CFD} - \theta_{PIV}|}{\theta_s}, \quad (78)$$

where  $e$  is the error,  $\theta$  is a fluid dynamics quantity to be compared, and  $\theta_s$  is the RMS standard developed in Section 5.6.

---

<sup>28</sup> Tecplot 10 is copyright Amtec Engineering Inc., 1988-2003

Turbulence models can be broken into two categories: eddy-viscosity based models, and Reynolds stress turbulence based models. As discussed in Section 6.5, turbulence models within the same category have shown very little difference; while there are significant differences between categories. Therefore, for brevity, only  $k-\varepsilon$  and BSL Reynolds models are shown below. The discussion regarding these results is in Section 7.3. All figures use identical linear colour scales, with blue corresponding to 0% error, and red corresponding to 100% or greater error. The velocity errors are shown in Figure 77 and Figure 78.

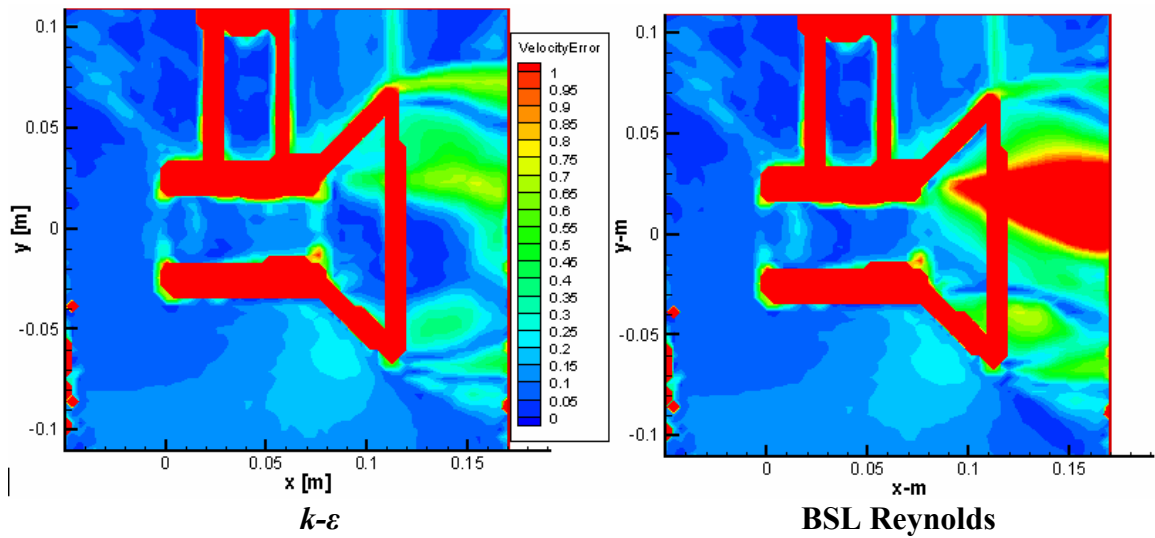


Figure 77 – D60 velocity error for  $k-\varepsilon$  and BSL



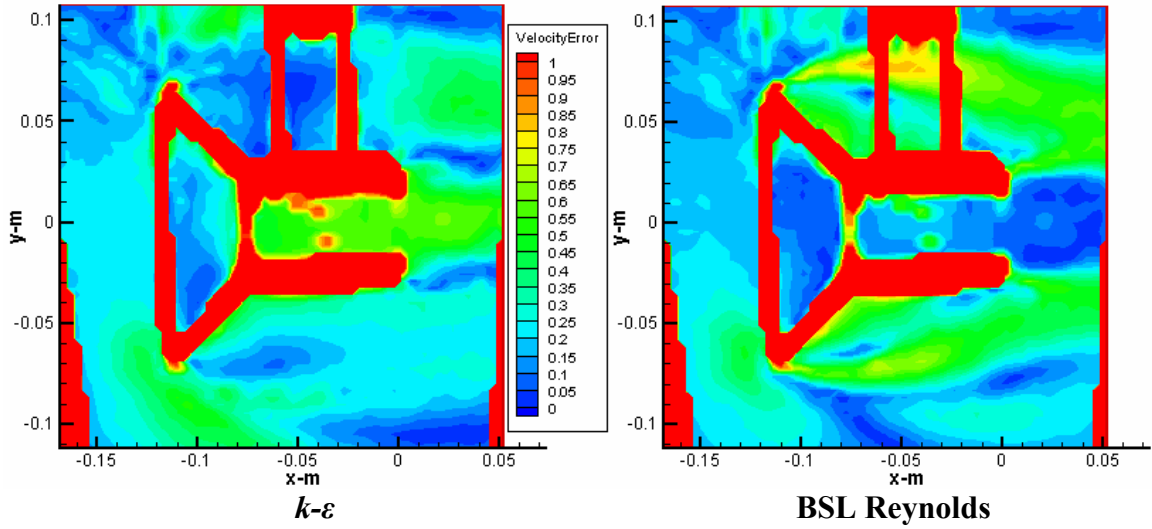


Figure 78 – N60 velocity error for  $k-\epsilon$  and BSL

Turbulence intensity error plots are shown in Figure 79 and Figure 80 below.

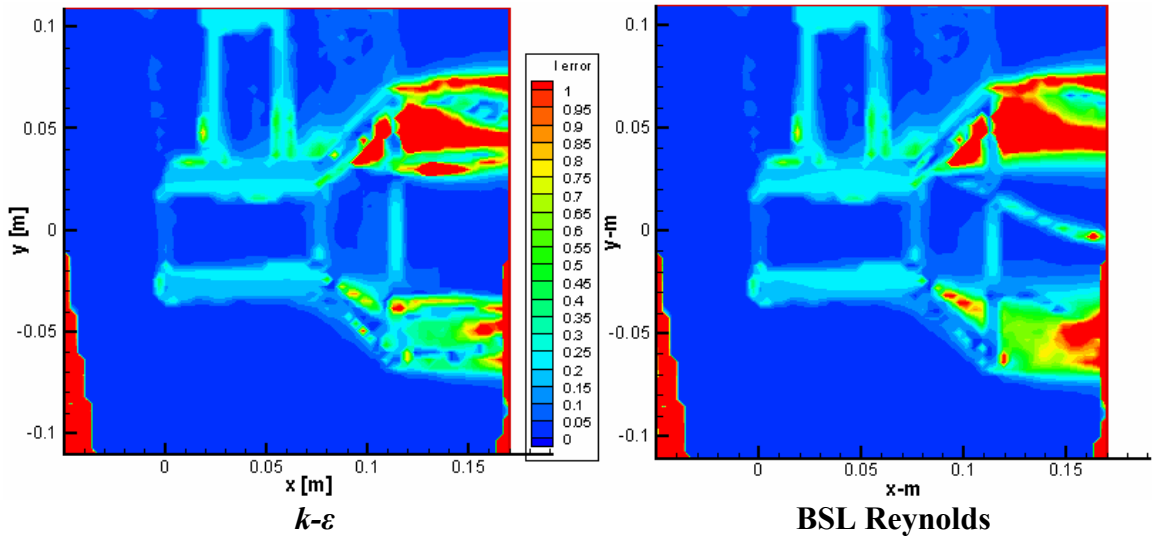


Figure 79 – D60 turbulence intensity error for  $k-\epsilon$  and BSL

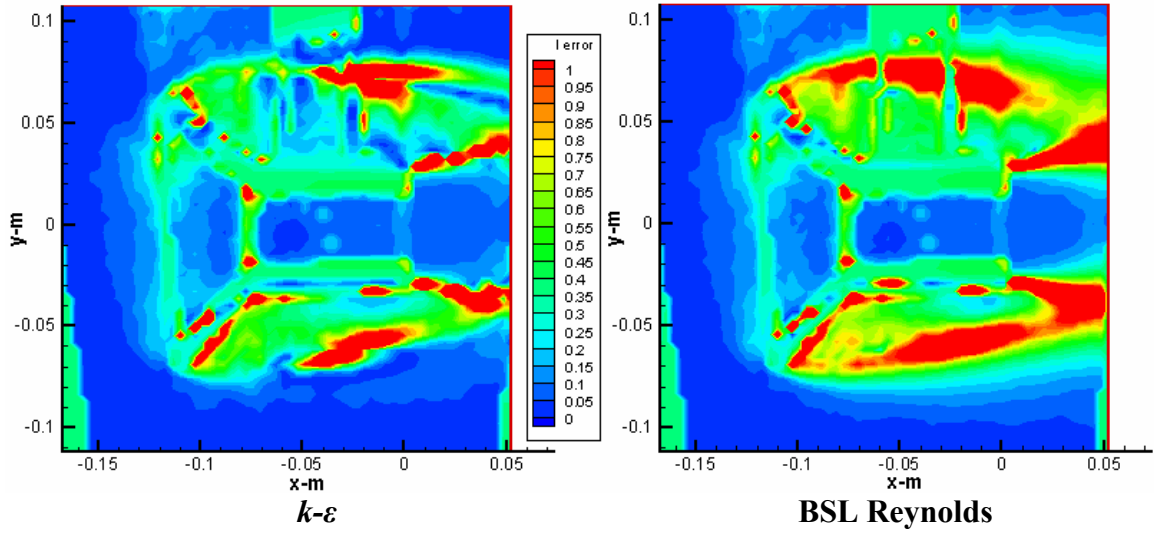


Figure 80 – N60 turbulence intensity error for  $k-\epsilon$  and BSL

Turbulence kinetic energy error plots are shown in Figure 81 and Figure 82.

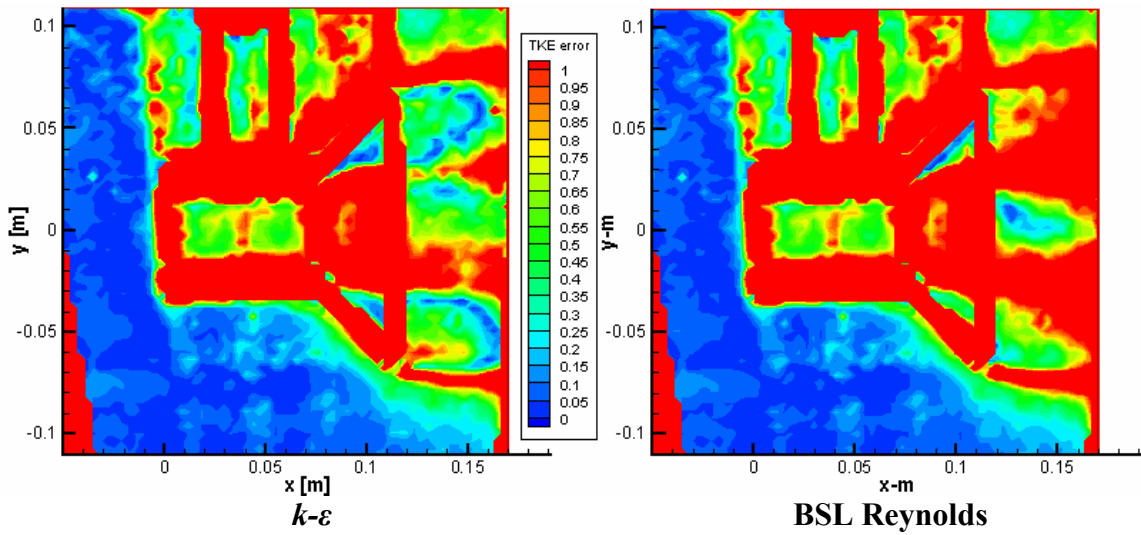


Figure 81 – D60 turbulence kinetic energy error for  $k-\epsilon$  and BSL

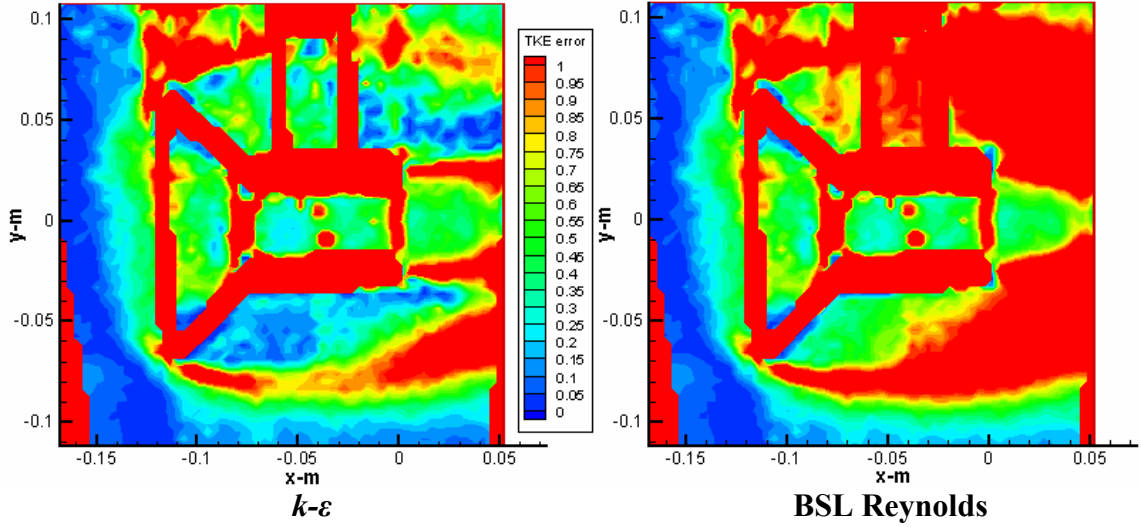


Figure 82 – N60 turbulence kinetic energy error for  $k-\varepsilon$  and BSL

### 7.2.2 Full-field validation

The full field validation can be calculated using RMS error (Liang et al. 2002):

$$\theta_{RMSE} = \frac{\sqrt{\frac{1}{N} \sum_k \sum_l [\theta_{CFD}(k,l) - \theta_{PIV}(k,l)]^2}}{\theta_s}, \quad (79)$$

where  $k$  and  $l$  are indices corresponding to  $x$  and  $y$  locations in the flow field. Results of the full field validation are presented in Figure 83 to Figure 85.

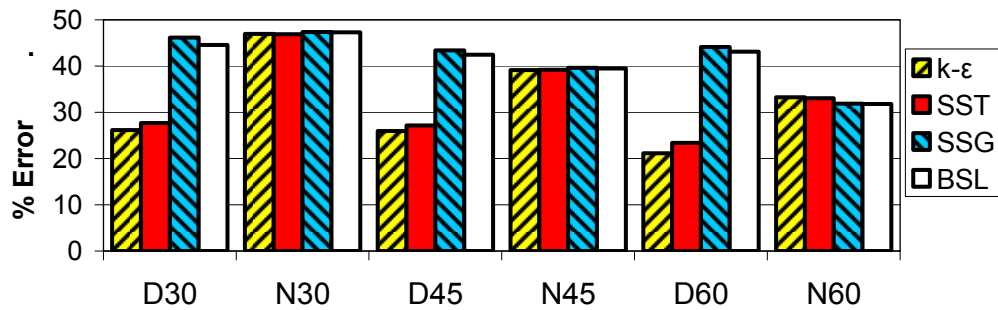


Figure 83 – Velocity RMS error

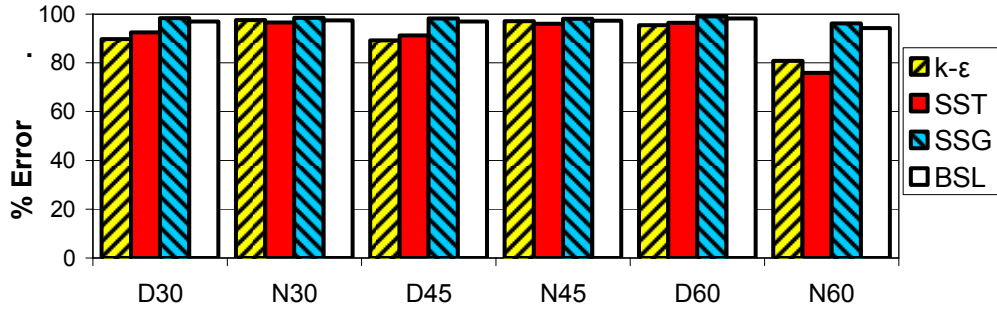


Figure 84 – Turbulence intensity RMS error

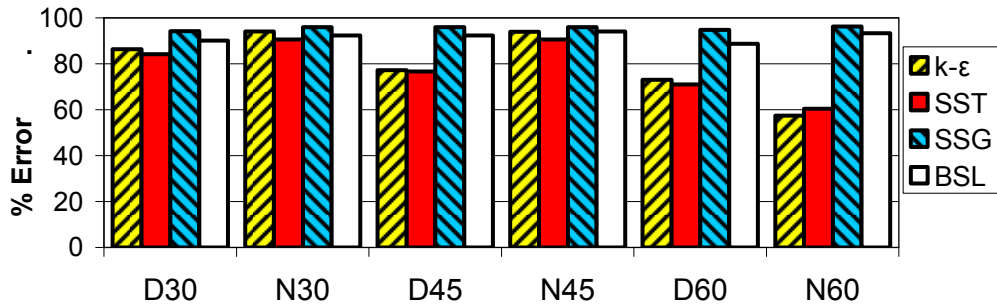


Figure 85 – Turbulence kinetic energy RMS error

### 7.3 Discussion

Masking and value blanking were omitted from the plots above in order to give a full visual representation of the model. For this reason, some anomalies are visible. Masking and blanking are employed for the full field calculations. See Section 5.8 for further discussion.

With full field RMS errors of between 21.2% to 99.1%, it is obvious that validation was not achieved. Apart from a general failure of all four turbulence models, there are two potential causes of this: experimental error in the PIV data, and inlet conditions in the CFD model.

As covered in Section 5.6, there was a high degree of error in the PIV experiment, particularly the turbulence data. The error in the CFD models was correlated with the PIV errors calculated in the Monte Carlo simulation shown in Table 10. That is, the CFD model predicted velocity with the least amount of error, with higher errors for turbulence intensity and turbulence kinetic energy.

The inlet conditions inadequately represented the experimental data. As described in Section 6.3, the CFD model was initialized with uniform inlet flow, the value of which was derived from an average of the upstream data in the diffuser-configured PIV experiments. It was noted that the nozzle-configured PIV data showed significant disturbances in the upstream flow profile, as shown in Figure 60 on page 116. It was assumed that the extra fluid space modelled upstream of the PIV data would allow the flow to develop sufficiently to capture these disturbances. However, Figure 78 shows an initial velocity error of 15 to 25% at the upstream end. This suggests that the inlet conditions were not adequately represented in the nozzle configurations. Furthermore, vertical velocities were assumed to be zero at the inlet. By comparing the PIV streamlines with those from the CFD model, it is obvious this assumption was also incorrect. In Figure 86, the PIV data clearly shows an upward motion at the inlet, whereas the CFD data does not. It is possible that the small differences upstream translated into large differences downstream. Furthermore, the PIV would have significant errors given the large gradients shown by the CFD simulation downstream of the diffuser.

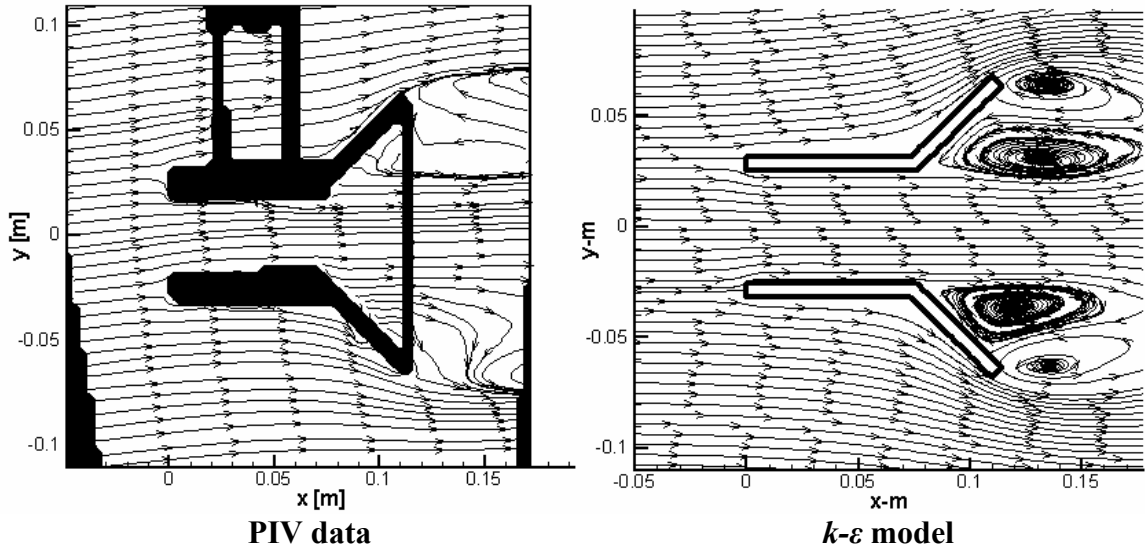


**Figure 86 – D30 streamlines for PIV and  $k-\varepsilon$**

Although validation was not achieved, qualitative observations can be made. In general, the eddy-viscosity turbulence models performed better than the Reynolds stress turbulence models. The downwards tapering of the core wake observed in the diffuser solutions of the Reynolds stress turbulence model (RSTM), as discussed in Section 6.5, were not observed in the PIV data. Therefore a large region of error greater than 100% is seen in the wake area of the RSTM solution, as shown in Figure 77. The eddy-viscosity models fared better, but the locations of recirculation zones were predicted too far upstream, as observed in Figure 86. The RSTM solutions showed a better handling of the interior cylindrical flow, particularly in the nozzle configurations, supporting the suggestion these turbulence models handle axisymmetric geometries better than eddy-viscosity models (Cho et al. 1991). A significant difference seen in turbulence models was in the predictions of unbounded shear flow. The eddy-viscosity model solutions showed a significant superiority over the RSTM solutions in their turbulence predictions

of unbounded shear flow; however all turbulence models showed multiple regions with large error.

Although the differences across turbulence model categories were obvious, the differences within each category were small. This is not surprising because the largest formulaic differences between the models of the same category is their near-wall treatment. Low resolution, coupled with masking prevented any study of the near-wall region. Therefore it is difficult to assess the relative performance of turbulence models within the same category.

Based on these numbers, and given their reliability, using qualitative arguments, this study indicates that the optimum turbulence model for studying open-channel diffuser and nozzle flow is one that uses the eddy-viscosity hypothesis. The output of the standard  $k-\varepsilon$  and SST turbulence models are too close to compare, given the quality of the data and the simulations. Further validation studies are necessary in the future.

## 8 Conclusion

River kinetic hydropower is a promising alternative energy source capable of producing electricity with minimal environmental impact. Rapid deployment and consistent energy production make the technology attractive to rural communities. The modular nature make this technology easily adaptable to distributed power generation. However, there is little in the technical literature covering river kinetic hydropower, a deficit this thesis attempts to start addressing. The fundamentals of modelling this technology are covered, and experiments are performed to evaluate the performance of the models. The models are then adapted to investigate enhancement techniques to improve the river kinetic turbine technology. The theory and formulation of four two-equation turbulence models are detailed, and a validation study is performed. Experimental error and inadequate boundary conditions hinder the validation; however, the results suggest that an eddy-viscosity based turbulence model may be superior to a Reynolds stress turbulence model for these flow conditions. Four different techniques of modelling the rotor are studied, including a momentum source model for rapid prototyping and a rotating reference frame model for fine-tuning. An experiment is performed to compare the momentum source model against theory, and it is found to perform well, with a consistent over-prediction of power output by approximately 5%. The momentum source model and rotating reference frame model are then used in a series of experiments evaluating the benefits of using a ducted shroud to enhance the performance of the rotor. The momentum source model is used to optimize the shroud design, and a design is found that enhances the power output by a factor of 3.1, with the adverse effect of increasing drag by a factor of 3.9. The momentum source model also demonstrates that when the cross-sectional area is a design



limitation, it is beneficial to sacrifice some of the rotor diameter for shroud area. The rotating reference model echoes the results of the momentum source model but to a lesser degree. The rotating reference frame model finds a power increase by a factor of 1.5 using similar conditions as the momentum source model. It is shown that some differences are expected between the models due to the fact that the momentum source model assumes a fixed power extraction ratio, whereas the rotating reference frame model assumes fixed rotor geometry. However, the rotating reference frame model also reveals the highly adverse effects of enclosing the rotor in a straight cylindrical shroud. Such a design can cause a 70% drop in the power output. It is suggested that the expansion regime of the ducted shroud should coincide with the natural flow expansion at the rotor. Unfortunately, the optimised shroud design was created under the constraint that it contain a cylindrical section throughout the length of the rotor, and therefore a new optimisation experiment is required. The risk of cavitation is briefly studied, and it is found not to be a concern. The power-loss caused by the river boundary layer is studied. A mitigation technique that involves altering the geometry of an upstream anchor block is proposed and studied. Four anchor blocks are studied, each with different fundamental design principles. It was found that anchor blocks designed to maximize their cross-stream disturbance in the boundary-layer, particularly vertically, had the most significant impact on the downstream power density. A power increase of 33% is observed at a distance of over 12 m downstream of the anchor block, although this power increase is only available in the upper half of the river cross-section.

## 8.1 Future study

The validation study shows how different turbulence models can give significantly different results; turbulence kinetic energy can differ by several orders of magnitude in some cases. This underscores the importance of choosing the correct turbulence model and the need for further development in this field to solve practical problems. The validation performed in this thesis was hindered by experimental error and inadequate boundary conditions, giving a full field RMS error of over 20%. Another validation is necessary before numerical results can be trusted. Furthermore, no validation was conducted for turbine rotors. The geometry of the rotor is an important aspect of river kinetic hydro power, therefore optimisation of the rotor geometry, as well as the risk of cavitation needs to be addressed in more detail the future. In order to maintain versatility, the rotor may require optimisation against a diverse background of flow conditions, as well as different angular velocities of the rotor. Furthermore, mechanical and electrical losses need to be included. Additional studies on shroud optimisation would further benefit the technology, including the elimination of any straight cylindrical sections. It is suggested that the diffuser be designed with the perspective that it is a cylindrical wing, opening a vast array of enhancements already established in the field of wing design, such as flaps and turbulators. Furthermore, no modifications were considered on the inlet, including the possibility of stators, something that should be studied in the future. The impact this technology may have on fish populations must be fully understood before large-scale deployment is considered, particularly if leading edge stators are used, or if the pressure drop across the rotor becomes significant. Results from the anchor study above suggest that upstream objects can impact power densities far

downstream. Therefore, the interaction between multiple river kinetic turbines should also be investigated if turbine arrays are to be considered. The effect of river boundary layers was only briefly studied, and should be followed up. Finally, the mitigation of damage from foreign debris, including logs, should also be studied.

## **Bibliography**

Al-Sulaiman, F. A., Jamjoum, F. A., 1992. "Applications of wind power on the east coast of Saudi Arabia," *Renewable Energy*, v. 2, n. 1, pp. 47-55.

Amtec Engineering Inc., 2003. Tecplot user's manual, version 10. Bellevue, Washington, USA: Amtec Engineering Inc..

ANSYS Inc., 2005. ANSYS CFX-Solver, Release 10.0. Canonsburg, PA: ANSYS Inc..

Barth, T. J., Jespersen, D. C., 1989. "The design and application of upwind schemes on unstructured meshes", AIAA paper 89-0366.

Bet, F., Grassmann, H., 2003. "Upgrading conventional wind turbines," *Renewable Energy*, v. 28, i. 1, pp. 71-78.

Betz A., 1926. "Wind-Energie und ihre Ausnutzung durch Windmuehlen," Bandenhoeck & Ruprect, Göttingen.

Bibeau, E.L., 2006. "Extraction d'énergie de l'écoulement fluvial", CHOC, Magazine de L'Association de l'industrie électrique du Quebec, 24 (2) Octobre 2006.

Bibeau, E.L., 2005. "Integrating alternative energy technologies in the electricity sector", Forum on Hydropower 2005, Canadian Hydro Power Association, Gatineau, Quebec, October 2005

Brennen, C. E., 1995. Cavitation and bubble dynamics. New York: Oxford University Press. Also available at <http://caltechbook.library.caltech.edu/1/04/bubble.htm> (2007-01-18).

Cho, N., Fletcher, C. A. J., 1991. "Computation of turbulent conical diffuser flows using a non-orthogonal grid system," Computers and Fluids, v. 19, pp. 346-361.

Dantec Measurement Technology A/S, 2000. FlowMap installation and user's guide: 5<sup>th</sup> edition. Skovlunde, Denmark: Dantec Measurement Technology A/S.

Danish Wind Industry Association, "Proof of Betz's law", article within a web site (anonymous). Accessed 2007-01-10, available at <http://www.windpower.org/en/stat/betzpro.htm>

Davidson, P. A., 2004. Turbulence, an Introduction for Scientists and Engineers. New York: Oxford University Press Inc..

Gaden, D. L. F. and Bibeau, E. L., 2006. "Increasing power density of kinetic turbines for cost-effective distributed power generation," POWER-GEN Renewable Energy Conference, Las Vegas, NV, April 10-12, 2006.

Gao, G. and Yan, Y., 2004. "Partial-average-based equations of incompressible turbulent flow," International Journal of Non-Linear Mechanics, v. 39, pp. 1407-1419.

Google, DigitalGlobe, TerraMetrics, NAVTEQ. Satellite image of Churchill River, Manitoba. Accessed 2007-01-10, available at <http://maps.google.ca/?ie=UTF8&z=14&ll=55.940596,-97.354317&spn=0.023362,0.080338&t=k&om=1>

Grassmann, H., Bet, F., Cabras, G., Ceshia, M., Cobai, D., DelPapa, C., 2003. "A partially static turbine - first experimental results," Technical note, Renewable Energy, v. 28, i. 11, pp. 1779-1785.

Grassmann, H., Bet, F., Ceschia, M., Ganis, M. L., 2003. "On the physics of partially static turbines," Renewable Energy, v. 29, pp. 491-499.

Grassmann, H., Ganis, M. L., 2004. "On partially static Kaplan turbines," Renewable Energy, v. 30, pp. 179-186.

H. N. Halvorson Consultant Ltd., 1994. Evaluation of Nova Energy Ltd.'s hydro turbine. Prepared for the Ministry of Employment and Investment, Government of British Columbia.

Harlow, F. H., Nakayama, P. I., 1968. "Transport of turbulence energy decay rate," Los Alamos Science Laboratory, LA-3854.

Házi, G., 2004. "On turbulence models for rod bundle flow computations," Technical note, *Annals of Nuclear Energy*, v. 32, pp. 755-761.

Helmy, M. L., 1991. "Dimensions of the axial flow turbine design for wind power," Technical note, *Renewable Energy*, v. 1, n. 2, pp. 303-307.

Horák, J., 1972. "Comments on the definition of turbulence", *Studia Geophysica et Geodaetica*, v. 16, pp. 186-196.

Igra, O., 1981. "Research and development for shrouded wind turbines," *Energy Conversion and Management*, v. 21, pp. 13-48.

Igra, O., 1981. "Shrouded wind turbine research in Israel," *International Journal of Ambient Energy*, v. 2, pp. 85-96.

Johnson, H. K., Karambas, T. V., Avergis, I., Sanuttigh, B., Gonzalez-Marco, D., Caceres, I., 2005. "Modelling of waves and currents around submerged breakwaters", *Coastal Engineering*, v.52, pp. 949-969.

Jones, W. P., Launder, B. E., 1972. "The prediction of laminarization with a two-equation model of turbulence," *International Journal of Heat and Mass Transfer*, v. 15, pp. 301-304.

Jung, K. H., Chang, K. A., Huang, E. T., 2005. "Two-dimensional flow characteristics of wave interactions with a free-rolling rectangular structure," *Ocean Engineering*, v. 32, pp. 1-20.

Keane, R. D., Adrian, R. J., 1992. "Theory of cross-correlation analysis of PIV images," *Applied Scientific Research*, v. 49, pp. 191-215.

Kolmogorov, A. N., 1942. "Equations of turbulent motion of an incompressible fluid," *Izv. Akad. Nauk SSSR*, v. 6, n. 1-2, p. 56.



Koskela, H., 2004. "Momentum source model for CFD-simulation of nozzle duct air diffuser," *Energy and Buildings*, v. 36, pp. 1011-1020.

Lagström, G. E., 2003. Sätt att omvandla rörelseenergi i havsströmmar till rotationsenergi. Swedish patent number F03B 13/22 7/00, in Swedish.

Launder, B. E., Reece, G. J., Rodi, W., 1975. "Progress in the development of a Reynolds-stress turbulence closure," *Journal of Fluid Mechanics*, v. 68, pp. 537-566.

Launder, B. E., Spalding, D. B., 1974. "The numerical computation of turbulent flows", *Computer Methods in Applied Mechanics and Engineering*, v. 3, pp. 269-289.

Lewis, R. I., Williams, J. E., Abdelghaffar, M. A., 1977, "A theory and experimental investigation of ducted wind turbines," *Wind Engineering*, v. 1, pp. 104-125.

Liang, D. F., Jiang, C. B., Li, Y. L., 2002. "A combination correlation-based interrogation and tracking algorithm for digital PIV evaluation," *Experiments in Fluids*, v. 33, pp. 684-695.

Lipej, A., 2004. "Optimization method for the design of axial hydraulic turbines," *Journal of Power and Energy*, v. 218, pp. 43-50.

Lissaman, P. B. S., Radkey, R. L., 1979. "Coriolis program: a review of the status of the ocean turbine energy system," Oceans 79, fifth annual conference, pp. 559-565.

Lai, Y. C., So, R. M. C., Hwang, B. C., 1989. "Calculation of planar and conical diffuser flows," AIAA Journal, v. 27, pp. 347-361.

Lynch, D. K., Livingston, W., 1995. Color and light in nature. Cambridge; New York: Cambridge University Press.

Manwell, J. F., McGowan, J. G., Rogers, A. L., 2002. Wind Energy Explained, Theory, Design and Application. New York: John Wiley & Sons, Inc..

Melvin, L. M. K., 2004. "Small hydro in Manitoba," M.Sc. Thesis, Department of Mechanical and Manufacturing Engineering, University of Manitoba.

Menter, F. R., 1993. "Zonal two equation  $k-\omega$  turbulence models for aerodynamic flows," AIAA 24<sup>th</sup> Fluid Dynamics Conference, July 6-9, 1993, Orlando, Florida. AIAA-1993-2906.

Menter, F. R., 1994. "Two-equation eddy-viscosity turbulence models for engineering applications". *AIAA Journal*, v. 32, pp. 1598-1605.

Modi, V. J., Akinturk, A., 2003. "Effect of momentum injection on drag reduction of a barge-like structure," *International Journal of Offshore and Polar Engineering*, v. 13, pp. 81-87.

Oerlemans, J., 2005. "Extracting a climate signal from 169 glacier records," *Science*, v. 308, pp. 675-677.

Oliveira, P. J., Younis, B. A., 2000. "On the prediction of turbulent flow around full-scale buildings," *Journal of Wind Engineering and Industrial Aerodynamics*, v. 86, pp. 203-220.

Panton, R. L., 1996. *Incompressible Flow, Second Edition*. New York: John Wiley & Sons, Inc..

Phillips, D.G., Nash, T. A., Oakey, A., Flay, R. G. J., Richards, P. J., 1999. "Computational fluid dynamic and wind tunnel modelling of a diffuser augmented wind turbine," *Wind Engineering*, v. 23, pp. 7-13.

Phillips, D. G., Flay, R. G. J., Nash, T. A., 1999. "Aerodynamic analysis and monitoring of the Vortec 7 diffuser-augmented wind turbine," IPENZ Transactions, 1999, v. 26, n. 1.

Ranasinghe, R., Turner, I. L., 2006. "Shoreline response to submerged structures: A review", Coastal Engineering, v. 53, pp. 65-79.

Raw, M., 1996. "Robustness of Coupled Algebraic Multigrid for the Navier-Stokes Equations", AIAA 96-0297, 34th Aerospace and Sciences Meeting and Exhibit, January 15-18, Reno, NV..

Reddy, M. M. G., Sannasiraj, S. A., Natarajan, R., 2007. "Numerical investigation on the dynamics of a vertical wall defenced by an offshore breakwater", Ocean Engineering, v. 34, pp. 790-798.

Rhie, C. M., Chow, W. L., 1982. "A numerical study of the turbulent flow past an isolated airfoil with trailing edge separation", AIAA Paper 82-0998.

Robinovich, S. G., 2005. Measurement errors and uncertainties: theory and practice, 3rd edition. New York: AIP Press: Springer Science & Business Media.

Scott-Pomerantz, C. D., 2004. "The k-epsilon model in the theory of turbulence," PhD thesis, University of Pittsburgh, Graduate Faculty of Arts and Science.

Segergren, E., 2005. "Direct drive generator for renewable power conversion from water currents", Acta Universitatis Upsaliensis. Digital Comprehensive Summaries of Uppsala Dissertations from the Faculty of Science and Technology 100. pp. 1-44.

Smith, M. R., Donnelly, R. J., Goldenfeld, N., Vinen, W. F., 1993. "Decay of vorticity in homogeneous turbulence," Physical Review Letters, v. 71, pp. 2583-2586.

Speziale, C. G., Sarkar, S., Gatski, T. B., 1991. "Modelling the pressure-strain correlation of turbulence: an invariant dynamical systems approach," Journal of Fluid Mechanics, v. 227, pp. 245-272.

Stamos, D. G., Hajj, M. R., Telionis, D. P., 2003. "Performance of hemi-cylindrical and rectangular submerged breakwaters", Technical note, Ocean Engineering, v. 30, pp. 813-828.

Technomare Spa, IT Power Ltd., 1996. Wave energy project results, the exploitation of tidal marine currents. EU JOULE contract JOU2-CT94-0355, p. 20.

Trapp, T., 2002. "The Stingray tidal stream generator: 150 kW demonstrator completes on-site testing," Energy World, n. 304, pp. 14-16.

Vauthier, P., 2006. "Kite soars to new depths," Water Power Magazine, 2006-03-16.

Accessed 2007-01-09, available at <http://www.waterpowermagazine.com/story.asp?sectionCode=46&storyCode=2034904>

Venezia, W. A., 1994. "Turbine under gulf stream (TUGS): Overview of an energy source potential," IEEE Oceans 1994, v. 3, pp. III.443-III.448. New Jersey: IEEE.

Wilcox, D.C., 1988. "Re-assessment of the scale-determining equation for advanced turbulence models," AIAA Journal, vol. 26, pp. 1414-1421.

Yihua, C., Ziwen, Y., 2005. "Numerical simulation of turbulent flow around helicopter ducted tail rotor," Aerospace Science and Technology, v. 9, pp. 300-306.

Zubkov, V. G., 1985, "Numerical study of laminarization effects in turbulent boundary layers of accelerated flows," Journal of Applied Mechanics and Technical Physics, v.26, pp. 215-221. Translated from Zhurnal Prikladnoi Mekhaniki i Tekhnicheskoi Fiziki, No. 2, pp. 71-78, March-April, 1985.

## Appendix A Turbulence Models

Some of the turbulence models described in Section 2.3 are extensions of other existing turbulence models. For further background into their formulation, these models are described here.

### A.1 Wilcox $k$ - $\omega$ turbulence model

The  $k$ - $\omega$  turbulence model was first introduced by Kolmogorov in 1942 (Kolmogorov 1942). In 1988, a modification to the model was developed (Wilcox 1988). The modification improved the original model and has become widely used (ANSYS 2005). The model uses the eddy-viscosity hypothesis as well as turbulence kinetic energy,  $k$ . The model introduces a new variable, turbulence frequency,  $\omega$ , along with its transport equation. Finally, turbulent viscosity is solved using the relation:

$$\mu_T = \rho \frac{k}{\omega}. \quad (80)$$

Turbulence kinetic energy is given by:

$$\rho \frac{\partial k}{\partial t} + \rho \frac{\partial}{\partial x_i} (kU_i) = \frac{\partial}{\partial x_j} \left[ \left( \mu + \frac{\mu_T}{\sigma_k} \right) \frac{\partial k}{\partial x_j} \right] + P_k - \beta' \rho k \omega, \quad (81)$$

where  $P_k$  is calculated the same as in the  $k$ - $\epsilon$  model, Equation (14) except a maximum value is placed on it, due to infinities encountered in stagnation regions. The turbulence frequency is given by:

$$\rho \frac{\partial \omega}{\partial t} + \rho \frac{\partial}{\partial x_i} (\omega U_i) = \frac{\partial}{\partial x_j} \left[ \left( \mu + \frac{\mu_T}{\sigma_\omega} \right) \frac{\partial \omega}{\partial x_j} \right] + \alpha \frac{\omega}{k} P_k - \beta \rho \omega^2. \quad (82)$$

In the Wilcox  $k$ - $\omega$  model, the constants are:

$$\alpha = 5/9, \beta = 0.075, \beta' = 0.09, \sigma_k = 2, \sigma_\omega = 2. \quad (83)$$

The Wilcox  $k-\omega$  model has some disadvantages, particularly its well-known sensitivity to freestream conditions (Menter 1993). However, the model has superior behaviour in near-wall regions and low Re flows (ANSYS 2005). The Wilcox  $k-\omega$  turbulence model is not used in this study; however it is used as a basis for the shear-stress transport model which is used in this study.

## A.2 Baseline $k-\omega$ turbulence model

The Baseline  $k-\omega$  turbulence model is not used in this study and is not to be confused with the Baseline Reynolds turbulence model, which is used herein. However the Baseline  $k-\omega$  is used as a basis for the shear-stress transport turbulence model, therefore its formulation is detailed.

As an improvement on the Wilcox  $k-\omega$  model, a blended model was developed to combine the advantages of the  $k-\varepsilon$  model with the  $k-\omega$  model. The Baseline (BSL)  $k-\omega$  turbulence model uses the Wilcox  $k-\omega$  model, and defines a transformation of the standard  $k-\varepsilon$  model to adapt it to the  $k-\omega$  formulation. A blending function is then used to bias the results towards the best performing model in each region (i.e., Wilcox  $k-\omega$  in near-wall regions; and  $k-\varepsilon$  model in free shear flows). For instance, the  $k$  transport equation is obtained using:

$$f(k)_{BSL} = F_1[f(k)_{k-\omega}] + (1 - F_1)[f(k)_{k-\varepsilon}], \quad (84)$$



where  $f(k)_{BSL}$ ,  $f(k)_{k-\omega}$ , and  $f(k)_{k-\varepsilon}$ , are the transport equations for  $k$  in the BSL  $k-\omega$  model, the  $k-\omega$  model, and the  $k-\varepsilon$  model respectively; and  $F_1$  is the blending function. The same template is used for the  $\omega$  transport equation.

The resulting model does not suffer from high sensitivity to free stream conditions, yet it retains the improved near-wall behaviour of the  $k-\omega$  model over the  $k-\varepsilon$  model (Menter 1993). However, the model still has some disadvantages, in particular, poor separation prediction (Menter 1994).

### A.3 Reynolds stress- $\omega$ turbulence model

The Reynolds stress- $\omega$  turbulence model is based on the RSTM formulation, using a pressure-strain term defined by:

$$\phi_{ij} = \frac{2}{3} \beta' \rho \omega k \delta_{ij} - \rho \Pi_{ij}, \quad (85)$$

where  $\beta'$  is an empirical constant;  $\omega$  is turbulence frequency, given by Equation (82); and  $\Pi_{ij}$  is the pressure-strain correlation, given by:

$$\Pi_{ij} = \beta' C_{P1} \omega \left( \tau_{ij}^R + \frac{2}{3} k \delta_{ij} \right) - \alpha_P \left( P_{ij} - \frac{1}{3} P_{kk} \delta_{ij} \right) - \gamma_P k \left( S_{ij} - \frac{1}{3} S_{kk} \delta_{ij} \right), \quad (86)$$

where  $C_{P1}$ ,  $\alpha_P$ , and  $\gamma_P$  are empirical constants; and  $P_{ij}$ , is Reynolds stress production tensor, given by:

$$P_{ij} = \tau_{ik}^R \frac{\partial U_j}{\partial x_k} + \tau_{jk}^R \frac{\partial U_i}{\partial x_k}. \quad (87)$$

The Reynolds stress- $\omega$  model has the advantage of superior near-wall treatment over the SSG Reynolds model (ANSYS 2005).

## Appendix B      Optical correction

The PIV experiment produced images of a cross-section of fluid passing through a model suspended in a water tunnel. The images display some obvious noise, especially in the top and bottom third of the cylinder. It was postulated that this noise was due to total-internal reflection caused by the slight difference in the indices of refraction of the water and the acrylic. The effect is shown to be insignificant and the noise remained, obscuring some regions of interest. This section details the calculations for the refractive effects, and the correction algorithm.

### B.1 Optical correction overview

The goal of optical refraction correction is to find a method to transform a distorted image  $I'$  into an undistorted image  $I$ . That is, find a set of functions to relate the *apparent* position with the *actual* position for all points in the image.

$$P_{x,y} = f(P'_{x,y}), \quad (88)$$

where  $P_{x,y}$  and  $P'_{x,y}$  are points in the undistorted and distorted images respectively, and  $f$  is the transformation function we wish to obtain.

### B.2 Cylinder transformation function

Due to the two dimensional nature of the problem, and the importance of the flow passing through it, the cylindrical section was chosen for first analysis. When it was later

discovered that the refractive effects are insignificant, further analysis of other regions was abandoned.

Figure 87 shows a cross section of the PIV set-up, and light rays, with the variables labelled. Some distances are exaggerated for clarity.

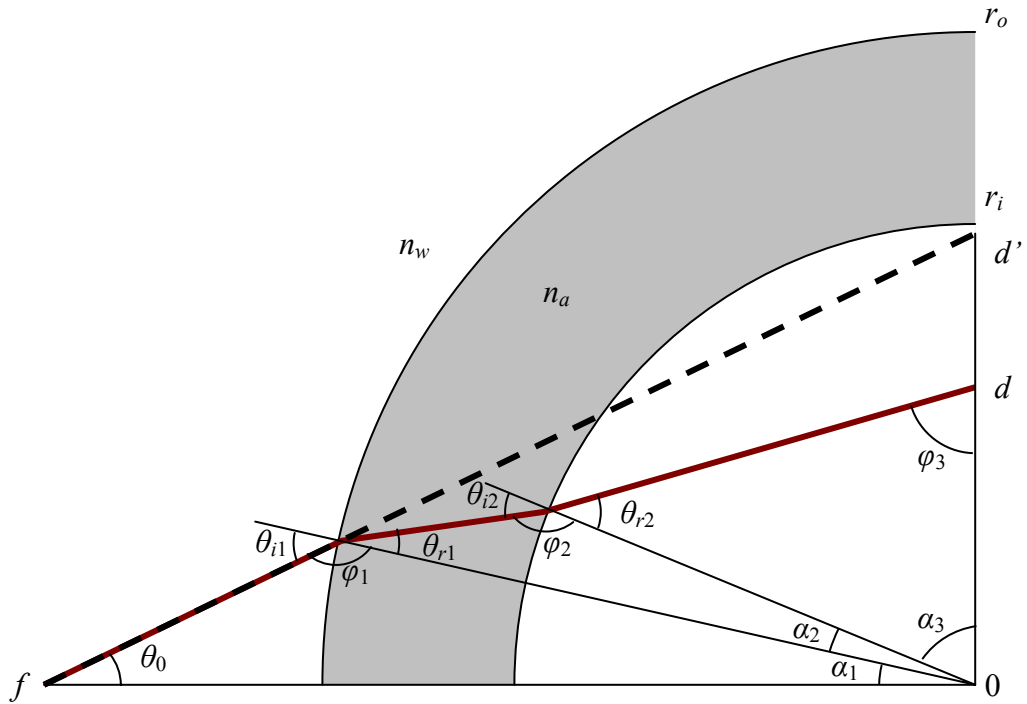


**Figure 87 – Optical correction variables**

From the camera image, we can determine  $d'$ , and we wish to find  $d$ . By geometry, we have:

$$\theta_0 = \tan^{-1}\left(\frac{d'}{f}\right), \quad (89)$$

where  $f$  is the focal length – the distance between the camera lens and the plane of light.

Using sine law, we can find  $\phi_1$  the angle between the light and the surface of the cylinder.

However, direct application of the sine law gives the function:

$$\phi_1 = \sin^{-1}\left(\frac{f}{r_o} \sin(\theta_0)\right),$$

but the  $\sin^{-1}(x)$  function has the range  $-\frac{\pi}{2} \leq \sin^{-1}(x) \leq \frac{\pi}{2}$ , and by inspection, we know that

$\frac{\pi}{2} \leq \phi_1 \leq \pi$ . Therefore, we use:

$$\phi_1 = \pi - \sin^{-1}\left(\frac{f}{r_o} \sin(\theta_0)\right). \quad (90)$$

The sum of the angles of a triangle gives us:

$$\alpha_1 = \pi - \theta_0 - \phi_1 \quad (91)$$

and the angle of incidence at the first interface is the complement of  $\phi_1$ :

$$\theta_{i1} = \pi - \phi_1. \quad (92)$$

The law of refraction gives the refracted angle of light through the acrylic wall:

$$\theta_{r1} = \sin^{-1}\left(\frac{n_w}{n_a} \sin(\theta_{i1})\right) \quad (93)$$

This process is repeated again, with the sine law, the sum of angles on a triangle, the complement, and the law of refraction respectively:

$$\phi_2 = \pi - \sin^{-1}\left(\frac{r_o}{r_i} \sin(\theta_{r1})\right), \quad (94)$$

$$\alpha_2 = \pi - \theta_{r1} - \phi_2, \quad (95)$$

$$\theta_{i2} = \pi - \phi_2, \text{ and} \quad (96)$$

$$\theta_{r2} = \sin^{-1} \left( \frac{n_a}{n_w} \sin(\theta_{i2}) \right). \quad (97)$$

The sum of the  $\alpha$  angles is a right angle, giving:

$$\alpha_3 = \frac{\pi}{2} - \alpha_1 - \alpha_2, \quad (98)$$

and from the sum of the angles on a triangle, we have:

$$\phi_3 = \pi - \theta_{r2} - \alpha_3 \quad (99)$$

Lastly, sine law gives us the actual distance:

$$d = r_i \frac{\sin(\theta_{r2})}{\sin(\phi_3)}. \quad (100)$$

Putting all these together gives the transformation function:

$$d = \frac{d'}{\gamma \cos \left[ \sin^{-1} \left( \frac{d'}{r_i \gamma} \right) + \sin^{-1} \left( \frac{d'}{f} \right) - \sin^{-1} \left( \frac{d'}{r_o \gamma} \right) + \sin^{-1} \left( \frac{n_w d'}{n_a r_o \gamma} \right) - \sin^{-1} \left( \frac{n_w d'}{n_a r_i \gamma} \right) \right]}, \quad (101)$$

where  $\gamma$  is given by:

$$\gamma = \sqrt{1 + \left( \frac{d'}{f} \right)^2}, \quad (102)$$

and:

$d$  is the actual distance from the axis of the cylinder;

$d'$  is the apparent distance from the axis of the cylinder;

$f$  is the distance between the camera lens and the light plane;

$r_o$  and  $r_i$  are the outside and inside radius of the cylinder respectively; and

$n_w$  and  $n_a$  are the indices of refraction of the water and acrylic respectively.

For the experimental set-up, we have these values:

$$f = 63 \text{ [in]}; r_o = 1.25 \text{ [in]}; r_i = 1.00 \text{ [in]}; n_a = 1.49 \text{ []}; n_w = 1.337 \text{ []}$$

The index of refraction of water,  $n_w$ , depends on its temperature and the wavelength. The wavelength of the laser light is 532 nm (Dantec 2005), and assuming room temperature, an approximate value of 1.337 is interpolated from published studies (Lynch et al. 1995).

Given these values, the transformation function is shown in Figure 88.

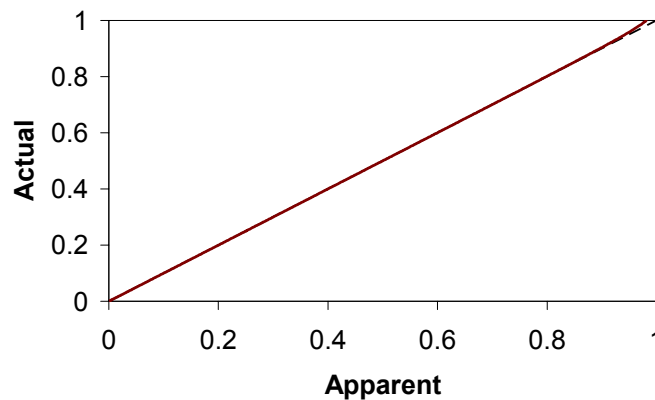


**Figure 88 – Optical transformation function**

The diagonal line,  $y = x$ , represents no optical distortion. Note how closely this function follows this. Alternatively, we can graph the distortion,  $\Delta d = d - d'$ , as shown in Figure 89.

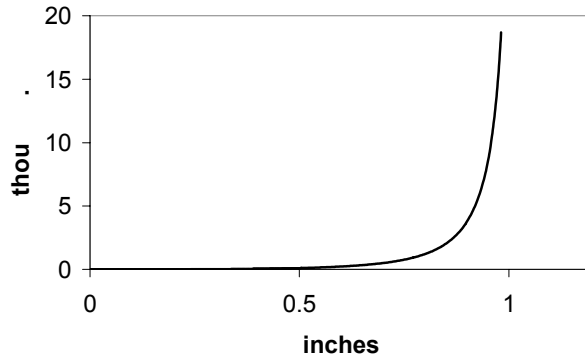


**Figure 89 – Optical distortion**

The maximum possible distortion is less than 19 thousandths of an inch. Two dimensional ray traces of the maximum distortion is shown in Figure 90.

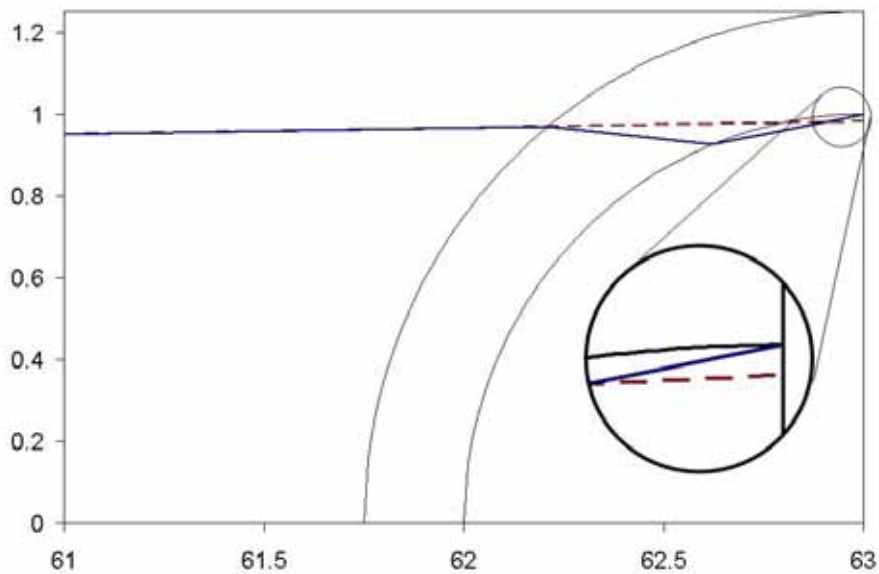


**Figure 90 – Scale ray traces showing maximum deviation**

### **B.3 Transforming an image**

To use this function on a 2-dimensional image, we must know the region of the affected area, i.e. co-ordinates describing the cylinder as it appears in the image. The four co-ordinates of the bounding box for the cylinder should be sufficient to derive all other necessary details about the image.



Given points  $S$  and  $T$ , situated at each end of the cylindrical axis, we calculate:

$$a = y_T - y_S$$

$$b = x_S - x_T \quad (103)$$

$$c = -by_T - ax_T,$$

where  $a$ ,  $b$  and  $c$ , characterize line  $ST$  as:

$$ax + by + c = 0. \quad (104)$$

Given a point  $P$  within the region of interest in the image, we calculate:

$$d' = \frac{|ax_P + bx_P + c|}{\sqrt{a^2 + b^2}} \quad (105)$$

$d$  can then be calculated from (101) above. Point  $R$ , the projection of  $P$  onto  $ST$  is given by:

$$x_R = \frac{ab(y_T - y_P) + b^2x_P + a^2x_T}{a^2 + b^2}$$

$$y_R = \frac{b[ab(y_T - y_P) + b^2x_P + a^2x_T]}{a(a^2 + b^2)} + y_P - \frac{b}{a}x_P \quad (106)$$

Point  $Q$ , the transformed position of point  $P$  is given by:

$$x_Q = x_R + (x_P - x_R)\frac{d}{d'}$$

$$y_Q = y_R + (y_P - y_R)\frac{d}{d'} \quad (107)$$

## B.4 Optical correction MATLAB algorithm

An algorithm for MATLAB to apply these corrections is given below. The results of this algorithm are summarized in Section 5.5.1.

```
function [ im_out ] = Decylindrify( userbox, cdata )
%Decylindrify - Optical correction to a refracted image of a transparent
%               cylinder, viewed perpendicular to cylinder axis.
% Required Inputs
%   cdata(x,y) - a 2 dimensional image array
%               Image values are integer between 0 and 255
%   userbox(x,y) - an array of 4 points describing the outside of the
%               cylinder as seen in the image.
%               userbox(1,:) - x values
%               userbox(2,:) - y values
%               userbox(:,1:4) - sequential points must not be diagonals
%               on the box.
%
% Outputs
%   im_out(x,y) - a 2 dimensional image array, the same size as cdata
%               Points within the userbox *less*the cylinder wall have
%               been modified according to the transformation function.

% Initial inputs - modify these according to the problem
bitmap_x=size(cdata);
bitmap_y=bitmap_x(1);
bitmap_x=bitmap_x(2);
focal=63; %focal length, distance from camera lens to cylinder axis
ro=1.25; %outside diameter of the cylinder
ri=1; %inside diameter of the cylinder
cyl_length=2.8964; %length of the cylinder
Nw=1.337; %index of refraction of water
Na=1.49; %index of refraction of cylinder material

% tir_factor is the value of d that satisfies:
%   f(d)=ri
% where f() is the transformation function and ri is the inside radius.
tir_factor=0.9813153501;

% Regional and scaling calculations
userbox_x=userbox(1,:);
userbox_y=userbox(2,:);
c_line_x=[mean(userbox_x(1:2:3)) mean(userbox_x(2:2:4))];
c_line_y=[mean(userbox_y(1:2:3)) mean(userbox_y(2:2:4))];
delta_userbox_x=[userbox_x(2)-userbox_x(1) userbox_x(4)-userbox_x(3)...
userbox_x(1)-userbox_x(3) userbox_x(2)-userbox_x(4)];
delta_userbox_y=[userbox_y(2)-userbox_y(1) userbox_y(4)-userbox_y(3)...
userbox_y(1)-userbox_y(3) userbox_y(2)-userbox_y(4)];
delta_userbox=sqrt(delta_userbox_x.^2+delta_userbox_y.^2);
scale_y=mean(delta_userbox(1:2))/(2*ro);
scale_x=mean(delta_userbox(3:4))/(cyl_length);
scale_x=mean(delta_userbox(1:2))/(cyl_length);
scale_y=mean(delta_userbox(3:4))/(2*ro);
c_line_l=mean(delta_userbox(1:2));
vec_sw=[c_line_x(2)-c_line_x(1); c_line_y(2)-c_line_y(1)]./c_line_l;
vec_cs=vec_sw([2 1]);
vec_cs(1) = -vec_cs(1);
delta_bent=tir_factor*vec_cs*scale_y;
c_line = [c_line_x; c_line_y];
```

```

bentbox=[delta_bent'; delta_bent']'+c_line;
bentbox(:,3:4)=-[delta_bent'; delta_bent']'+c_line;
bentbox=bentbox(:,[1 2 4 3]);
bentbox_x=bentbox(1,:);
bentbox_y=bentbox(2,:);
delta_unbent=ri*vec_cs*scale_y;
unbentbox=[delta_unbent'; delta_unbent']'+c_line;
unbentbox(:,3:4)=-[delta_unbent'; delta_unbent']'+c_line;
unbentbox=unbentbox(:,[1 2 4 3]);
unbentbox_x=unbentbox(1,:);
unbentbox_y=unbentbox(2,:);
unbentmask=poly2mask(unbentbox_x, unbentbox_y, bitmap_y, bitmap_x);
bentmask=poly2mask(bentbox_x, bentbox_y, bitmap_y, bitmap_x);
im_bent_only=cdata.*uint8(bentmask);
im_not_unbent=cdata.*uint8(not(unbentmask));
imp=im_bent_only;

% Transformation Function look-up table to improve speed
for m=1:1001
    mp=(m-1)/1000;
    gamma=sqrt(1+mp^2/focal^2);
    actual(m)=mp/(gamma*cos( asin(mp/(ri*gamma)) + asin(mp/focal) - ...
asin(mp/(ro*gamma)) + asin(Nw*mp/(Na*ro*gamma)) - asin(Nw*mp/(ri*...
Na*gamma)) ) );
    xactual(m)=mp;
end

% Build final interpolation grid
for m=1:bitmap_y
    imx( m, : ) = [1:bitmap_x];
end
for m=1:bitmap_x
    imy( :, m ) = [1:bitmap_y]';
end

% Centreline values
a=c_line_y(1)-c_line_y(2);
b=c_line_x(2)-c_line_x(1);
c=-b*c_line_y(1)-a*c_line_x(1);
gamma2=sqrt(a^2+b^2)*scale_y;
gamma3=a^2+b^2;

% Main loop
for m=1:bitmap_x*bitmap_y
    m / bitmap_x/bitmap_y * 100
    x=imx(m);
    y=imy(m);
    % Check if point is past the ends of the cylinder
    p=[x-c_line_x; y-c_line_y];
    dotp=[dot(p(:,1),vec_sw) dot(p(:,2),-vec_sw)];
    if or(dotp(1) < 0, dotp(2) < 0) %Past the ends, reject
        d(m)=255;
    else %Between the ends, calculate distance d
        d(m) = abs(a*x + b*y + c) / gamma2;
    end
    %Check if the point is within refraction area
    if and( d(m) > 1E-4, d(m) < tir_factor) %Point within refraction area
        dp(m) = interp1(xactual, actual, d(m));
        xr=(a*b*(c_line_y(1)-y)+b*b*x+a*a*c_line_x(1)) / gamma3;
        yr=b*( a*b*(c_line_y(1)-y) + b*b*x + a*a * x ) / ( a * gamma3 )...
+ y - b/a*x;
        modx(m)=xr + (x - xr) * dp(m) / d(m);
        mody(m)=yr + (y-yr) * dp(m) / d(m);
    end
end

```

```

    modp(m)=imp(m);
elseif d(m) <= 1e-4 %Transformation function breaks down at zero
    modx(m) = x;
    mody(m) = y;
    modp(m) = imp(m);
else
    modp(m) = 0;
    modx(m) = x/1000; %Prevents griddata from failing
    mody(m) = y/1000;
end
end
% Interpolate new points to image grid and add unmodified portions of image
im_corrected=griddata(modx, mody, modp, imx, imy);
im_corrected=uint8(im_corrected).*uint8(unbentmask);
im_out=im_not_unbent+im_corrected;

```

## Appendix C PIV Monte Carlo simulation

To gain more insight into the quality of the PIV data, a Monte Carlo simulation was conducted. The method and results for this study are presented in Section 5.6.1y are presented in Section 5.6.1. The MATLAB code is presented here.

### C.1 Monte Carlo simulation MATLAB algorithm

```
function [ outputarray ] = MonteCarlo( FMInput, DataSetSize, xsize, ysize )
% MONTECARLO Simulation
% * Randomly creates two subsets of a large dataset, no duplications.
% * Gathers statistical data about each subset and compares them against
%   one another.
% * Summarizes the comparison, and repeats for 5 x DataSetSize.
%
% Inputs:
% * FMInput - "As is" output from FlowManager PIV software
%   Contains a 62 x 62 vector map of U, V and Status
%   "Include Vector Status" must be selected prior to FlowManager
%   export.
% * DataSetSize - How many frames are included in the PIV data
% * xsize, ysize - Dimensions of vector map
% Calculations may take a long time

% *** BEGIN INITIALIZATION ***
% Looks at entire dataset and calculates RMS
% standard values for each quantity.

% Read loop - reads in data from FMInput
for i=1:DataSetSize %Read loop
    Ubase(i, :, :) = FMInput{2}.Vec(indicies(i)).U;
    Vbase(i, :, :) = FMInput{2}.Vec(indicies(i)).V;
    Sbase(i, :, :) = FMInput{2}.Vec(indicies(i)).Status;
end

% Filter array loop - creates a Filter array to eliminate rejected vectors
for i = 1:DataSetSize
    for x = 1:xsize
        for y = 1:ysize
            if Sbase(i,x,y)== 0
                a = 1;
            else
                a = 0;
            end
            Fbase(i,x,y) = a;
        end
    end
end

% Appying Filter array to Vector maps
UFbase = Ubase.*Fbase;
VFbase = Vbase.*Fbase;
% N - Number of datapoints not rejected for each location on vector map
Nbase = sum(Fbase, 1);
```

```

% Calculating mean values
UMbase = sum(UFbase, 1);
UMbase = UMbase ./ Nbase;
VMbase = sum(VFbase, 1);
VMbase = VMbase ./ Nbase;

% Calculating u' and v'
for i = 1:N_fields
    UPbase(i, :, :) = (Ubase(i, :, :) - UMbase(1, :, :)) .* Fbase(i, :, :);
    VPbase(i, :, :) = (Vbase(i, :, :) - VMbase(1, :, :)) .* Fbase(i, :, :);
end

% StdDev(U) and StdDev(V) calculations
USDbase = (sum(UPbase.^2, 1) ./ Nbase) .^ .5;
VSDbase = (sum(VPbase.^2, 1) ./ Nbase) .^ .5;
% -uv calculations
UVbase = UPbase .* VPbase;
% Correlation coefficient
Cbase = sum(UVbase, 1) ./ Nbase ./ USDbase ./ VSDbase;

% Generating RMS standards array
UMtemp = reshape(UMbase, 1, xsize * ysize);
RMSbase(1) = ( nanmean(UMtemp) .^ 2 + nanstd(UMtemp) .^2 ) .^ .5;
VMtemp = reshape(VMbase, 1, xsize * ysize);
RMSbase(2) = ( nanmean(VMtemp) .^ 2 + nanstd(VMtemp) .^2 ) .^ .5;
USDtemp = reshape(USDbase, 1, xsize * ysize);
RMSbase(3) = ( nanmean(USDtemp) .^ 2 + nanstd(USDtemp) .^2 ) .^ .5;
VSDtemp = reshape(VSDbase, 1, xsize * ysize);
RMSbase(4) = ( nanmean(VSDtemp) .^ 2 + nanstd(VSDtemp) .^2 ) .^ .5;
Ctemp = reshape(Cbase, 1, xsize * ysize);
RMSbase(5) = ( nanmean(Ctemp) .^ 2 + nanstd(Ctemp) .^2 ) .^ .5;

% *** END INITIALIZATION ***
% *** BEGIN MAIN ANALYSIS ***

% Output array size will contain 5 x DataSetSize points
tempto = DataSetSize * 5
%Main loop
for bigloop = 1:tempto
    % N_fields - size of each subset
    N_fields = ceil(bigloop / 10)

    % Randomly select subsets from total dataset
    rand('state',sum(100*clock))
    indicies = randsample(DataSetSize, N_fields * 2)
    indicies1 = indicies(1:N_fields); %subset1
    indicies2 = indicies( (N_fields + 1): 2 * N_fields); %subset2

    % *** BEGIN SUBSET1 CALCULATIONS ***
    % Read loop
    for i=1:N_fields
        Uarray(i, :, :) = FMInput{2}.Vec(indicies1(i)).U;
        Varray(i, :, :) = FMInput{2}.Vec(indicies1(i)).V;
        Sarray(i, :, :) = FMInput{2}.Vec(indicies1(i)).Status;
    end

    % Filter array loop - generate filter array to remove rejected vectors
    for i = 1:N_fields
        for x = 1:xsize
            for y = 1:ysize
                if Sarray(i,x,y)== 0
                    a = 1;

```

```

        else
            a = 0;
        end
        Farray(i,x,y) = a;
    end
end
end

% Apply filter to vectors
UFarray = Uarray.*Farray;
VFarray = Varray.*Farray;
Narray = sum(Farray, 1);
%Calculate mean vectors
UMarray = sum(UFarray, 1);
UMarray = UMarray ./ Narray;
VMarray = sum(VFarray, 1);
VMarray = VMarray ./ Narray;

% u' and v' calculations
for i = 1:N_fields
    UParray(i, :, :) = (Uarray(i, :, :) - UMarray(1, :, :)) .* Farray(i, :, :);
    VParray(i, :, :) = (Varray(i, :, :) - VMarray(1, :, :)) .* Farray(i, :, :);
end

% Standard Deviation calculations
USDarray = (sum(UParray.^2, 1) ./ Narray) .^ .5;
VSDarray = (sum(VParray.^2, 1) ./ Narray) .^ .5;
% -uv calculations
UVarray = UParray .* VParray;
% Correlation-coefficient
Carray = sum(UVarray, 1) ./ Narray ./ USDarray ./ VSDarray;

% *** END SUBSET1 CALCULATIONS ***
% *** BEGIN SUBSET2 CALCULATIONS ***

% Read loop
for i=1:N_fields
    Uarray2(i, :, :) = FMInput{2}.Vec(indicies2(i)).U;
    Varray2(i, :, :) = FMInput{2}.Vec(indicies2(i)).V;
    Sarray2(i, :, :) = FMInput{2}.Vec(indicies2(i)).Status;
end

% Filter array loop - generate filter array to remove rejected vectors
for i = 1:N_fields
    for x = 1:xsize
        for y = 1:ysize
            if Sarray2(i,x,y)== 0
                a = 1;
            else
                a = 0;
            end
            Farray2(i,x,y) = a;
        end
    end
end

% Apply filter to vectors
UFarray2 = Uarray2.*Farray2;
VFarray2 = Varray2.*Farray2;
Narray2 = sum(Farray2, 1);
% Mean calculations
UMarray2 = sum(UFarray2, 1);
UMarray2 = UMarray2 ./ Narray2;

```

```

VMarray2 = sum(VFarray2, 1);
VMarray2 = VMarray2 ./ Narray2;

% u' and v' calculations
for i = 1:N_fields
    Uarray2(i,:,:)= (Uarray2(i,:,:)-UMarray2(1,:,:)) .* Farray2(i,:,:);
    Varray2(i,:,:)= (Varray2(i,:,:)-VMarray2(1,:,:)) .* Farray2(i,:,:);
end

% Standard deviation calculations
USDarray2 = (sum(Uarray2.^2, 1) ./ Narray2) .^ .5;
VSDarray2 = (sum(Varray2.^2, 1) ./ Narray2) .^ .5;
% -uv calculations
UVarray2 = Uarray2 .* Varray2;
% Correlation-coefficient
Carray2 = sum(UVarray2, 1) ./ Narray2 ./ USDarray2 ./ VSDarray2;

% *** END SUBSET2 CALCULATIONS ***
% *** BEGIN COMPARISON CALCULATIONS ***
UMerror = Uarray - UMarray2;
UMerror = reshape(UMerror, 1, xsize * ysize);
outputarray(1,1) = ( nanmean(UMerror) .^ 2 + nanstd(UMerror) .^2 ) .^ .5...
/ RMSbase(1);
outputarray(1,2) = nanstd(UMerror);

VMerror = Varray - VMarray2;
VMerror = reshape(VMerror, 1, xsize * ysize);
outputarray(2,1) = ( nanmean(VMerror) .^ 2 + nanstd(VMerror) .^2 ) .^ .5...
/ RMSbase(2);
outputarray(2,2) = nanstd(VMerror);

USDerror = USDarray - USDarray2;
USDerror = reshape(USDerror, 1, xsize * ysize);
outputarray(3,1) = ( nanmean(USDerror) .^ 2 + nanstd(USDerror) .^2 ) .^ .5...
/ RMSbase(3);
outputarray(3,2) = nanstd(USDerror);

VSDerror = VSDarray - VSDarray2;
VSDerror = reshape(VSDerror, 1, xsize * ysize);
outputarray(4,1) = ( nanmean(VSDerror) .^ 2 + nanstd(VSDerror) .^2 ) .^ .5...
/ RMSbase(4);
outputarray(4,2) = nanstd(VSDerror);

Cerror = Carray - Carray2;
Cerror = reshape(Cerror, 1, xsize * ysize);
outputarray(5,1) = ( nanmean(Cerror) .^ 2 + nanstd(Cerror) .^2 ) .^ .5 ...
/ RMSbase(5);
outputarray(5,2) = nanstd(Cerror);

bigoutput(bigloop, :, :) = outputarray
end

```